

1998

# Application of finite element models to eddy current probe design for aircraft inspection

Sarit Sharma  
Iowa State University

Follow this and additional works at: <https://lib.dr.iastate.edu/rtd>

 Part of the [Aerospace Engineering Commons](#), and the [Electrical and Computer Engineering Commons](#)

## Recommended Citation

Sharma, Sarit, "Application of finite element models to eddy current probe design for aircraft inspection " (1998). *Retrospective Theses and Dissertations*. 11890.  
<https://lib.dr.iastate.edu/rtd/11890>

This Dissertation is brought to you for free and open access by the Iowa State University Capstones, Theses and Dissertations at Iowa State University Digital Repository. It has been accepted for inclusion in Retrospective Theses and Dissertations by an authorized administrator of Iowa State University Digital Repository. For more information, please contact [digirep@iastate.edu](mailto:digirep@iastate.edu).

## INFORMATION TO USERS

This manuscript has been reproduced from the microfilm master. UMI films the text directly from the original or copy submitted. Thus, some thesis and dissertation copies are in typewriter face, while others may be from any type of computer printer.

**The quality of this reproduction is dependent upon the quality of the copy submitted.** Broken or indistinct print, colored or poor quality illustrations and photographs, print bleedthrough, substandard margins, and improper alignment can adversely affect reproduction.

In the unlikely event that the author did not send UMI a complete manuscript and there are missing pages, these will be noted. Also, if unauthorized copyright material had to be removed, a note will indicate the deletion.

Oversize materials (e.g., maps, drawings, charts) are reproduced by sectioning the original, beginning at the upper left-hand corner and continuing from left to right in equal sections with small overlaps. Each original is also photographed in one exposure and is included in reduced form at the back of the book.

Photographs included in the original manuscript have been reproduced xerographically in this copy. Higher quality 6" x 9" black and white photographic prints are available for any photographs or illustrations appearing in this copy for an additional charge. Contact UMI directly to order.

# UMI

A Bell & Howell Information Company  
300 North Zeeb Road, Ann Arbor MI 48106-1346 USA  
313/761-4700 800/521-0600



Application of finite element models  
to eddy current probe design for aircraft inspection

by

Sarit Sharma

A dissertation submitted to the graduate faculty  
in partial fulfillment of the requirements for the degree of  
DOCTOR OF PHILOSOPHY

Major: Electrical Engineering (Electromagnetics)

Major Professor: Dr. Lalita Udpa

Iowa State University

Ames, Iowa

1998

---

**UMI Number: 9841085**

---

**UMI Microform 9841085**  
**Copyright 1998, by UMI Company. All rights reserved.**

**This microform edition is protected against unauthorized  
copying under Title 17, United States Code.**

---

**UMI**  
**300 North Zeeb Road**  
**Ann Arbor, MI 48103**

---

Graduate College  
Iowa State University

This is to certify that the Doctoral dissertation of  
Sarit Sharma  
has met the dissertation requirements of Iowa State University

Signature was redacted for privacy.

Major Professor

Signature was redacted for privacy.

For the Major Program

Signature was redacted for privacy.

For the Graduate College

to Professor Yushi Sun

---

## TABLE OF CONTENTS

<b>ABSTRACT</b>		vi
<b>1 INTRODUCTION</b>		1
Problem Statement		1
Edge Effect Reduction		4
Remote Field Eddy Current Inspection		5
Magneto-optic Imaging		6
Modeling Probe Performance		7
<b>2 NUMERICAL MODELING</b>		9
Finite Element Method		9
Impedance Computation		14
Analytical Computation		17
Model Validation		21
<b>3 PARALLELIZATION OF MODEL SOLUTION</b>		26
Introduction		26
Parallel Solution		28
Parallel Decomposition		35
<b>4 EDGE EFFECT REDUCTION</b>		39
Edge Effect in Eddy Current Inspection		39
Shielding of Eddy Current Probes		44
Flux Shaping Probe (A)		53
Experimental Results		59
<b>5 REMOTE FIELD EDDY CURRENT</b>		65
Introduction		65
Volume Partition Method		69

---

<b>6</b>	<b>MAGNETO-OPTIC IMAGING</b> . . . . .	75
	Introduction . . . . .	75
	Magneto-optic/Eddy current Imaging . . . . .	79
	Corrosion Detection . . . . .	84
<b>7</b>	<b>CONCLUSION</b> . . . . .	90
	Summary of Accomplishments . . . . .	90
	Future Work . . . . .	91
	<b>REFERENCES</b> . . . . .	93

---

## ABSTRACT

Eddy current nondestructive testing (NDT) methods are used extensively in the inspection of aircraft structures. Improvements and innovations in probe design are constantly required for detection of flaws in complex multilayer aircraft structures. Some of the challenges encountered in aircraft inspection are (i) detection of flaws in close proximity to edges, (ii) detection of cracks in the the second or third layer (iii) detection of corrosion in second and third layer. This thesis investigates alternate designs of eddy current probes for addressing some of these problems.

An important aspect of probe design is the capability to simulate probe performance. Numerical computation and visualization of the electromagnetic fields can provide valuable insight into the design of new probes. Finite element methods have been used in this dissertation to numerically compute the electromagnetic fields associated with the probe coils, and the eddy current probe signals. Most practical test geometries are three dimensional and consequently the numerical models are computationally intensive requiring considerable computing resources. A major contribution of this thesis is development of techniques to reduce the computer resource requirement in the finite element modeling of the eddy current phenomenon.

The first flaw detection problem is addressed by focusing the flux of the probe using active compensation techniques. A novel eddy current probe using a combination of coils is proposed and studied using the 3D model simulation. The probe consists of two current carrying concentric coils to detect flaws closer to the sample edges.

Detection of defects in the second and third layer of samples has been demonstrated using the remote field eddy current (RFEC) method. In the RFEC method the pickup coils are located in the far field region which leads to a large volume to be modeled numerically with large number of elements. A method involving partitioning the volume in the 3D finite element model is demonstrated for the RFEC detection of defects.

Magneto-optic /eddy current imaging (MOI) techniques have shown considerable promise in the detection of corrosion in the second layer. MOI is a nondestructive testing method currently in use

in aircraft frame inspection and it involves optically sensing the magnetic field induced by the eddy currents in the test sample. A numerical model for simulating the MOI test geometry has been developed as an aid for tool optimization.

In all the modeling work, effort is focused towards reducing the computation time and utilizing larger computer memory. The programs that solve the linear equations obtained in the finite element method have been parallelized using the message passing interface (MPI) to run on a cluster of computers. Domain decomposition is achieved by subdividing the stiffness matrix and solving the submatrices in parallel. Results of implementation for a banded complex symmetric matrix using three processors are presented.

## 1 INTRODUCTION

Eddy current methods are used extensively in the inspection and evaluation of conducting materials. An eddy current probe simply consists of a coil or a set of coils excited by a time varying current. When this probe is brought close to a conducting material, it induces (eddy) currents in the specimen (Faraday's law). The effect of these induced currents is to change the impedance of the probe coils. The magnetic field produced by these eddy-currents as given by Ampere's law, opposes the field produced by the current in the probe coil (Lenz's law). The net effect is a change in the magnetic flux linking the coil which by definition is the coil inductance. The eddy currents also cause energy to be dissipated in the conducting material thereby resulting in a change of the coil resistance.

Defects in the material under test disturb the eddy-current distribution which in turn alters the net magnetic flux (probe inductance) and the dissipated power (probe resistance). Consequently the presence of a defect is detected as a change in the impedance of the probe coil scanning the test sample. The changes in coil impedance (or voltage) measured as the probe scans the specimen constitute an eddy current defect signal. The eddy current method represents a non-contact method of nondestructive inspection used for rapid testing and evaluation of conducting samples.

### **Problem Statement**

Eddy current techniques are widely used in electromagnetic nondestructive testing (NDT) and inspection of aircraft structures composed largely of aluminum material. Some of the challenges encountered in eddy current inspection of aircraft parts are (i) detection of flaws in close proximity to edges, (ii) detection of cracks in the second or third layer (iii) detection of corrosion in second and third layer. Development of new probe designs to solve these problems in multilayer structures is therefore of considerable interest to the aerospace industry.

Very often cracks occur close to an edge in multilayer structures in aircraft frames. One of the challenging problems in the inspection of aircraft structures is the detection of flaws in the second

layer in the vicinity of edges as shown in Figure 1.1. This is referred to as the *edge effect problem*. The edge effect is very pronounced at lower operating frequencies which are required for detection of flaws in thick samples. Low frequency eddy current (LFEC) probes are currently used in the inspection of subsurface fatigue cracks in aircraft frame structures [26]. However the interpretation of LFEC signals is rendered difficult by the proximity to hidden edges.

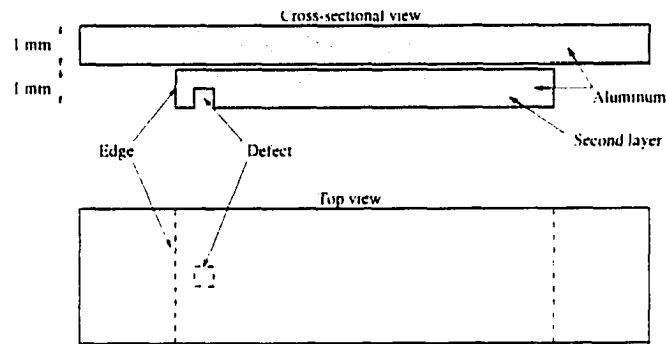


Figure 1.1 Cracks in multi-layer structures in the vicinity of edges.

A second inspection problem is the detection of cracks under fasteners (CUF). A schematic of this geometry is illustrated in Figure 1.2. Aluminum fuselage skins can develop small fatigue cracks after extended period of service due to the numerous pressurization cycles [25]. Cracks emanating from the fastener holes in the aircraft frames are a major source of failures and detection of these flaws is made difficult by the proximity of defects to fastener holes, particularly when the fasteners are made of ferromagnetic material.

Detection of corrosion between aluminum plates in test specimens is yet another problem in aircraft inspection that has had limited success. Figure 1.3 shows a two layer sample with corrosion between the plates. Magneto-optic imaging (MOI) is one of the more recent that offer some promise in the detection of corrosion in multilayer samples.

This thesis presents simple variations of eddy current probe designs to address the inspection problems described here. The three specific problems are solved using three different sensors. The performance of the probes is also investigated using computational models. A major portion of the research effort is therefore focussed on the development of 3D finite element models for simulating the test geometries of interest.

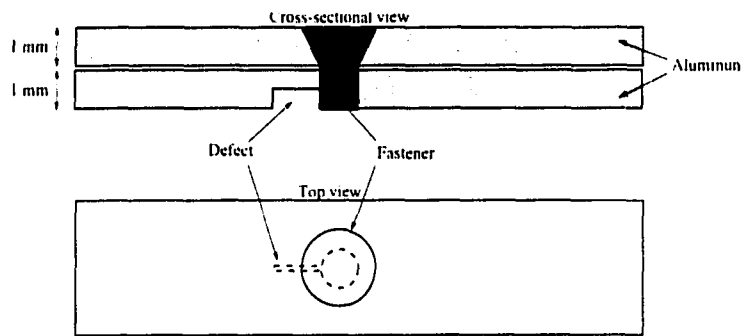


Figure 1.2 Cracks under fasteners in multi-layer structures.

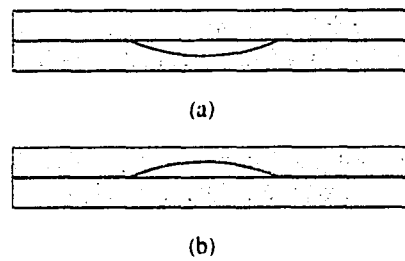


Figure 1.3 Multilayer samples showing corrosion in (a) lower plate and (b) upper plate.

## Edge Effect Reduction

A characteristic feature of eddy current inspection is that the magnetic field around an eddy current probe coil, influences an area larger than the probe diameter [7]. The area into which the magnetic field of the probe coil spreads is called the *probe footprint* which is larger than the physical size of the probe. A direct consequence of the probe footprint is the *edge effect*. Edges in a conducting specimen can be considered as large defects which produce a large eddy current signal. When a defect occurs close to an edge the large contribution from edges therefore masks information related to the defects. The masking of defect signal by edge signal is referred to as edge effect. The larger the footprint of the probe, the more severe is the edge effect. New eddy current probe designs are therefore required for eliminating or minimizing the edge effects in an inspection.

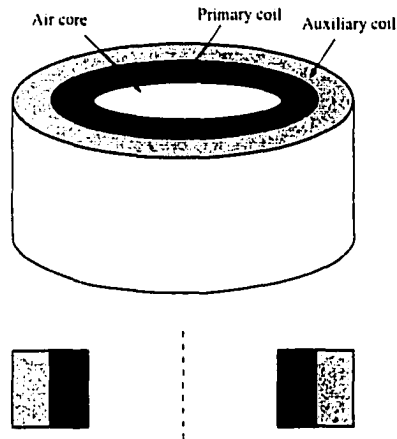


Figure 1.4 A new probe designed using two coils (auxiliary and primary) in a concentric configuration for reducing the effect of edges in eddy current inspection.

One of the earliest techniques used for reducing the probe footprint size is shielding. Coil shields are generally made up of either a high conductivity ( $\sigma$ ) or high permeability ( $\mu$ ) material. These are referred to as eddy current and ferromagnetic shielding respectively. However, as the operating frequency is reduced, the method of shielding becomes less effective in focusing the magnetic flux to a small area. Since the detection of defects that are deep within airframe structures require the use of low frequency (< 5 KHz) probes, shielding is not an effective method in this application.

This thesis presents an alternate approach for focusing flux, based on active compensation using a combination of coils. A probe consisting of an outer auxiliary coil, concentric with an inner primary

coil is shown in Figure 1.4. The total field distribution is controlled by changing the coil geometry and coil currents. Both the magnitude and phase of the currents in the two coils are varied in order to obtain the desired flux pattern. The design parameters of the flux shaping probe is optimized using a 3D finite element model.

## Remote Field Eddy Current Inspection

Conventional eddy current techniques are limited to the inspection of surface and near surface anomalies. The sensitivity of eddy current techniques to deeper flaws can be increased using remote field measurements. The remote field eddy current (RFEC) technique [13], originally used for inspecting tubular metallic product, is characterized by equal sensitivity to a flaw irrespective of its location in the tube wall. This method has been extended for inspecting defects in thick metal plates using the probe as shown in Figure 1.5 [14].

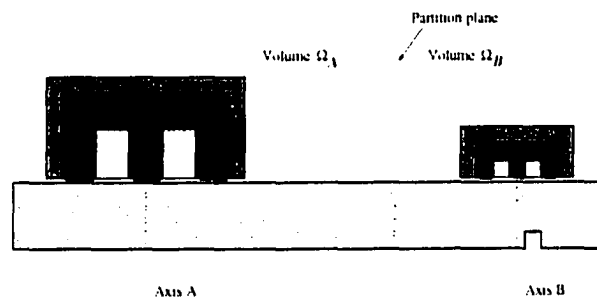


Figure 1.5 Partitioning of the volume to be modeled in order to reduce the computing resource requirement.

The RFEC probe consists of two coils, one of which is excited with current (driver) and the other used to sense the signal (pickup). Both coils consist of an E-shaped ferrite core and a metallic shield on the outside made up of steel and aluminum as shown in Figure 1.5. The driver coil of diameter 100mm is larger than the pickup coil (diameter=50mm). The pickup coil senses the field in the remote field region and the distance between the coil centers is 145mm. The E-shaped core in the pickup coil gives rise to a differential signal in the coil. The modeling of RFEC inspection geometry has been made practical by using a volume partition method.

## Magneto-optic Imaging

The magneto-optic/eddy current imager (MOI) is a nondestructive testing instrument that examines aircraft skin for cracks and corrosion [24],[20]. This method uses magneto-optic principles to generate real time images of defects on a TV monitor. The physical principles of this technique consists of inducing eddy currents in the sample and then imaging the magnetic field associated with these eddy currents using a magneto-optic sensor.

Figure 6.1(a) shows the schematic of the MOI device. A copper foil carrying a time varying (sinusoidal) planar currents is used to induce eddy currents in the sample as shown in Fig 1.6. The presence of defects such as a hole in the sample disturbs the induced eddy currents and the magnetic fields associated with these currents in the sample.

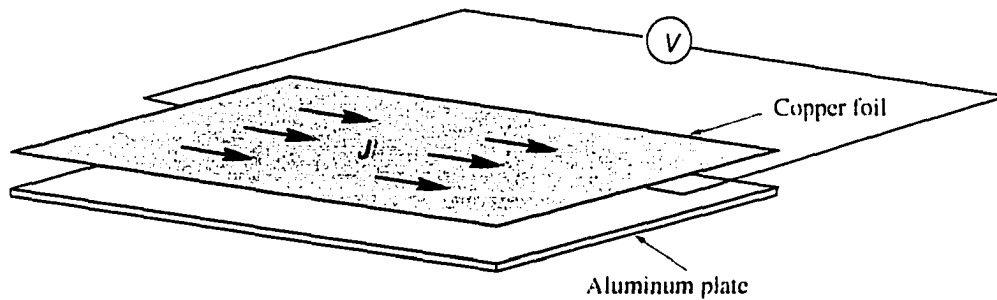


Figure 1.6 Schematic of the magneto-optic/eddy-current imaging device.

With the sample plate in the  $x$ - $y$  plane the  $z$  component of the magnetic field  $\vec{B}$  is mapped using a sensor plate above the copper foil. The sensor consists of a single crystal garnet wafer (gadolinium gallium garnet) which serves as a substrate for an epitaxial magnetic film that is several microns in thickness. When a plane polarized light passes through the film, its plane of polarization is rotated in proportion to the strength of the magnetic field (Faraday's Effect). With appropriate optics, the sensor transforms a spatially varying magnetic field into an optical image.

The MOI device can detect subsurface corrosion in multilayer samples. In order to study the sensitivity and improve the device and improve its performance the field values encountered in MOI inspection are required to be computed.

## Modeling Probe Performance

In general simulation of probe performance using numerical models is an important aspect of the design optimization process. The availability of models is also useful in visualization of the electromagnetic fields around the probe and in the test specimen. Finite element methods have been used in this research to numerically compute the electromagnetic fields associated with the sensors, and the eddy current or remote field eddy current signals. To successfully model the flaw detection signal a three dimensional (3D) finite element model is required. The large distances involved between the driver and pickup coils in an RFEC geometry translate into a large number of elements needed for discretizing the volume. The finite element model consequently requires large amounts of computer resource in terms of both the computer memory and processing time.

In all the modeling work, effort is focused towards reducing the computation time and computer memory requirement. For instance in the remote field eddy current (RFEC) model if the driver and pickup coils are modeled using two different volumes, the computer resource requirement can be reduced and useful numerical results obtained. This is implemented by a two stage procedure. The first step computes the magnetic vector potential  $\vec{A}$  at the partition plane between the driver and pickup coils and using this plane as the boundary plane in subsequently modeling, the remote field eddy current signals of the pickup coil are computed.

In order to further reduce the computation time and utilize larger computer memory the programs that solve the linear equations obtained in the finite element method have been parallelized using the message passing interface (MPI) to run on a cluster of computers. Domain decomposition is achieved by subdividing the stiffness matrix and solving the submatrices in parallel.

The process of domain decomposition can be described in terms of the finite elements. The total space to be modeled is divided into domains which are themselves composed of the elements. The solution is first obtained for the magnetic vector potentials ( $\vec{A}$ ) on the domain walls. Elements in each domain are then solved for individually with the previously computed values on the domain walls as the boundary conditions. Results of implementation on a banded complex symmetric matrix using three processors.

The theoretical basis of the finite element model for eddy current NDT is described in the next chapter followed by a parallel implementation of the finite element solver described in chapter 3. A detailed discussion of the probe design study using flux focusing and remote field eddy current (RFEC) are given in chapters 4 and 5 respectively. The modeling of magneto-optic/eddy current imaging inspection method is described in chapter 6. *Conclusions and future plans* are given in chapter 7.

## 2 NUMERICAL MODELING

### Finite Element Method

Given the basic principles governing the physics of a system, a mathematical model translates these principles into differential equations. To study the system using a mathematical model we have to solve these differential equations. Figure 2.1 illustrates the general method of mathematical modeling. Finite element analysis is an engineering approach used to solve the partial differential equations numerically using a set of discrete elements which approximate the continuous domain.

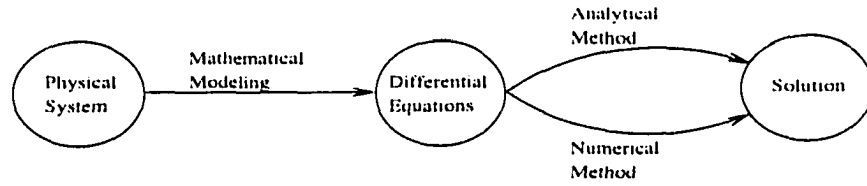


Figure 2.1 Mathematical modeling of physical systems.

The differential equations governing electromagnetic fields are given by the Maxwell's equations.

$$\nabla \times \vec{E} = -\frac{\partial \vec{B}}{\partial t} \quad (2.1)$$

$$\nabla \times \vec{H} = \vec{J} + \frac{\partial \vec{D}}{\partial t} \quad (2.2)$$

$$\nabla \cdot \vec{D} = \rho \quad (2.3)$$

$$\nabla \cdot \vec{B} = 0 \quad (2.4)$$

where  $\vec{H}, \vec{E}$  are the magnetic and electric field strengths.  $\vec{B}, \vec{D}$  are the magnetic and electric flux density, and  $\vec{J}, \rho$  are the current and charge density respectively. In addition, the following constitutive relations describe linear and isotropic media,

$$\vec{D} = \epsilon \vec{E}, \quad \vec{B} = \mu \vec{H}, \quad \vec{J} = \sigma \vec{E}$$

where,  $\epsilon$ ,  $\mu$  and  $\sigma$  are the permittivity, permeability and conductivity of the media, respectively.

Solution to the above equations is obtained through the method of potential functions. The use of potentials enables, in a simple way, to reduce the number of equations. In electromagnetics two basic forms of potential are considered: the first is the magnetic vector potential  $\vec{A}$  and the second the electric vector potential  $\vec{T}$ .

Substituting  $\vec{B} = \nabla \times \vec{A}$  into the Maxwell's equations gives,

- inside eddy current region

$$\nabla \times \nabla \times \vec{A} = \mu\sigma \frac{\partial \vec{A}}{\partial t} + \sigma \nabla V \quad (2.5)$$

- outside eddy current region

$$\nabla \times \nabla \times \vec{A} = 0 \quad (2.6)$$

This formulation referred to as the  $A - V$  model requires the solution of a vector potential equation outside the eddy current region. To avoid this a second potential namely the magnetic scalar potential  $\psi$  is introduced. The non-conducting region is then described by,

$$\nabla^2 \psi = 0 \quad (2.7)$$

where  $\vec{H}$  results from  $\vec{H} = -\nabla \psi$ . This formulation is referred to as the  $A - V - \psi$  model.

The electric vector potential  $\vec{T}$  has the advantage that it gives the possibility of modeling dielectric and conducting regions. It also leads directly to the determination of  $\vec{H}$  since the relation between two vectors is linear. The electric vector potential  $\vec{T}$  is defined as

$$\vec{J} = \nabla \times \vec{T} \quad (2.8)$$

and has as a consequence  $\vec{H} = \vec{T} - \nabla \psi$ , which leads to the following equations:

- inside eddy current region

$$\nabla \times \nabla \times \vec{T} = \mu\sigma \left( \frac{\partial \vec{T}}{\partial t} - \nabla \psi \right) \quad (2.9)$$

$$\nabla^2 = \nabla \cdot \vec{T} \quad (2.10)$$

- outside eddy current region

$$\nabla^2 = 0 \quad (2.11)$$

In this thesis the magnetic vector potential has been used to solve for the electromagnetic fields. The four components in the  $A - V$  formulation can be reduced to three at a cost of complicating the relationships between the potentials and the sources. One such method is referred to as the  $A^*$  formulation which is described below.

Vector  $\vec{B}$  is solenoidal ( $\nabla \cdot \vec{B} = 0$ ) and hence can be expressed as the curl of a vector function  $\vec{A}$  called the *magnetic vector potential*.

$$\vec{B} = \nabla \times \vec{A}$$

Expressing all variables in terms of the vector potential  $\vec{A}$  an equation in the single unknown variable  $\vec{A}$  is obtained in terms of the known quantities.

Substituting  $\vec{B} = \nabla \times \vec{A}$  into equation (2.1) we have,

$$\nabla \times \vec{E} = -\frac{\partial \vec{B}}{\partial t} = -\frac{\partial(\nabla \times \vec{A})}{\partial t} = \nabla \times \left(-\frac{\partial \vec{A}}{\partial t}\right) \quad (2.12)$$

In the case of time-varying electric fields the electric field strength  $\vec{E}$  at a point is generally composed of two components, solenoidal (vortex) ( $E_1$ ) and an irrotational (source) ( $E_2$ ). The solenoidal-field component  $E_1$  ( $\nabla \cdot \vec{E}_1 = 0$ ) is due to a time varying magnetic field and the irrotational-field component  $E_2$  ( $\nabla \times \vec{E}_2 = 0$ ) due to the impressed voltage (or charge distribution). A source field can be expressed as a gradient of a scalar potential function  $V$  and conventionally this is expressed as  $E_2 = -\nabla V$ . Equation (2.5) can therefore be integrated and expressed as,

$$\vec{E} = \vec{E}_1 + \vec{E}_2 = -\frac{\partial \vec{A}}{\partial t} - \nabla V$$

In terms of the known quantities and the impressed currents the vector  $\vec{E}$  can be expressed as,

$$\sigma \vec{E} = \vec{J} = -\sigma \frac{\partial \vec{A}}{\partial t} - \sigma \nabla V + \vec{J}_s \quad (2.13)$$

In the  $A^*$  formulation the magnetic vector potential  $\vec{A}$  is replaced by,

$$\vec{A}^* = -\frac{\partial \vec{A}}{\partial t} - \nabla V \quad (2.14)$$

and the equation for  $\vec{E}$  in terms of  $\vec{A}^*$  can be written as,

$$\vec{E} = -\frac{\partial \vec{A}^*}{\partial t}$$

The symbol  $*$  is dropped in representing the modified magnetic vector potential in the rest of the thesis.

In conventional eddy current testing where the excitation frequency is less than a few mega Hertz, the induced conduction current density ( $\sigma \vec{E}$ ) is much greater than the displacement current density ( $\epsilon \frac{\partial \vec{E}}{\partial t}$ ), and hence the equation (2.2) can be written as,

$$\nabla \times \vec{H} = \vec{J} + \frac{\partial \vec{D}}{\partial t} = \sigma \vec{E} + \frac{\partial(\epsilon \vec{E})}{\partial t} \approx \sigma \vec{E}$$

Substituting  $\vec{B} = \nabla \times \vec{A}$  into the above equation we have,

$$\sigma \vec{E} = \nabla \times \vec{H} = \nabla \times \frac{\vec{B}}{\mu} = \nabla \times \frac{1}{\mu} (\nabla \times \vec{A}) \quad (2.15)$$

Comparing the equations (2.6) and (2.7) we have the vector potential equation.

$$\nabla \times \frac{1}{\mu} (\nabla \times \vec{A}) = -\sigma \frac{\partial \vec{A}}{\partial t} + \vec{J}_s$$

Under sinusoidal steady state conditions the magnetic vector potential  $\vec{A}$  is a phasor quantity and the above equation becomes

$$\nabla \times \frac{1}{\mu} (\nabla \times \vec{A}) = -j\omega\sigma \vec{A} + \vec{J}_s \quad (2.16)$$

This vector potential equation can be solved for  $\vec{A}$ , which can then be used to derive other quantities such as  $\vec{B}$ ,  $\vec{J}_c$ ,  $\vec{E}$  and  $\vec{H}$ . Analytical closed form solution to equation (2.8) is available only for very simple geometries. Consequently for most practical cases, the solution to the above equations is obtained using the numerical techniques such as finite element methods.

Among the many methods available for finite element formulation, the weighted residual method (Galerkin's method) and the use of an energy functional stemming from a global energy balance concept are commonly used. The general approach of any variational method is to derive a function capable of minimizing the energy functional rather than solve the above equation directly. The energy balance formulation lends itself to an easy physical interpretation. A general energy functional for electromagnetic field problems can be written as.

$$\begin{aligned} \mathcal{F} &= \text{magnetic field energy} + \text{electric field energy} \\ &= \text{stored energy} + (\text{dissipated energy} - \text{input energy}) \end{aligned}$$

The stored energy is due to the magnetic field, the input energy is derived from the impressed current densities and the dissipated energy arises from the eddy current densities in the conducting parts of the geometry.

In terms of field quantities the energy functional can be written as,

$$\mathcal{F} = \int_v \frac{1}{2} \vec{H} \cdot \vec{B} dv + \int_v \frac{1}{2} \vec{J} \cdot \vec{A} dv$$

$$\begin{aligned}
&= \int_v \frac{1}{2} \vec{H} \cdot \vec{B} dv + \int_v \frac{1}{2} \vec{J}_e \cdot \vec{A} dv - \int_v \frac{1}{2} \vec{J}_s \cdot \vec{A} dv \\
&= \int_v \left[ \frac{1}{2\mu} |\vec{B}|^2 + \frac{1}{2} \sigma \left( -\frac{\partial \vec{A}}{\partial t} \right) \cdot \vec{A} - \frac{1}{2} \vec{J}_s \cdot \vec{A} \right] dv
\end{aligned}$$

In the case of harmonic excitation we have,

$$= \int_v \left[ \frac{1}{2\mu} |\nabla \times \vec{A}|^2 + \frac{1}{2} j\omega\sigma |\vec{A}|^2 - \frac{1}{2} \vec{J}_s \cdot \vec{A} \right] dv$$

The minimization of this function with respect to the magnetic vector potential  $\vec{A}$  yields the solution of vector  $\vec{A}$ . The terms inside the integrand represent the energy terms corresponding to the magnetic field, eddy currents and the source currents respectively.

In two-dimensions the equation can be expressed by the energy functional,

$$\mathcal{F} = \int_v \left[ \frac{1}{2\mu} \left\{ \left| \frac{\partial \vec{A}_y}{\partial x} \right|^2 + \left| \frac{\partial \vec{A}_x}{\partial y} \right|^2 \right\} + \frac{1}{2} j\omega\sigma |\vec{A}|^2 - \vec{J}_s \cdot \vec{A} \right] dv$$

and in three-dimensions we have the energy functional,

$$\mathcal{F} = \int_v \left[ \frac{1}{2\mu} \left\{ \left| \frac{\partial \vec{A}_z}{\partial y} - \frac{\partial \vec{A}_y}{\partial z} \right|^2 + \left| \frac{\partial \vec{A}_x}{\partial z} - \frac{\partial \vec{A}_z}{\partial x} \right|^2 + \left| \frac{\partial \vec{A}_y}{\partial x} - \frac{\partial \vec{A}_x}{\partial y} \right|^2 \right\} + \frac{1}{2} j\omega\sigma |\vec{A}|^2 - \vec{J}_s \cdot \vec{A} \right] dv$$

The next step in the finite element technique is to discretize the region of interest into small areas (2 dimensional) or volumes (3 dimensional) called *elements* connected to each other at *nodes*. The discretized energy functional in terms of the variable values at the nodes of the *mesh* is then given by,

$$\mathcal{F} = \sum_{i=1}^n \left[ \frac{1}{2\mu} \left\{ \left| \frac{\partial \vec{A}_{zi}}{\partial y} - \frac{\partial \vec{A}_{yi}}{\partial z} \right|^2 + \left| \frac{\partial \vec{A}_{xi}}{\partial z} - \frac{\partial \vec{A}_{zi}}{\partial x} \right|^2 + \left| \frac{\partial \vec{A}_{yi}}{\partial x} - \frac{\partial \vec{A}_{xi}}{\partial y} \right|^2 \right\} + \frac{1}{2} j\omega\sigma |\vec{A}_i|^2 - \vec{J}_{si} \cdot \vec{A}_i \right]$$

where  $n$  is the total number of nodes in the solution region.

Energy balance in the solution region is achieved by minimizing the energy functional within every element of the region. This is achieved by setting the first partial derivative of  $\mathcal{F}(\vec{A})$  with respect to each component of  $\vec{A}$  at each node to zero.

$$\frac{\partial \mathcal{F}(\vec{A})}{\partial A_{ki}} = 0, \quad i = 1, 2, 3, \dots, n; \quad k = x, y, z$$

We then have  $3n$  simultaneous linear equations in  $3n$  variables. These equations can be rearranged so that they may be represented by the matrix equation,

$$[G][A] = [Q]$$

where  $[G]$  is a  $(3n \times 3n)$  banded symmetric complex matrix,  $[A]$  and  $[Q]$  are  $(3n \times 1)$  complex column matrices. In practice, the minimization is performed on an element by element basis and the contribution of individual elements is summed to obtain the algebraic equations in the entire solution region. This *assembly* is achieved using the *connectivity matrix*. This procedure results in a global matrix equation in terms of all the variables of equation (2.15) which is solved for the unknown nodal magnetic vector potential ( $\vec{A}$ ). With the choice of triangular elements (3 nodes) in the two dimensional model and hexahedral elements (8 nodes) in a three dimensional model we obtain a  $G$  matrix that is complex, banded and symmetric. It is significant to observe that the  $G$  matrix is symmetric and not hermitian.

The system of equations is solved using a standard solution technique such as Gaussian elimination to obtain,

$$A = G^{-1}Q$$

The solution of the nodal values of  $\vec{A}$  is used for computing various physically measurable quantities such as flux density  $\vec{B}$ , eddy current density  $\vec{J}_e$ , and probe impedance  $Z$ .

Since in eddy current testing the signal is composed of changes in probe impedance  $Z$ , the calculation of coil impedance starting from nodal values of  $\vec{A}$  is described next.

## Impedance Computation

The eddy current method of NDT uses the change in the impedance of the coil as a signal to detect and characterize defects. This signal is plotted as an impedance-plane diagram, with resistance along one axis and the inductive reactance (or inductance) along the other. The size and shape of this plot is interpreted to extract meaningful information about the integrity of the test specimen. In numerical modeling of the eddy current phenomenon the probe impedance has to be computed from the nodal values of the magnetic vector potential  $\vec{A}$ . There are several approaches for computing the impedance of a circular coil, namely the power/energy method and the flux method.

In the power/energy method, coil impedance is found from the dissipated power and stored energy. Hence this approach yields total impedance regardless of the number of coils, their shapes or location in the solution region [4]. The flux method on the other hand can be used to compute the impedance of individual coils by computing the total flux linking a coil in the solution space.

The power/energy method computes the impedance from the dissipated power and stored energy. In terms of field quantities, the dissipated power and stored energies  $P$  and  $W$  over a volume  $v$ , are

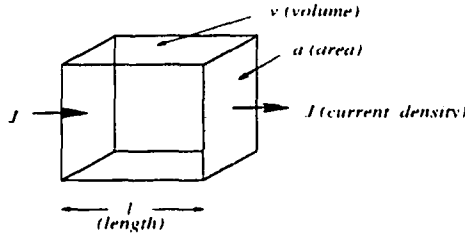


Figure 2.2 Current carrying element in the discretized three dimensional model.

calculated using the equations.

$$\begin{aligned} \text{Dissipated Power } P &= \frac{1}{2} \int_v \vec{J} \cdot \vec{E} dv \\ \text{Stored Energy } W &= \frac{1}{2} \int_v \vec{H} \cdot \vec{B} dv \end{aligned}$$

These values are calculated for each element and summed over all the elements to obtain the average dissipated power and total stored energy.

Consider the  $i$ th element of length  $l_i$  along the direction of vector  $\vec{J}_i$ , a cross section area  $a_i$  normal to  $l_i$ , with a volume  $v_i$ , permeability  $\mu_i$  and conductivity  $\sigma_i$ . Expressed in terms of the centroidal vector  $\vec{A}_i$  the dissipated power and stored energy in each element are computed as.

$$\begin{aligned} P_i &= \frac{1}{2} \int_{v_i} \vec{J}_i \cdot \vec{E}_i dv = \frac{1}{2} \int_{v_i} \sigma_i \vec{E}_i \cdot \vec{E}_i dv = \frac{\sigma_i}{2} \int_{v_i} |\vec{E}_i|^2 dv = \frac{\sigma_i}{2} \int_{v_i} \left| \frac{\partial \vec{A}_i}{\partial t} \right|^2 dv \\ &\approx \frac{\sigma_i}{2} \omega^2 |\vec{A}_i|^2 v_i \\ W_i &= \frac{1}{2} \int_{v_i} \vec{H}_i \cdot \vec{B}_i dv = \frac{1}{2} \int_{v_i} \frac{\vec{B}_i}{\mu_i} \cdot \vec{B}_i dv = \frac{1}{2\mu_i} \int_{v_i} |\vec{B}_i|^2 dv = \frac{1}{2\mu_i} \int_{v_i} |\nabla \times \vec{A}_i|^2 dv \\ &\approx \frac{1}{2\mu_i} |\nabla \times \vec{A}_i|^2 v_i \end{aligned}$$

The total power dissipated and energy stored in the volume of interest is then computed as.

$$P = \sum_{i=1}^n P_i = \sum_{i=1}^n \frac{\sigma_i}{2} \omega^2 |\vec{A}_i|^2 v_i \quad W = \sum_{i=1}^n W_i = \sum_{i=1}^n \frac{1}{2\mu_i} |\nabla \times \vec{A}_i|^2 v_i$$

where  $n$  is the total number of elements in the finite element mesh.

Assuming a current  $I$  ( $I_{rms} = I/\sqrt{2}$ ) through the coil, the total dissipated power ( $P$ ) and the energy stored ( $W$ ) in terms of the coil parameters are given as.

$$\begin{aligned} P &= \frac{1}{2} I^2 R \\ W &= \frac{1}{2} I^2 L \end{aligned}$$

From the above equations we compute impedance of the coil as

$$Z = R + j\omega L = \frac{P}{I^2} + j\omega \frac{2W}{I^2}$$

Since the design of the new eddy current probes involves multiple coil configurations, the power/energy method cannot be used to compute the impedance of individual coils. The flux method is therefore used to compute the impedance of each coil. The total flux linking the coil is computed directly using the magnetic vector potential  $\vec{A}$  vector or the magnetic flux density  $\vec{B}$  ( $\vec{B} = \nabla \times \vec{A}$ ).

In the flux method, the total flux linking the coil (of  $N$  turns) is calculated and the impedance is computed as,

$$Z = \frac{V}{I} = \frac{1}{I}(-N \frac{\partial \phi}{\partial t}) = -\frac{j\omega N}{I} \phi$$

where  $N$  is the number of turns in the coil and  $\phi$  is the total flux linking the coil. The flux  $\phi$  can also be computed by directly using the vector  $\vec{B}$ , or using the vector  $\vec{A}$  ( $\vec{B} = \nabla \times \vec{A}$  and applying the Stoke's theorem),

$$\phi = \int_S \vec{B} \cdot d\vec{S} \quad \text{or} \quad \phi = \int_l \vec{A} \cdot d\vec{l}$$

where  $\vec{S}$  is the surface area enclosed by the coil, normal to the direction of  $\vec{B}$  and  $\vec{l}$  is along the circumference of the coil.

Consider the  $i$ th element with the surface area  $\vec{S}_i$  in the plane of the coil and let  $m$  be the number of elements enclosed by the coil in the plane. The impedance  $Z$  using the elemental values of  $\vec{B}_i$  is,

$$Z = -\frac{j\omega N}{I} \sum_{i=1}^m \vec{B}_i \cdot \vec{S}_i = -\frac{j\omega N}{I} \sum_{i=1}^m \nabla \times \vec{A}_i \cdot \vec{S}_i \quad (2.17)$$

If  $l_i$  is the length of the  $i$ th element with the length along the circumference of the coil and  $n$  is the number of elements in the coil carrying the current and  $p$ , the number of current carrying elements in the cross-section of the coil. The impedance  $Z$  using the elemental values of  $\vec{A}_i$  (centroidal) is,

$$Z = -\frac{j\omega N}{I} \frac{1}{p} \sum_{i=1}^n \vec{A}_i \cdot \vec{l}_i \quad (2.18)$$

In the absence of magnetic materials, inductance (self) is a parameter that is independent of the value of the current and depends only on the geometry of the coil. The value of inductance can therefore be used to validate the numerical methods that are used to model the eddy current phenomenon.

The finite element models have to be first validated prior to their use in probe design studies. In this thesis the validation is done by comparing the model prediction of probe impedance with analytical calculations for some simple cases. The analytical derivation of the electromagnetic fields and impedance of the coil is described next.

## Analytical Computation

The law of Biot-Savart which is a statement of observation, enables us to calculate the magnetic field  $\vec{H}$  generated by an electrical current and is given by,

$$dI\vec{H}(\vec{r}) = \frac{1}{4\pi} \frac{I d\vec{l} \times (\vec{r} - \vec{r}')}{|\vec{r} - \vec{r}'|^3} \quad (2.19)$$

where  $d\vec{l}$  is a vector differential line element with a constant current  $I$ ,  $\vec{r}'$  and  $\vec{r}$  are position vectors of the source and the observation point, respectively.

## Coil Filament Approximation

Starting from the law of Biot-Savart, the vector potential  $\vec{A}$  and the magnetic induction  $\vec{B}$  due to an arbitrary current filament are given by [10],

$$\vec{A}(\vec{r}) = \frac{\mu_0 I}{4\pi} \int_l \frac{d\vec{l}}{|\vec{r} - \vec{r}'|} \quad (2.20)$$

$$\vec{B}(\vec{r}) = \frac{\mu_0 I}{4\pi} \int_l \frac{d\vec{l} \times (\vec{r} - \vec{r}')}{|\vec{r} - \vec{r}'|^3} \quad (2.21)$$

where  $\mu_0$  is the free-space permeability.

For a closed circular filament since  $\vec{A}_z = \vec{A}_r = 0$  and  $\vec{B}_\phi = 0$  we obtain,

$$A_\phi(\vec{r}) = \frac{\mu_0 I}{4\pi} \int_0^{2\pi} d\phi r' D^{-1}(\phi) \cos \phi \quad (2.22)$$

$$B_j(\vec{r}) = \frac{\mu_0 I}{4\pi} \int_0^{2\pi} d\phi r' D^{-3}(\phi) \begin{cases} -\gamma \cos \phi \\ r' - r \cos \phi \end{cases} \quad (j = r, z), \quad (2.23)$$

where  $\vec{r}' = (r', \phi', z')$  and  $\vec{r} = (r, \phi, z)$  are the coordinates of the source and field point, respectively and

$$D(\phi) = \sqrt{\gamma^2 + r'^2 + r^2 - 2rr' \cos \phi}, \quad \gamma = z' - z, \quad \phi = \phi' - \phi$$

These equations can be solved analytically for the field values on the axis ( $r = 0$ ) of the coil. The field values for this case with the coil of radius ( $r' = R$ ) placed at the origin ( $z' = 0$ ) is,

$$\vec{A}_\phi(0, 0, z) = 0, \quad \vec{B}_r(0, 0, z) = 0, \quad \vec{B}_z(0, 0, z) = \frac{\mu_0 I R^2}{2(R^2 + z^2)^{3/2}} \quad (2.24)$$

In order to evaluate the field at any other point in space, the expressions are transformed into integrals over Jacobian elliptic functions and expressed in terms of *complete* elliptical integrals  $K(k)$  and  $E(k)$  of the first and second kind, respectively with modulus  $k$  these equations are [10],

$$\vec{A}_\phi(\vec{r}) = \left(\frac{\mu_0 I}{4\pi}\right) \frac{2a}{r} [(1 - k^2/2)K(k) - E(k)] \quad (2.25)$$

$$\vec{B}_r(\vec{r}) = \left(\frac{\mu_0 I}{4\pi}\right) \frac{\gamma}{ar} [K(k) - \frac{(2 - k^2)}{2k'^2} E(k)] \quad (2.26)$$

$$\vec{B}_z(\vec{r}) = \left(\frac{\mu_0 I}{4\pi}\right) \frac{2}{ar} [rK(k) - \frac{(2r - bk^2)}{2k'^2} E(k)] \quad (2.27)$$

where,

$$a = \sqrt{\gamma^2 + (r' + r)^2} \quad k = \sqrt{\frac{4rr'}{a^2}} \quad b = r + r' \quad k' = \sqrt{1 - k^2}$$

When the field point lies directly on the circular loop ( $r = r'$  and  $z' = z$ ), then  $k^2 = 1$  these equations show a singular behavior.

Consider a circular filament of radius  $r' = 4$  mm carrying a current  $I = 4$  A centered on the origin ( $z' = 0$  mm) in the x-y plane. Using the above equations to compute the  $\vec{A}$  and  $\vec{B}$  fields in a plane 0.5 mm above the coil ( $z = 0.5$  mm), we get  $\vec{A}(0, 0, 0) = 0$  and  $\vec{B}(0, 0, 0) = 6.28 \times 10^{-4}$  Tesla at the center of the coil. Figures 2.3 display the fields along the radial axis ( $\phi = 0$ ,  $z = 0.5$  mm). Figure 2.3(a) shows the magnitude of vector  $\vec{A}_z$  with a maximum value at the radius of coil ( $r = 4$  mm). Figure 2.3(b) shows the vector  $\vec{B}_z$  and  $\vec{B}_r$ .  $\vec{B}_z$  has two extrema, a maxima inside and a minima outside the coil radius with a zero crossing at  $r = 4$  mm. The radial component  $\vec{B}_r$  has a maximum at  $r = 4$  mm.

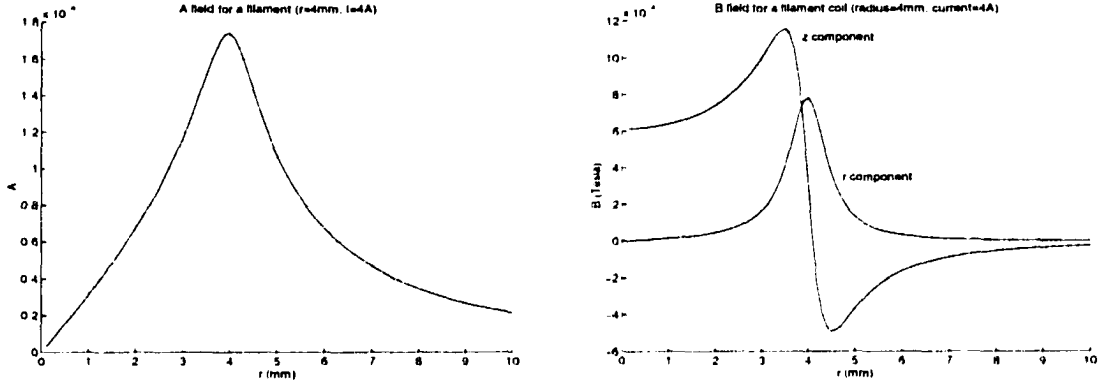


Figure 2.3 Analytically computed  $\vec{A}_z$  and  $\vec{B}$  fields measured along the radial axis

### Coil With Rectangular Cross Section

Starting from the law of Biot-Savart, the vector potential  $\vec{A}$  and the magnetic induction  $\vec{B}$  due to an arbitrary three dimensional volume current are given by [11],

$$\vec{A}(\vec{r}) = \frac{\mu_0 J}{4\pi} \int_t \int_s \frac{d\vec{l}}{|\vec{r} - \vec{r}'|} ds \quad (2.28)$$

$$\vec{B}(\vec{r}) = \frac{\mu_0 J}{4\pi} \int_t \int_s \frac{d\vec{l} \times (\vec{r} - \vec{r}')}{|\vec{r} - \vec{r}'|^3} ds \quad (2.29)$$

where  $J$  is the azimuthal constant current density in the conductor and  $ds$  is a differential element of cross sectional area orthogonal to  $d\vec{l}$ .

For a closed circular coil of rectangular cross section  $(\vec{R}_2 - \vec{R}_1) \times (\vec{Z}_2 - \vec{Z}_1)$ , the field and source points are  $\vec{r} = (r, \varphi, z)$  and  $\vec{r}' = (r', \varphi', z')$  respectively with  $R_1 \leq r' \leq R_2$  and  $Z_1 \leq z' \leq Z_2$ . After integrating over  $r'$  and  $z'$  the following expressions are obtained for the vector potential ( $\vec{A}$ ) and the magnetic field ( $\vec{B}$ ).

$$\vec{A}(\vec{r}) = \frac{\mu_0 J}{4\pi} \vec{A}(\vec{r}) \Big|_{r'=R_1}^{R_2} \Big|_{z'=Z_1}^{Z_2} \quad (2.30)$$

$$\vec{B}(\vec{r}) = \frac{\mu_0 J}{4\pi} \vec{H}(\vec{r}) \Big|_{r'=R_1}^{R_2} \Big|_{z'=Z_1}^{Z_2} \quad (2.31)$$

Since for a coil  $\vec{A}_z = \vec{A}_r = 0$  and  $\vec{B}_\phi = 0$ , we obtain

$$\begin{aligned} \vec{A}_\phi(\vec{r}) = & \frac{1}{2} \int_0^{2\pi} d\phi [\gamma D(\phi) + 2\gamma r \cos \phi \sinh^{-1} J_1(\phi) \\ & + (r'^2 - r^2 \cos 2\phi) \sinh^{-1} J_2(\phi) - r^2 \sin 2\phi \tan^{-1} J_3(\phi)] \cos \phi \end{aligned} \quad (2.32)$$

$$\bar{H}_r(\bar{r}) = \int_0^{2\pi} d\phi \cos \phi [D(\phi) + r \cos \phi \sinh^{-1} \beta_1(\phi)] \quad (2.33)$$

$$\bar{H}_z(\bar{r}) = \int_0^{2\pi} d\phi [\gamma \sinh^{-1} \beta_1(\phi) - r \cos \phi \sinh^{-1} \beta_2(\phi) - r \sin \phi \tan^{-1} \beta_3(\phi)] \quad (2.34)$$

where,

$$\gamma = z' - z, \quad \phi = \varphi' - \varphi$$

$$B(\phi) = \sqrt{r'^2 + r^2 - 2rr' \cos \phi}, \quad D(\phi) = \sqrt{\gamma^2 + B^2(\phi)}, \quad G(\phi) = \sqrt{\gamma^2 + r^2 \sin^2 \phi}$$

$$\beta_1(\phi) = \frac{(r' - r \cos \phi)}{G(\phi)}, \quad \beta_2(\phi) = \frac{\gamma}{B(\phi)}, \quad \beta_3(\phi) = \frac{\gamma(r' - r \cos \phi)}{r \sin \phi D(\phi)}$$

These expressions are then transformed into integrals over Jacobi elliptic functions and expressed in terms of the *complete* elliptic integrals of the first ( $\Pi(n_1^2, k)$ ), second ( $\Pi(n_2^2, k)$ ) and third ( $\Pi(n_3^2, k)$ ) kind with modulus  $k$ .

$$\bar{A}_\phi(\bar{r}) = \frac{r}{3} C(r, r') + \gamma r \mathcal{J}(\pi/2) + \frac{\gamma a}{6r} [U(k)K(k) - 2r' E(k)]$$

$$+ \frac{\gamma}{6ar} [-P_\varphi(n_1)\Pi(n_1^2, k) + P_\varphi(n_2)\Pi(n_2^2, k) - P_\varphi(n_3)\Pi(n_3^2, k)] \quad (2.35)$$

$$\bar{H}_r(\bar{r}) = r \mathcal{J}(\pi/2) - \frac{ar'}{2r} [E(k) - v(k)K(k)]$$

$$- \frac{1}{4ar} [-Q_r(n_1)\Pi(n_1^2, k) + Q_r(n_2)\Pi(n_2^2, k) - Q_z(n_3)\Pi(n_3^2, k)] \quad (2.36)$$

$$\bar{H}_z(\bar{r}) = C(r, r') + 2\gamma \mathcal{J}(\pi/2) - \frac{3a}{4r} \gamma k^2 K(k)$$

$$- \frac{1}{4ar} [-Q_z(n_1)\Pi(n_1^2, k) + Q_z(n_2)\Pi(n_2^2, k) - Q_z(n_3)\Pi(n_3^2, k)] \quad (2.37)$$

where,

$$a = \sqrt{\gamma^2 + (r' + r)^2}, \quad b = r' + r, \quad c = \sqrt{\gamma^2 + r^2}, \quad k = \sqrt{\frac{4r'r}{a^2}}, \quad k' = \sqrt{1 - k^2}$$

$$n_1 = \sqrt{\frac{2r}{r - c}}, \quad n_2 = \sqrt{\frac{2r}{r + c}}, \quad n_3 = \sqrt{\frac{4r'r}{b^2}}$$

$$v(k) = 1 + \frac{k^2(\gamma^2 - br)}{2rr'}, \quad U(k) = k^2 \frac{4\gamma^2 + 3r'^2 - 5r^2}{4r}$$

$$Q_r(n_1) = (r' + c) \frac{n_1^2 \gamma^2 c}{r}, \quad Q_r(n_2) = (r' - c) \frac{n_2^2 \gamma^2 c}{r}, \quad Q_r(n_3) = 0$$

$$Q_z(n_1) = (r' + c)(-2\gamma c n_1^2), \quad Q_z(n_2) = (r' - c)(-2\gamma c n_2^2), \quad Q_z(n_3) = \gamma b(r' - r)n_3^2$$

$$P_\varphi(n_1) = (r' + c)n_1^2 c \frac{(3r^2 - c^2)}{2r}, \quad P_\varphi(n_2) = (r' - c)n_2^2 c \frac{(3r^2 - c^2)}{2r}, \quad P_\varphi(n_3) = -\frac{r'}{b}(r' - r)(3r^2 - r'^2)$$

$$C(r, r') = -\frac{1}{2}\pi r [1 + \text{sgn}(r' - r)], \quad \mathcal{J}(\pi/2) = \int_0^{\pi/2} \sinh^{-1} \beta_1(\phi) d\phi$$

It has not been possible to find an analytic solution in terms of known functions for the integral  $\mathcal{J}(\pi/2)$ . However, an approximate solution of such types of integrals can be found.

$$\mathcal{J}(\pi/2) = \int_0^{\pi/2} \sinh^{-1} \beta_1(\phi) d\phi$$

$$\begin{aligned}
&= \int_0^{\pi/2} \ln[(r' - r \cos \phi) + D(\phi)] d\phi \\
&= \int_0^{\pi/2} \ln\left[1 + \frac{(r' - r \cos \phi)}{D(\phi)}\right] d\phi + \int_0^{\pi/2} \ln[D(\phi)] d\phi \\
&= \int_0^{\pi/2} \ln\left[1 + \frac{(r' - r \cos \phi)}{D(\phi)}\right] d\phi + \frac{\pi}{4} \ln[r'^2 + r^2 + \gamma^2 + \sqrt{(r'^2 + r^2 + \gamma^2)^2 - 4r'^2 r^2}] \\
&= \int_0^{\pi/2} \ln\left[1 + \frac{(r' - r \cos \phi)}{D(\phi)}\right] d\phi + \frac{\pi}{4} \ln[D^2(\pi/2) + \sqrt{D^4(\pi/2) - 4r'^2 r^2}]
\end{aligned}$$

If  $\gamma \neq 0$ , then  $-1 < (r' - r \cos \phi)/D(\phi) < 1$  and the logarithm in the integrand can be expanded in series as,

$$\ln\left[1 + \frac{(r' - r \cos \phi)}{D(\phi)}\right] = \left[\frac{(r' - r \cos \phi)}{D(\phi)}\right] - \frac{1}{2}\left[\frac{(r' - r \cos \phi)}{D(\phi)}\right]^2 + \frac{1}{3}\left[\frac{(r' - r \cos \phi)}{D(\phi)}\right]^3 - \dots$$

Using the first term in this series as the approximation we have,

$$\mathcal{J}(\pi/2) \approx \int_0^{\pi/2} \frac{(r' - r \cos \phi)}{D(\phi)} d\phi + \frac{\pi}{4} \ln[D^2(\pi/2) + \sqrt{D^4(\pi/2) - 4r'^2 r^2}]$$

where the first term can be represented in terms of elliptic integrals of the first and second kind.

## Model Validation

The most frequently modeled probes are circular coils of rectangular cross section. These coils combine the advantage of large attainable inductance with the simplicity of construction. Consider a coil of  $N$  turns as illustrated in Figure 2.4 with mean radius  $a$ , the axial dimension of the cross section  $b$  and the radial dimension of the cross section  $c$ . Inductance is a function of the shape of the coil and two shape ratios of  $\frac{c}{2a}$  and  $\frac{b}{c}$  represent the shape in the analytical computation. For the case of a coil with square cross section ( $b = c$ ) with  $(0 < \frac{c}{2a} < 1)$  some simple formulae have been derived.

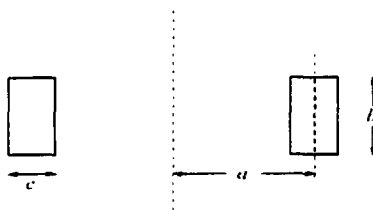


Figure 2.4 A circular coil of rectangular cross section indicating the parameters required to analytically compute the inductance.

For the coil geometry shown in Figure 2.1 a working formula for inductance ( $L$ ) as obtained in [9] is given by,

$$L = a.N^2 P \times 10^{-7} \quad (2.38)$$

where  $P$  is a function of the ratio  $\frac{c}{2a}$  alone expressed as,

$$P = 4\pi \left[ \frac{1}{2} \left\{ 1 + \frac{1}{6} \left( \frac{c}{2a} \right)^2 \right\} \log_e \frac{8}{\left( \frac{c}{2a} \right)^2} - 0.84834 + 0.2041 \left( \frac{c}{2a} \right)^2 \right] \quad (2.39)$$

For a coil with  $N = 100$ ,  $a = 4\text{mm}$ ,  $b = c = 2\text{mm}$ , with a shape ratio  $\frac{c}{2a} = 0.25$ , the equation (2.31) gives  $P = 20.304$  and inductance ( $L$ ) evaluates to  $81.2160 \mu\text{Henries}$ .

In order to validate the finite element models, a simple circular coil is modeled using both the two and three dimensional finite element models and their results compared with that obtained using analytical calculations. Table 2.1 gives the parameter details used in numerical modeling. The analytically computed value is compared with the values obtained from the numerical models in the Table 2.2. The value of inductance can be computed by calculating the total flux enclosed by the coil or by the power/energy considerations.

In the 2D model the equation  $\Phi = \int_l \vec{A} \cdot d\vec{l}$  is used to calculate the flux. The 3D model uses this equation and the equation  $\Phi = \int_s \vec{B} \cdot d\vec{S}$  to compute the flux  $\Phi$ . In 3D modeling inductance can also be computed from the power/energy considerations. Table 2.2 shows the equations involved in computing the inductance of the coil and the inductance computed. The inductance value computed using the power/energy method in 3D model ( $80.0603\mu H$ ) gives the least amount of error when compared with the analytical value ( $81.216\mu H$ ).

The source of error in the equation using  $\Phi = \int_l \vec{A} \cdot d\vec{l}$  to compute total flux linking the coil is the approximation of the vector  $d\vec{l}$ . Also  $\vec{J}_s$  is assumed to be constant along the circumference of the coil. The source of error in the equation using  $\Phi = \int_s \vec{B} \cdot d\vec{S}$  to compute the total flux linking the coil is in the estimation of the total area which has flux flowing in the positive direction. As the number of elements in the cross section area of the coil is increased this error will decrease.

The discretization of the volume in three dimensional (3D) finite element model in the plane  $\phi = 0$  in the  $r, \phi, z$  coordinate system is the same as discretization of the area in two dimensions. Both models use same values of the parameters as indicated in Table 2.1.

Figures 2.5, 2.6 and 2.7 present comparisons of the field values, as obtained from the 2D and 3D finite element models. Figures 2.5 shows flux plots computed using the 2D and 3D models. Figure 2.6 shows the corresponding plots of the vector  $\vec{A}_\theta$  along the radial direction. Figure 2.7 presents the  $\vec{B}_z$  and  $\vec{B}_r$  components as computed along the radius in the plane of the coil ( $z = 0$ ).

Table 2.1 Numerical model parameters for inductance computation

Probe coil (mean) radius $r$	4mm
Coil cross-section (square)	2mm $\times$ 2mm
Number of turns in the coil	100
Coil current density $J_s$	$10^6$ A/m
Frequency $f$	1 KHz
Conductivity $\sigma$ (coil wire)	0 S/m
Permeability $\mu_r$ (coil wire)	1

Table 2.2 Comparison of coil inductance computed numerically and analytically.

Computation Method	Inductance ( $\mu$ H)
Analytical	81.2160
Two dimensional finite element model emf $E = -N \frac{\partial \phi}{\partial t} = -j\omega N \phi = -j\omega N \int_l \vec{A} \cdot d\vec{l} = IZ$	72.2910
Three dimensional finite element model stored energy $W = \frac{1}{2} \int_v \vec{B} \cdot \vec{H} dv = \frac{1}{2\mu} \int_v  \vec{B} ^2 dv = \frac{1}{2} LI^2$	80.0603
Three dimensional finite element model emf $E = -N \frac{\partial \phi}{\partial t} = -j\omega N \phi = -j\omega N \int_s \vec{B} \cdot d\vec{S} = IZ$	78.2560
Three dimensional finite element model emf $E = -N \frac{\partial \phi}{\partial t} = -j\omega N \phi = -j\omega N \int_l \vec{A} \cdot d\vec{l} = IZ$	79.3417

The  $\vec{A}$  values computed using the 2D model are in agreement with the analytical values. However, the analytical  $\vec{B}$  field values are in close agreement with the values computed by the 3D model. The vector  $\vec{A}$  computed using the 3D model and the vector  $\vec{B}$  computed by the 2D model show large errors. For example the value of  $\vec{B}_z$  at the origin computed analytically is 6.28 Teslas, whereas the 3D model predicts a value of 6.00 Teslas and the 2D model predicted value is 4.25 Teslas. These errors are not completely understood and further investigation is required.

A more accurate method to compute the inductance of a circular coil with square cross-section is derived in [6]. Figure 2.8 shows the coil dimensions in cylindrical coordinates used in the analytical computation.

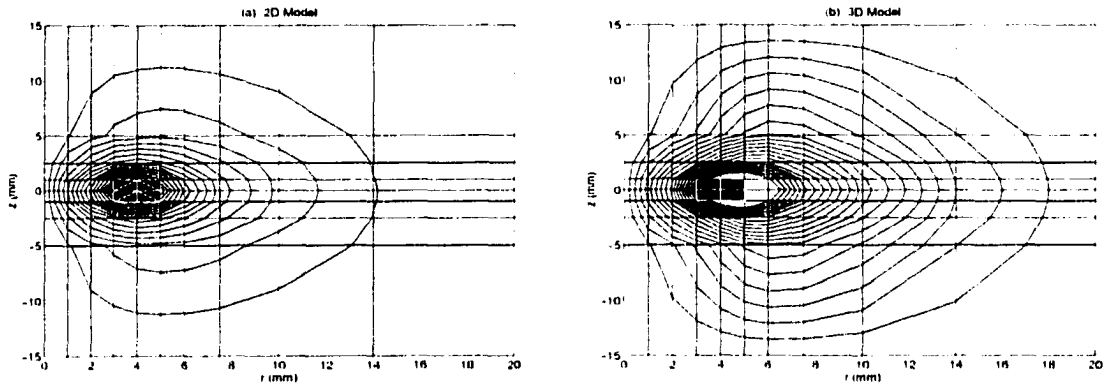


Figure 2.5 Comparison of computed  $\vec{A}$  for 2D and 3D models.

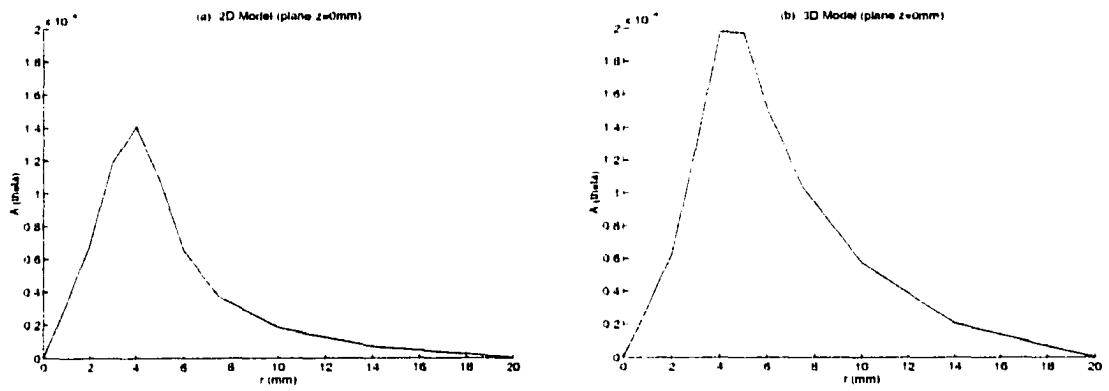


Figure 2.6 Comparison of  $\vec{A}_\theta$  for (a) 2D and (b) 3D models.

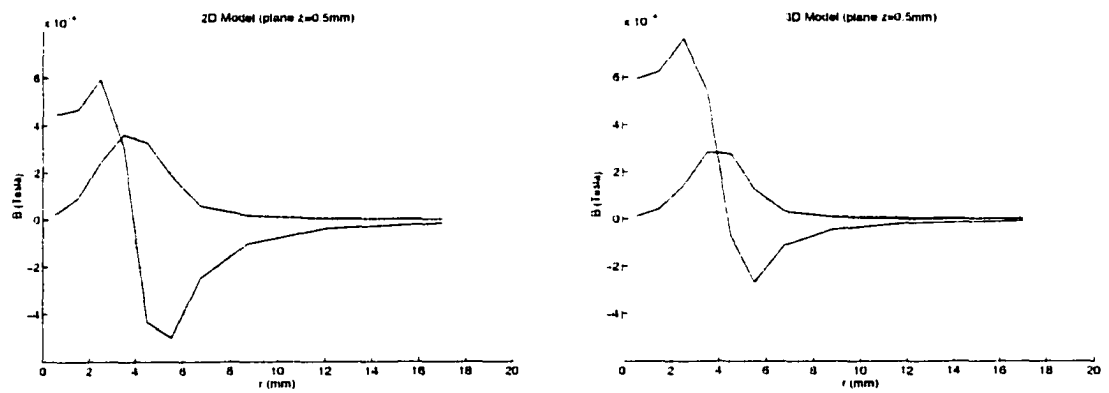


Figure 2.7 Comparison of  $\vec{B}$  for (a) 2D and (b) 3D models.

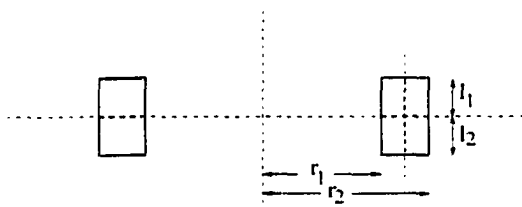


Figure 2.8 A circular coil of rectangular cross section indicating the parameters required to analytically compute the inductance.

Induced voltage in a length of wire is given by,

$$V = j\omega \int \vec{A} \cdot d\vec{s} \quad (2.40)$$

For an axially symmetric coil with a single loop of radius  $r$  the above equation becomes

$$V = j\omega 2\pi r A(r, z) \quad (2.41)$$

The total voltage induced in a coil of  $n$  turns is then

$$V = j\omega 2\pi \sum_{i=1}^n r_i A(r_i, z_i) \quad (2.42)$$

We can approximate the above summation by an integral over a turn density of  $N$  turns per unit cross-sectional area:

$$V \approx j2\pi\omega \int \int_{\text{coil-cross-section}} r A(r, z) N dr dz \quad (2.43)$$

For coils with a constant number of turns per unit cross-sectional area

$$V = \frac{j2\pi\omega n}{\text{coil-cross-section}} \int \int_{\text{coil-cross-section}} r A(r, z) dr dz \quad (2.44)$$

If we specify a rectangular cross-section coil of length  $(l_2 - l_1)$  and of inner and outer radii  $r_1$  and  $r_2$ , respectively, we can write

$$V = \frac{j2\pi\omega n}{(l_2 - l_1)(r_2 - r_1)} \int_{l_1}^{l_2} \int_{r_1}^{r_2} r A(r, z) dr dz \quad (2.45)$$

The impedance  $Z = V/I$  can therefore be written as

$$Z = \frac{j2\pi\omega n}{(l_2 - l_1)(r_2 - r_1)i} \int_{l_1}^{l_2} \int_{r_1}^{r_2} r A(r, z) dr dz \quad (2.46)$$

### 3 PARALLELIZATION OF MODEL SOLUTION

#### Introduction

The finite element method solves a set of partial differential equations by minimizing a variational function derived from the original equations. The governing equation for eddy current analysis is

$$\nabla \times \frac{1}{\mu} \nabla \times \vec{A} = -j\omega\sigma\vec{A} + \vec{J}_s \quad (3.1)$$

and the corresponding energy (variational) functional is expressed as,

$$\mathcal{F} = \int_v \left[ \frac{1}{2\mu} |\nabla \times \vec{A}|^2 + \frac{1}{2} j\omega\sigma |\vec{A}|^2 - \frac{1}{2} \vec{J}_s \cdot \vec{A} \right] dv$$

The minimization of the discretized form of this function with respect to the magnetic vector potential  $\vec{A}$  at each node yields the numerical solution of vector  $\vec{A}$ . If  $n$  is the number of nodes in the discretized mesh,

$$\frac{\partial \mathcal{F}(\vec{A})}{\partial A_{ki}} = 0, \quad i = 1, 2, 3, \dots, n; \quad k = x, y, z$$

gives  $3n$  simultaneous linear equations in  $3n$  variables. These equations are rearranged so that they are represented by the matrix equation,

$$[G][A] = [Q]$$

where  $[G]$  is a  $(3n \times 3n)$  sparse, banded symmetric complex matrix,  $[A]$  and  $[Q]$  are  $(3n \times 1)$  complex column matrices.

In general the solution of the set of linear equations takes upto 95% of the total computation time. The stiffness matrix  $G$  for a practical mesh can use several gigabytes (GB) of computer memory even after exploiting the properties of symmetry and bandedness. In order to reduce the computing time the memory requirement can be distributed over a cluster of workstations. This requires the solver to be parallelized using the message passing paradigm of parallel computing.

Multiprocessor parallel computing systems consist of a number of interconnected processors. An individual processor, or node, may be a scalar or vector processor. Vector processors are specialized

machines that are specifically targeted at problems involving considerable amount of vector arithmetic. Based on how the processors are connected we can have a shared memory system or a local (distributed) memory system as shown in Figure 3.1. In the shared memory systems the main computer memory is a global resource available to all processors where as in a distributed memory system each processor has its own local memory. A cluster of work stations is a distributed memory system that can be assembled into a parallel computing machine inexpensively. Such a cluster of workstations (COWs) is scalable i.e. more processors can be added as and when they become available.

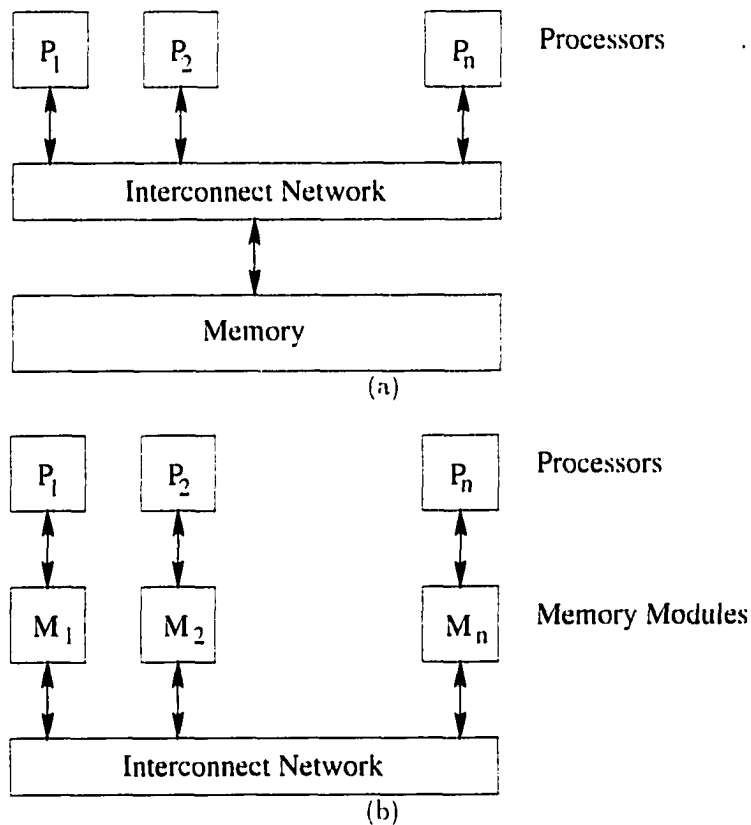


Figure 3.1 Multiprocessor computing systems: (a) shared memory system (b) local or distributed memory system.

A sequential code that runs on a computer needs to be decomposed so that it may run on a cluster of workstations. Software decomposition can be achieved by either function decomposition or domain decomposition [27]. In function decomposition each processor executes a different sub-function, the results of which when put together give the total solution. However the process of

breaking the desired function into subfunctions is not scalable, i.e. there is an upper limit to the number of subprocesses. The load on different processors may also not be equal as the subfunctions may be different. This method of software decomposition is not *scalable* and the system cannot be easily *load balanced*. In *domain decomposition* each processor performs the same operations with different data. This method is inherently load balanced and is also scalable.

Domain (or data) decomposition requires some communication between the subprocesses or some "message passing". In this thesis the programs that solve the set of linear equations  $[G][A] = [Q]$  have been parallelized using the domain decomposition method. The stiffness matrix  $G$  has been decomposed into smaller submatrices and the vector  $Q$  is also decomposed into corresponding subvectors. The protocol used for inter-process communication is the Message Passing Interface (MPI).

## Parallel Solution

Figure 3.2 shows a pictorial representation of the symmetric, banded matrix equation  $[G][A] = [Q]$  with the shaded area representing the *nonzero entries*.

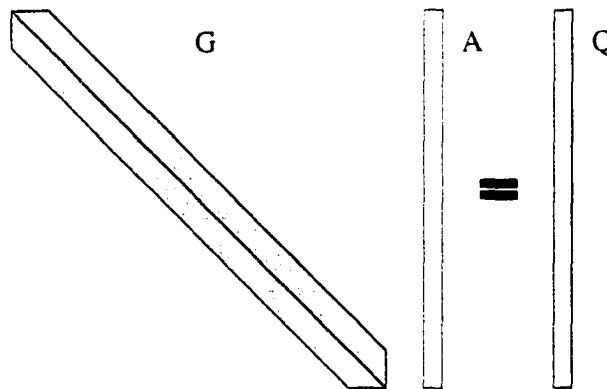


Figure 3.2  $G$  matrix and  $A, Q$  vectors in equation  $G A = Q$ .

Figure 3.3(a) shows a simple decomposition of matrix  $G$  into submatrices  $G_1$  and  $G_2$ . As can be seen from Figure 3.3(a), this decomposition does not take into account some of the nonzero entries in the  $G$  matrix as indicated by the dark shaded region. Figure 3.3(b) shows an alternative scheme for decomposing the matrix with some overlap which will require some communication between the processes working on submatrices  $G_1$  and  $G_2$ . The Figure also shows the corresponding overlap in

the decomposition of vector  $Q$ .

In order to solve the two system of equations  $G_1 A_1 = Q_1$  and  $G_2 A_2 = Q_2$  independent of each other (or in parallel) it is required to decouple the two systems. Hence the terms corresponding to these variables,  $g_b$  which appear in both systems must be eliminated.

Figures 3.4 and 3.5 shows the sequential algorithm used to decouple the matrices  $G_1$  and  $G_2$ . The algorithm starts with downward elimination of matrix  $G_1$  as indicated in Figure 3.4(a). This followed by the upward elimination of  $G_1$  which leads to nonzero entries in the vertical band as in Figure 3.4(b). The diagonal entries in the unshaded  $G_1$  matrix are ones.

Figure 3.5(a) shows the downward elimination of  $G_2$  followed by upward elimination as in Figure 3.5(b). The elimination process described in Figures 3.4 and 3.5 are carried out using only row operations and hence they do not effect the vector  $A$ . The vector  $Q$  is affected at each and every row operation that is performed on matrix  $G_1$  or  $G_2$ .

It is observed from Figure 3.5(b) that the rows indicated by  $g_a$  contain nonzero entries in matrix  $G$  corresponding to variables indicated by  $g_b$ . And similarly rows indicated by  $g_b$  have nonzero entries corresponding to variables indicated by  $g_b$  and  $g_c$ , and rows indicated by  $g_c$  have nonzero entries corresponding to variables indicated by  $g_b$  and  $g_c$ . In other words the variables indicated by  $g_a$ ,  $g_b$  and  $g_c$  are expressed as linear combinations of each other.

The rows and columns corresponding to variables  $g_a$ ,  $g_b$  and  $g_c$  can therefore now be solved for, separately from the rest of the matrix. Figure 3.6 shows the assembly of the nonzero entries for these variables. These are then solved by gaussian elimination to obtain solution vector  $A$  corresponding to variables  $g_a$ ,  $g_b$  and  $g_c$ . The shaded area in Figure 3.7 shows the elements of vector  $A$  that have been solved for in the linear system of equations.

This partially computed  $A$  vector is substituted into the original equations represented by Figure 3.2. Figure 3.8 shows the part of the linear equation system that remains to be solved. In this remaining system of equations if the appropriately marked elements of vector  $A$  are multiplied by the corresponding elements of vector  $G$  and moved to the right hand side the system as shown in Figure 3.9 we obtain a system as shown in Figure 3.10. Figure 3.8 shows the effect of this substitution, which is to decouple the matrices  $G_1$  and  $G_2$ .

The two sets of linear equations shown in Figure 3.10 are solved in parallel to obtain the vectors  $A_1$  and  $A_2$ . The values computed from Figures 3.9 and 3.6 are combined to obtain the total solution  $A$  as shown in Figure 3.11.

Decomposing the global stiffness matrix  $G$  into the decoupled submatrices as described in this

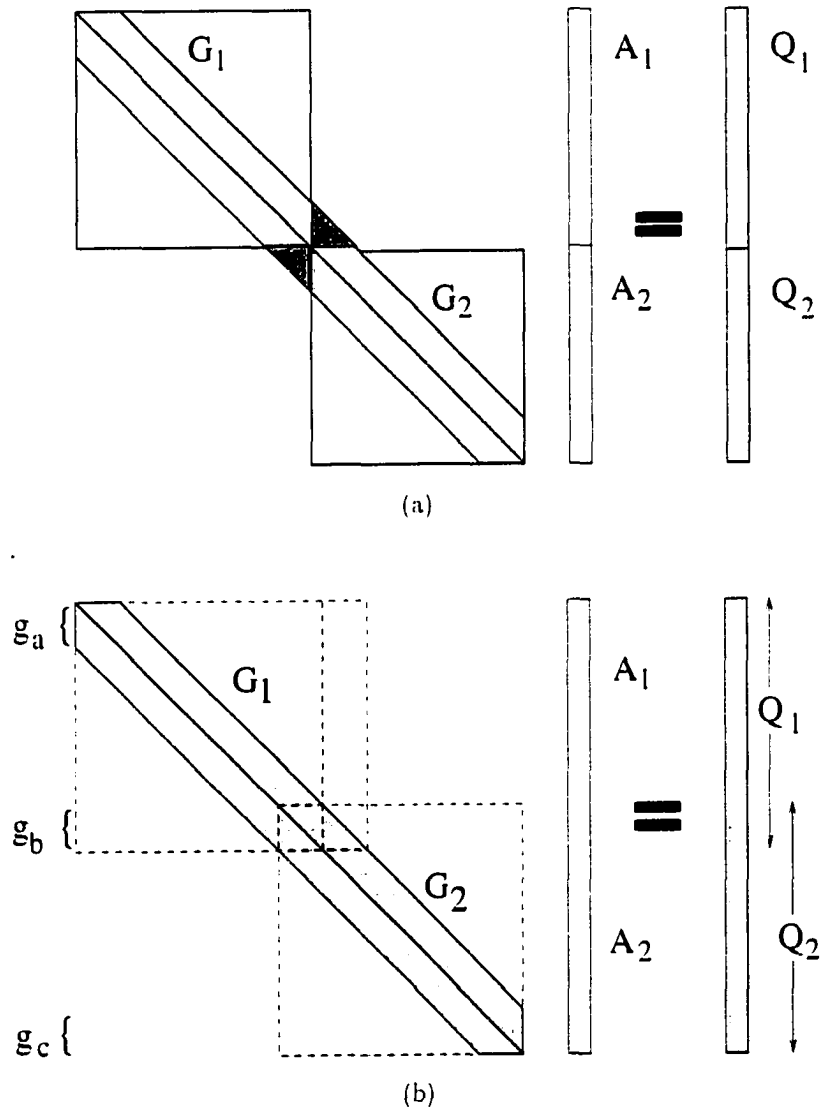


Figure 3.3 Decomposition of the  $GA = Q$  into two subproblems.

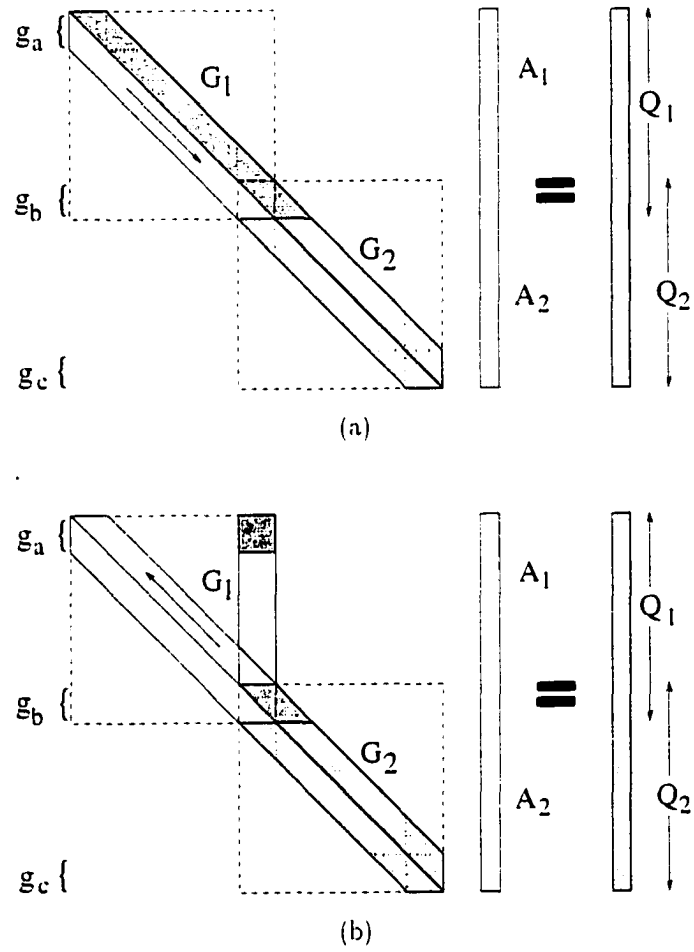


Figure 3.4 Decomposition algorithm showing the downward and upward elimination in matrix  $G_1$ .

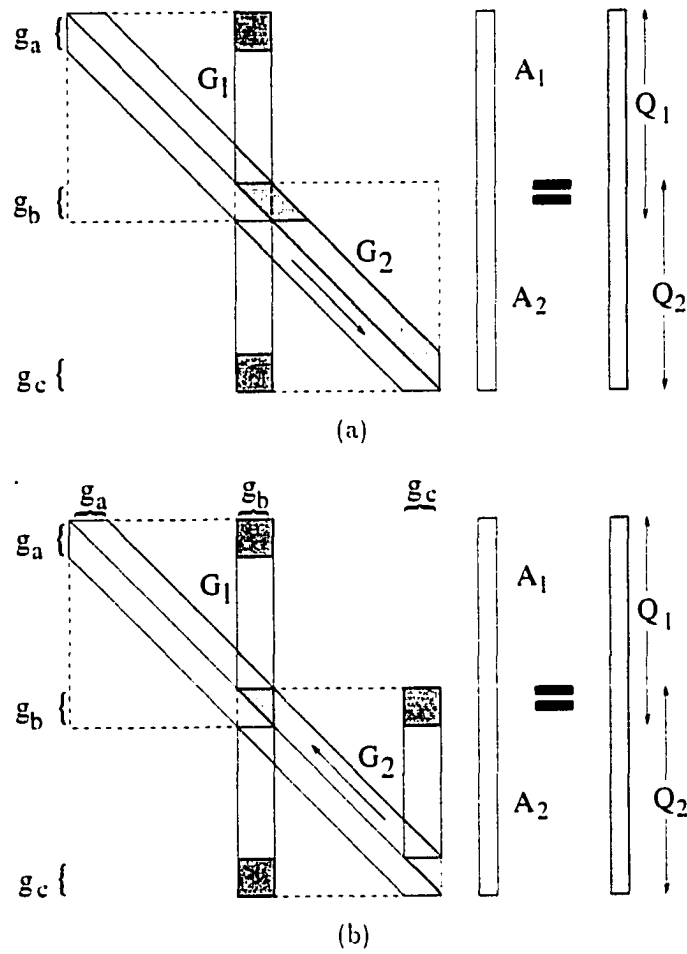


Figure 3.5 Decomposition algorithm showing the downward and upward elimination in matrix  $G_2$ .

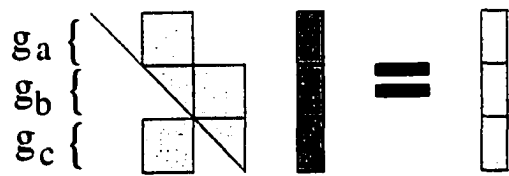


Figure 3.6 Assembly of nonzero entries in matrix  $G$  corresponding to variables indicated by  $y_a$ ,  $y_b$  and  $y_c$ .

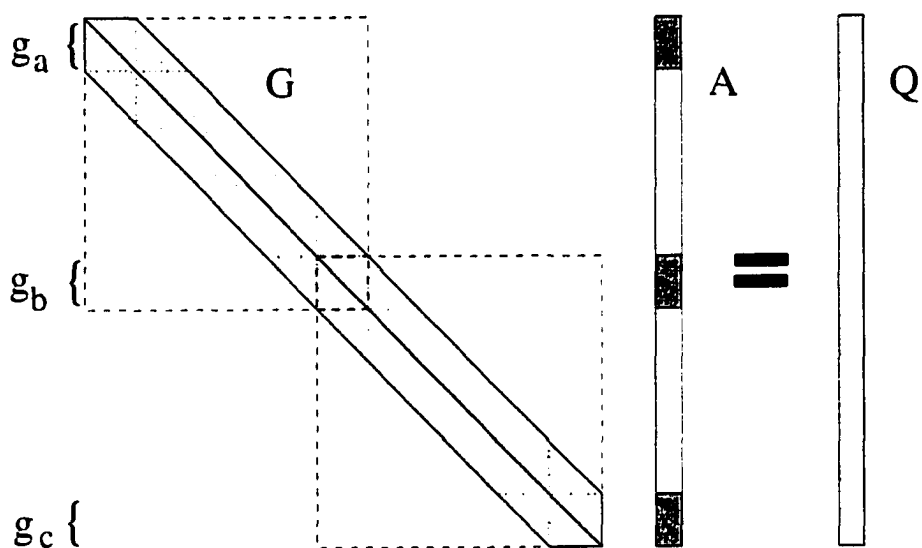


Figure 3.7 Assembly of nonzero entries in matrix  $G$  corresponding to variables indicated by  $g_a$ ,  $g_b$  and  $g_c$ .

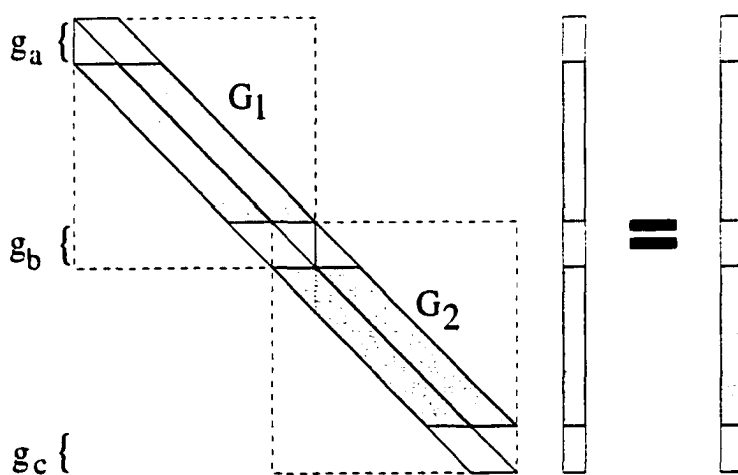


Figure 3.8 The unsolved part of the equation  $G.A = Q$ .

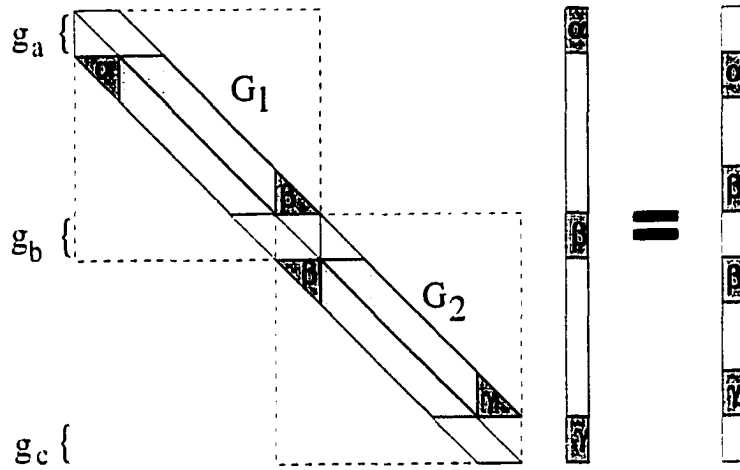


Figure 3.9 Partially computed  $A$  vector and its substitution in equation  $GA = Q$ .

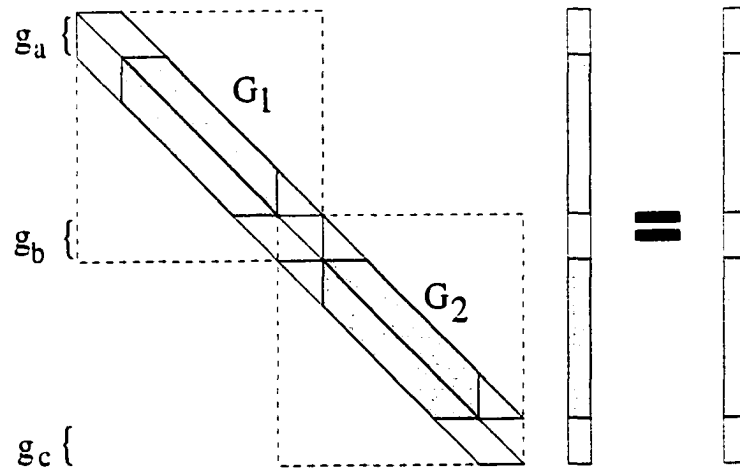


Figure 3.10 The effect of substituting the values of partially computed  $A$  vector into equation  $GA = Q$ .

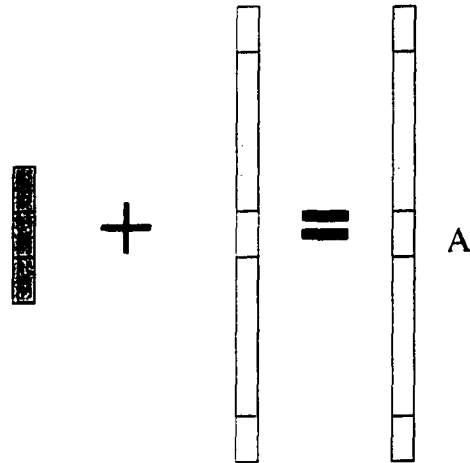


Figure 3.11 Assembly of the final solution vector  $A$ .

section can consume considerable computing resource. This process of decomposing the data (or domain) as represented by the  $G$  matrix can also be parallelized as described in the next section.

### Parallel Decomposition

The decomposition of the matrix  $G$  into decoupled submatrices  $G_1$  and  $G_2$  as depicted in Figure 3.9 can also be parallelized. Consider a stiffness matrix  $G$  as in Figure 3.12. The matrix is to be decomposed into three decoupled independent submatrices.

The algorithm to achieve this in parallel begins by creating three matrices  $G_1$ ,  $G_2$  and  $G_3$  as shown in Figure 3.12. These three submatrices can be decoupled and then solved in parallel. Figure 3.13 shows the 3 matrices that can be processed on 3 different processors. It is noted that the matrices are not square. The submatrices have overlap in data and hence communication will be required between the processors.

The matrices are eliminated downwards simultaneously (in parallel) as shown in Figure 3.14. This process creates vertical bands of nonzero entries called "fill in" in the submatrices as shown. The direction of elimination is indicated by the arrows and the "fill in" is indicated by the shaded areas.

Figure 3.15(a) shows the communication required at the end of downward elimination process. The first (1) processor does not receive any message and the last (3) processor does not send any message. All other processors send and receive data as indicated. Each of the data sent and received

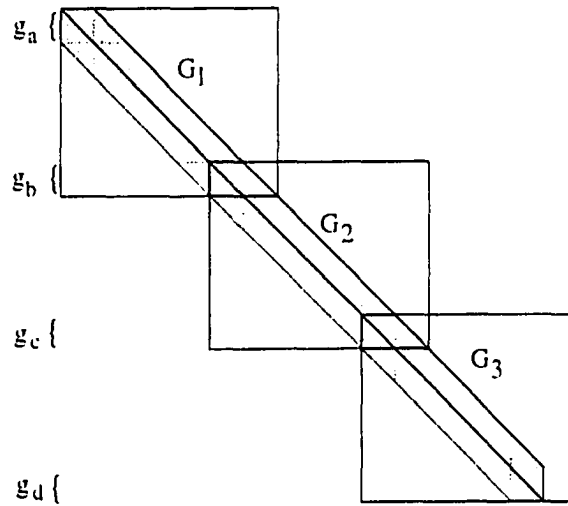


Figure 3.12 The  $G$  matrix decomposed into 3 submatrices.

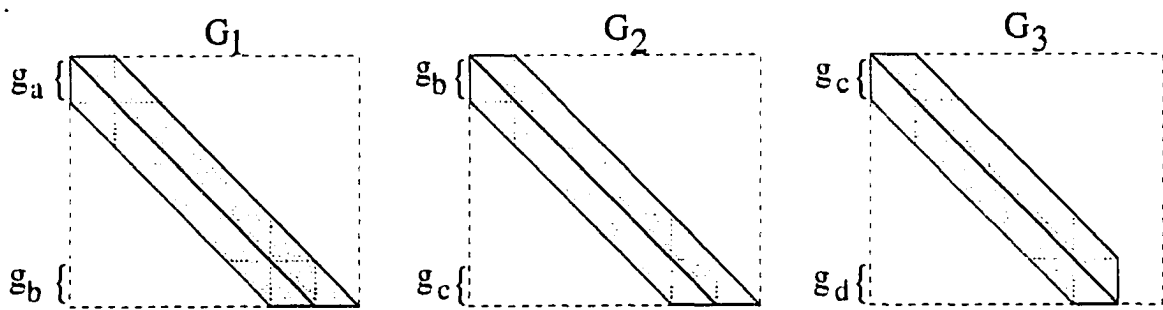


Figure 3.13 The  $G$  matrix decomposed into 3 submatrices to be processed on 3 different computer processors in parallel.

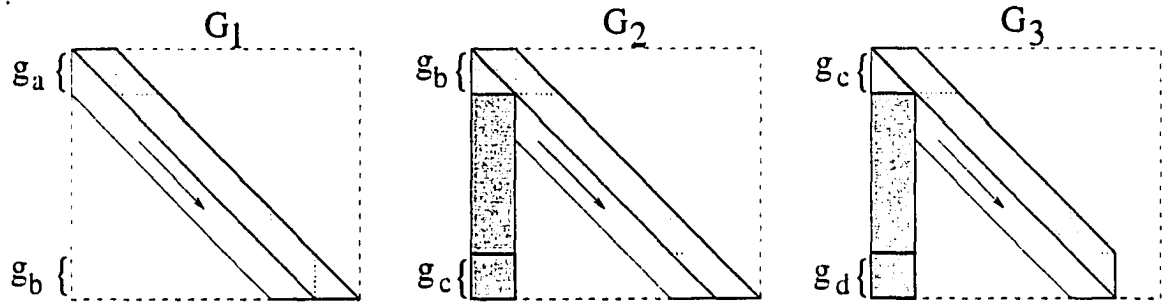


Figure 3.14 Parallel downward elimination of  $G_1$ ,  $G_2$  and  $G_3$ .

consists of blocks of data and is called the blocked send/receive. The processes do not proceed further until the communication is complete. Figure 3.15(b) shows the changed portion of the matrices after communication of data has been completed.

Figure 3.16 shows the simultaneous (parallel) upward elimination of the matrices  $G_1$ ,  $G_2$  and  $G_3$ . This creates vertical bands of nonzero entries in the matrices as indicated by the dark shaded area. This completes the elimination of the  $G$  matrix and  $Q$  vector in parallel using three processors. As described in the previous section the  $G$  matrix and  $Q$  vector corresponding to the variables  $g_a$ ,  $g_b$ ,  $g_c$  and  $g_d$  can now be assembled as these equations do not have a nonzero coefficient for any other variable.

Figure 3.17 shows the assembled portion of the entries in the  $G$  submatrices corresponding to the variables indicated by  $g_a$ ,  $g_b$ ,  $g_c$  and  $g_d$ . This set of linear equations is then solved to obtain a solution for parts of  $A$  vector as described in previous section. This partially computed  $A$  vector is then substituted into the original equation  $G \cdot A = Q$  to decouple the system of equations into three sets of equations of  $G_1 \cdot A_1 = Q_1$ ,  $G_2 \cdot A_2 = Q_2$  and  $G_3 \cdot A_3 = Q_3$ . These decoupled systems of linear equations are then solved in parallel using three processors.

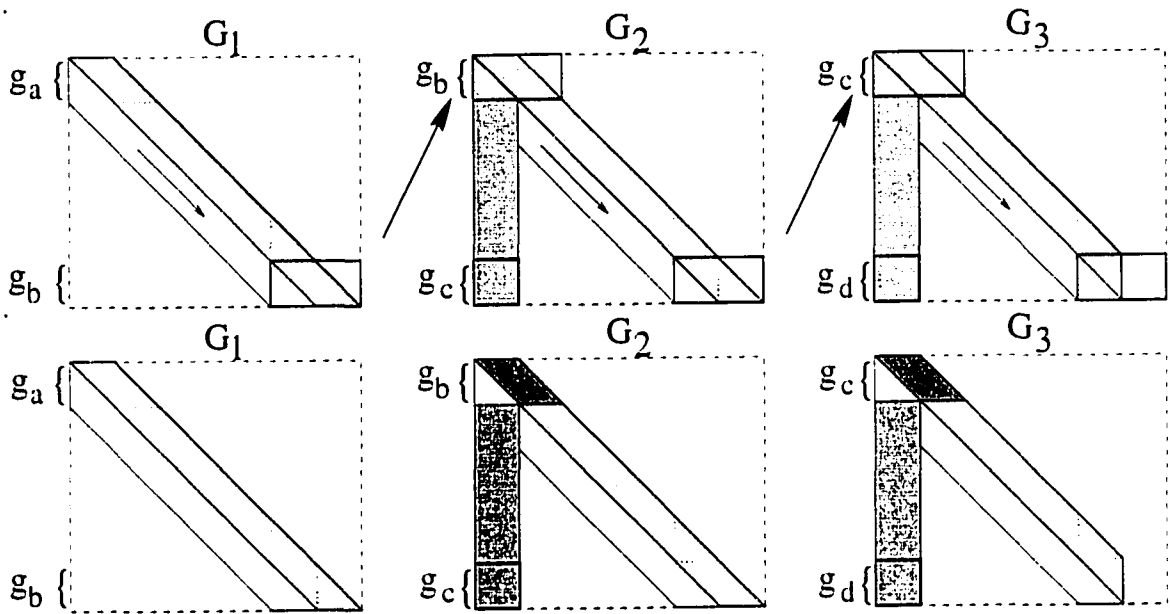


Figure 3.15 Inter process communication (blocked).

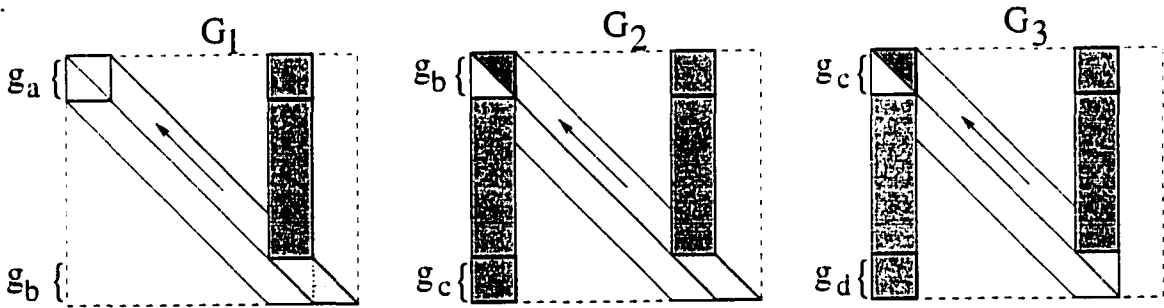


Figure 3.16 Parallel upward elimination of  $G_1$ ,  $G_2$  and  $G_3$ .

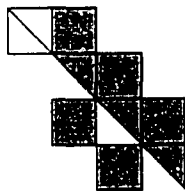


Figure 3.17 Parallel assembly of nonzero entries in matrix  $G$  corresponding to variables indicated by  $g_a$ ,  $g_b$ ,  $g_c$  and  $g_d$ .

## 4 EDGE EFFECT REDUCTION

This chapter discusses the design of probes for minimizing edge effects. The edge effect encountered in eddy current inspection of aircraft structures is described first in detail using both modeling and experimental results. This is followed by a study of shielding of eddy current probes, and the effectiveness of shielding for the application under consideration. Finally a flux focusing method using active compensation is described along with potential candidate design of eddy current probe for edge effect reduction.

### Edge Effect in Eddy Current Inspection

Very often cracks occur close to an edge in multilayer structures in aircraft frames. One of the challenging problems in the inspection of aircraft structures is the detection of flaws in the second layer in the vicinity of edges as shown in Figure 1.1. This is referred to as the *edge effect problem*. The edge effect is very pronounced at lower operating frequencies which are required for detection of flaws in thick samples. Low frequency eddy current (LFEC) probes are currently used in the inspection of subsurface fatigue cracks in aircraft frame structures [26]. However the interpretation of LFEC signals is rendered difficult by the proximity to hidden edges.

Aircraft structures consist of multiple layers with edges in the subsurface layers. Consequently the detection of defects in the second layer in the vicinity of edges is rendered difficult by the edge effect. A study of edge effect in multilayer geometry was conducted using a three dimensional finite element model. The sample consists of two aluminum plates with a defect in the lower plate close to a hidden edge. The test geometry is shown in Figure 4.1. The geometry shows that a half symmetry can be used to model and reduce the computing resources required. The boundary conditions on the plane of symmetry are applied by forcing the components of vector potential  $\vec{A}$  not normal to the plane to zero. Table 4.1 gives values of all the parameters used in the 3D finite element model.

Figure 4.2 shows the defect and edge signals in the impedance plane. It can be observed that the edge signal is very large compared to the defect signal. When the defect occurs close to an edge

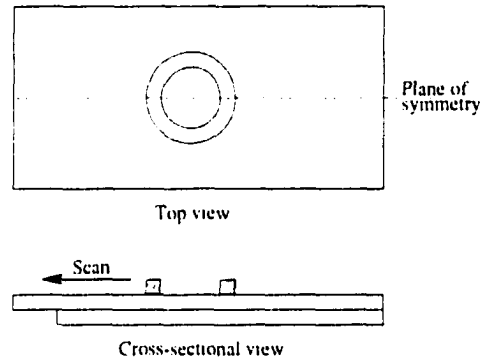


Figure 4.1 Test geometry for edge effect study.

Table 4.1 Numerical model parameters for edge effect modeling.

Parameter	Value
Probe coil radius $r$	4 mm
Coil cross-section	2 mm $\times$ 2 mm
Coil current density $J_s$	$10^6$ A/m
Sample (two Aluminum plates) size	100 mm $\times$ 100 mm $\times$ 2 mm
Defect size	4 mm $\times$ 2 mm $\times$ 1 mm (50%)
Edge to defect distance $d$	2 mm to 5 mm
Frequency $f$	1 and 5 kHz
Conductivity $\sigma_{Al}$ (Aluminum)	$1.8868e+07$ S/m
Permeability $\mu_r$ (Ferrite)	10000
Conductivity $\sigma_{Fe}$ (Ferrite)	100 S/m

in the second layer, the signal from the edge will completely mask the contribution from the defect.

Figure 4.3 presents signals from the probe at an operating frequency of 1kHz as the edge-to-defect distance  $d$  increases from 2mm to 5mm with (a)  $d=2$ mm, (b)  $d=3$ mm, (c)  $d=4$ mm and (d)  $d=5$ mm. The defect signal is completely masked by the edge contribution for  $d < 5$  mm in the composite edge+defect signal. The defect in the presence of the edge becomes more visible as  $d$  increases.

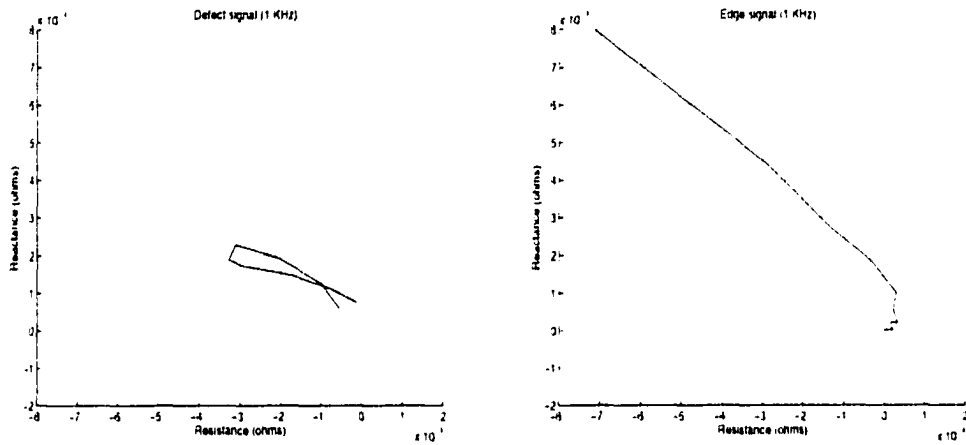


Figure 4.2 Defect and edge (numerical) signals for a coil at  $f=1$ kHz.

The model was used to compute probe signals at a higher frequency of 5 kHz. Figure 4.4 shows the defect and edge signals. The defect signal at this higher frequency is larger and rotated in phase. Figure 4.5 shows the experimental eddy current signal at 5 kHz at an edge-to-defect distance  $d$  of 3mm and 5mm. At this higher frequency the edge effect is seen to be less pronounced and there is a shift in the phase (angle or tilt) of the signal. At higher frequencies the probe can therefore be successful in detecting flaws closer to an edge than at lower frequencies. However, low frequency operation required for detection of flaws deeper inside material results in contradictory requirements. Consequently, the detection of flaws in the presence of edges in the second layer presents a major challenge.

The model-generated signals have been validated by experiments. The plots in Figure 4.6 are the experimentally measured defect and edge signals using a probe of radius 10mm at 1kHz. Figure 4.7 presents the experimental impedance plane plots for  $d = 3$  mm and  $d = 5$  mm. Comparing with Figure 4.5 it is seen that the experimental results validate the model predictions of the edge effect. A commonly used technique to minimize edge effect is shielding and is discussed in the next section.

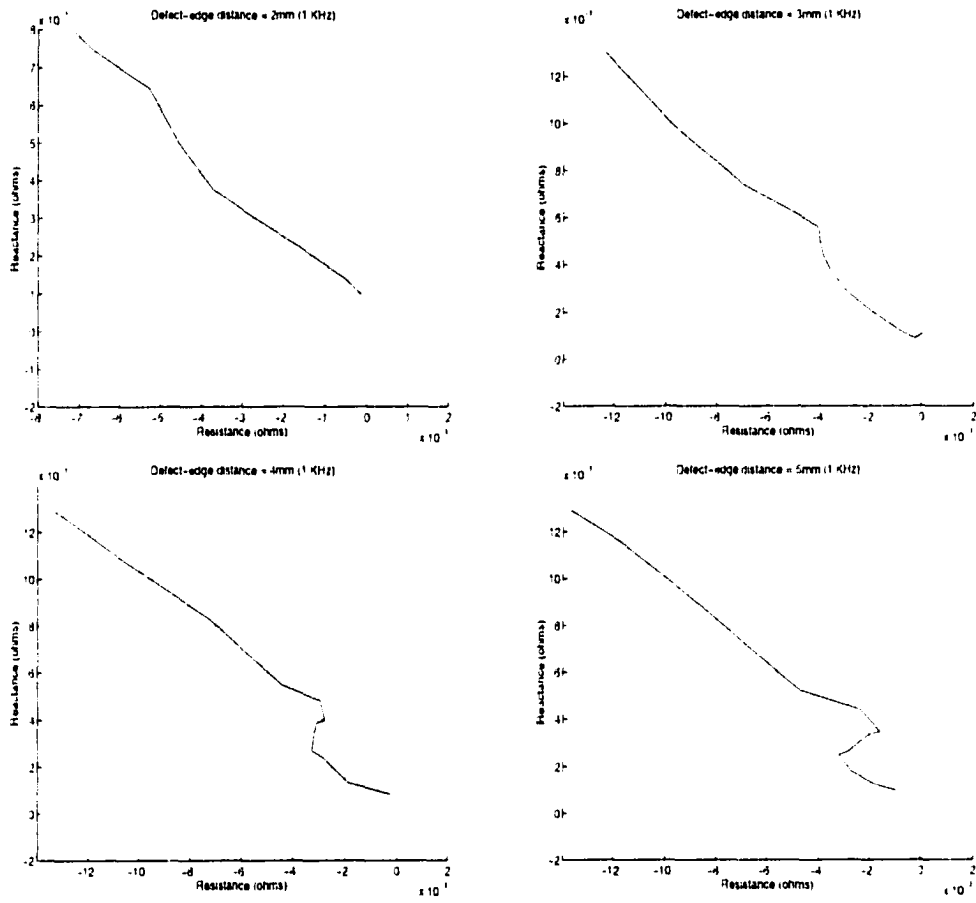


Figure 4.3 Edge effect (numerical) for a coil at  $f=1$  kHz.

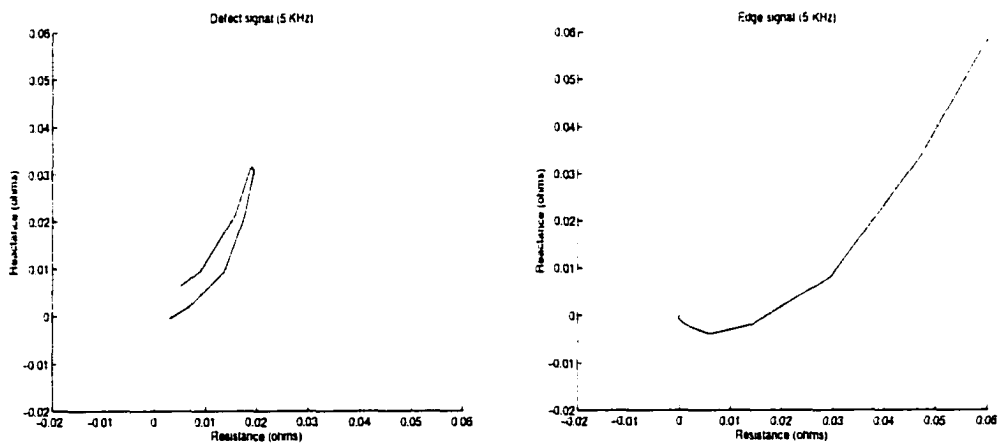


Figure 4.4 Defect and edge (numerical) signals for a coil at  $f=5$  kHz.

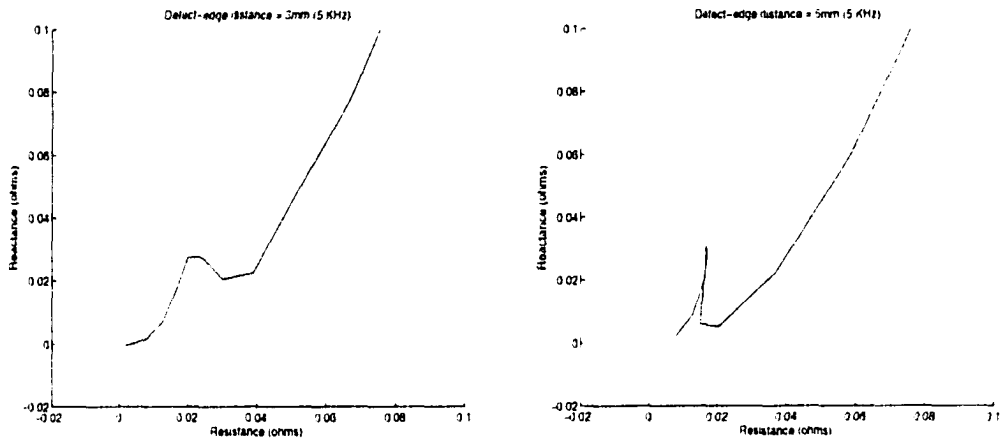


Figure 4.5 Edge effect (numerical) for a coil at  $f=5$  kHz.

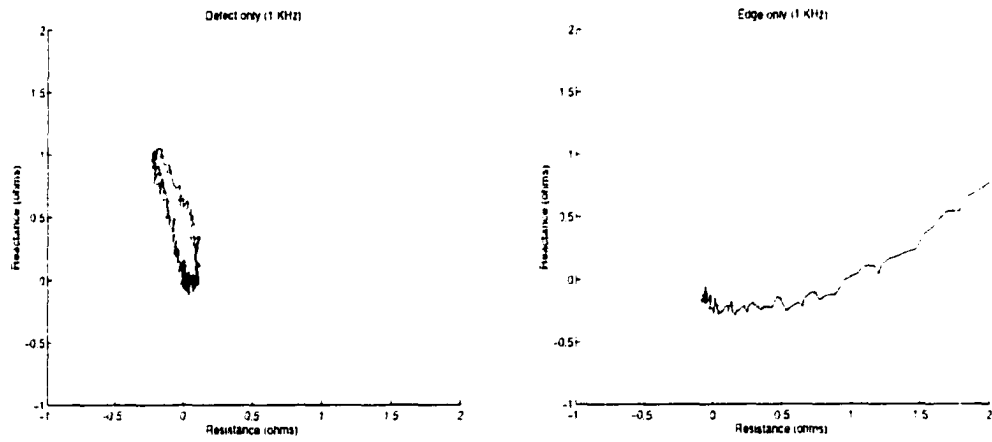


Figure 4.6 Defect and edge (experimental) signals for a 10mm coil at  $f=1$  kHz.

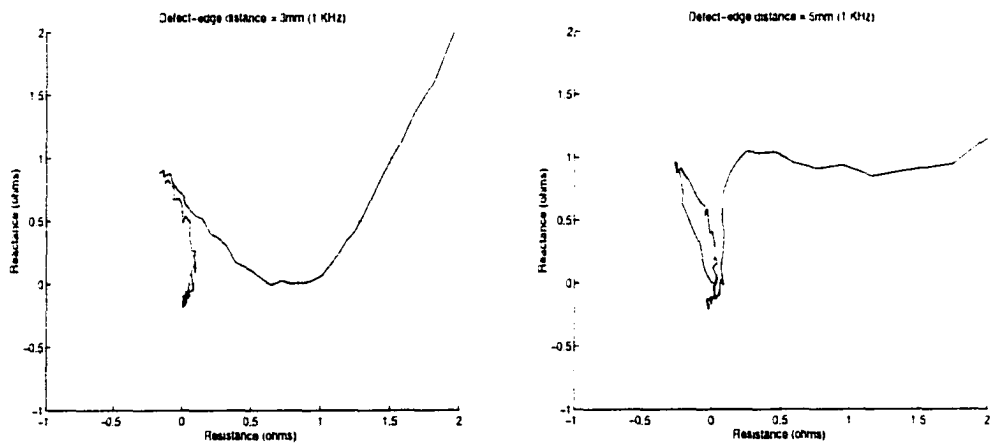


Figure 4.7 Edge effect (experimental) for a coil of 10mm radius at  $f=1$  kHz (a)  $d=3$ mm (b)  $d=5$ mm.

## Shielding of Eddy Current Probes

Low frequency eddy current testing is important in the detection of embedded flaws and corrosion in multilayer structures of the aircraft. In eddy current inspection the density of the induced eddy currents inside the conducting specimen is a function of the operating frequency ( $f$ ), material conductivity ( $\sigma$ ) and magnetic permeability ( $\mu$ ). These variables are used to define the skin depth (the standard depth of penetration)  $\delta_s$ , as:

$$\delta_s = \frac{1}{\sqrt{\pi f \mu \sigma}} \quad (1.1)$$

For a given sample with known magnetic permeability and conductivity the depth of penetration is controlled by the operating frequency. In order to detect defects at larger depths in the material low-frequency excitation has to be used.

The finite element model predictions of magnetic flux around a simple circular coil carrying a current is shown in Figure 4. The coil has a radius of 6 mm with a rectangular cross section of (4 mm  $\times$  8 mm).

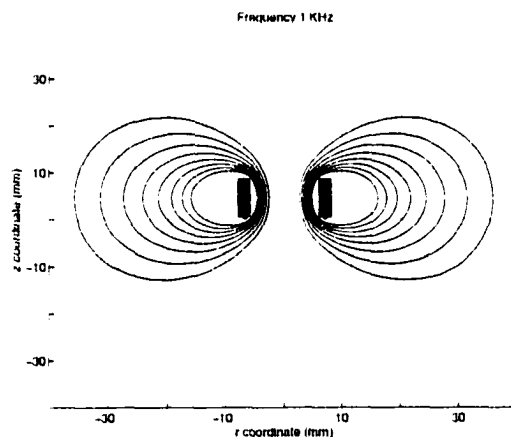


Figure 4.8 Magnetic flux for a simple circular coil carrying current.

The eddy current probe coil does not generate a plane electromagnetic wave and for this reason the standard depth of penetration is a material/test parameter rather than a true measure of penetration [12]. The *true depth of penetration*  $\delta_t$  besides depending on frequency, magnetic permeability and electrical conductivity, depends also on the sample thickness and the probe diameter. The depth in the sample at which the eddy current density drops to  $1/e$  (36.8%) of the density at the surface is called the true depth of penetration. The *effective depth of penetration*  $\delta_e$  is defined as the depth at which the current density decreases to  $1/e^3$  (4.9%) of the surface density. If the ratio  $\frac{R}{\delta_t} > 10$ .

where  $R$  is the mean coil radius, then  $\delta_e$  can be approximated as  $3\delta_s$ . If the ratio  $\frac{R}{\delta_s} < 10$ , which is usually true in eddy current testing, then the standard and true penetration depths are significantly different [12]. For practical design purposes the effective depth of penetration  $\delta_e$  is approximated as  $3\delta_s$ , even with  $\frac{R}{\delta_s} < 10$ .

The eddy current defect signal is the change in impedance (or voltage) of the probe coil as the probe scans the test sample. The impedance ( $Z$ ) of the coil is expressed as a complex sum of the resistance ( $R$ ) and inductive reactance ( $X_L$ ) expressed in terms of the frequency ( $\omega = 2\pi f$ ) and inductance ( $L$ ) as,

$$Z = R + jX_L = R + j\omega L. \quad (4.2)$$

The strength of the induced currents is proportional to the time rate of change of the exciting field and hence the induced currents are very large at high frequencies. At low frequencies ( $< 5\text{kHz}$ ) the induced eddy currents are relatively small in magnitude resulting in smaller eddy current signals. Consequently the defect signal can become too low for detection in the presence of noise. Since  $Z$  is proportional to  $R$  the signal can be increased by increasing  $R$ . However a very large resistance coil is also undesirable as it will require a high power source to drive it.

The inductive reactance ( $X_L = \omega L$ ) can be increased by increasing the inductance  $L$  which for a coil is directly proportional to the square of the coil diameter ( $D$ ) and the number of coil turns ( $N$ ),

$$L \propto N^2 D^2 \quad (4.3)$$

Both of these factors also increase the probe size. Consequently, if defects are smaller in dimensions relative to the probe diameter, the defect signals will be embedded in a large average coil signal and will be difficult to detect. The minimum size flaw that can be detected using a probe coil is thus limited by the coil diameter. An ideal probe coil used in eddy-current inspection should have a *small diameter, high inductance and low resistance* so as to be able to detect small flaws at larger depths in the sample at low frequencies.

At low frequencies the magnetic field around the coil of an eddy-current probe, often affects an area much larger than is desired [7]. In eddy current inspection the *probe footprint* is the area in the conducting sample in which the eddy currents are induced when the coil is excited. Theoretically a coil will have a footprint of infinite size, but for practice the area around the probe where the effect of the coil fields can be measured or has reduced to a certain fraction of the peak value is considered.

At high frequencies the footprint is small because of the skin effect, but at lower frequencies the footprint is large. A probe with a small footprint is desirable because it has a much better resolution

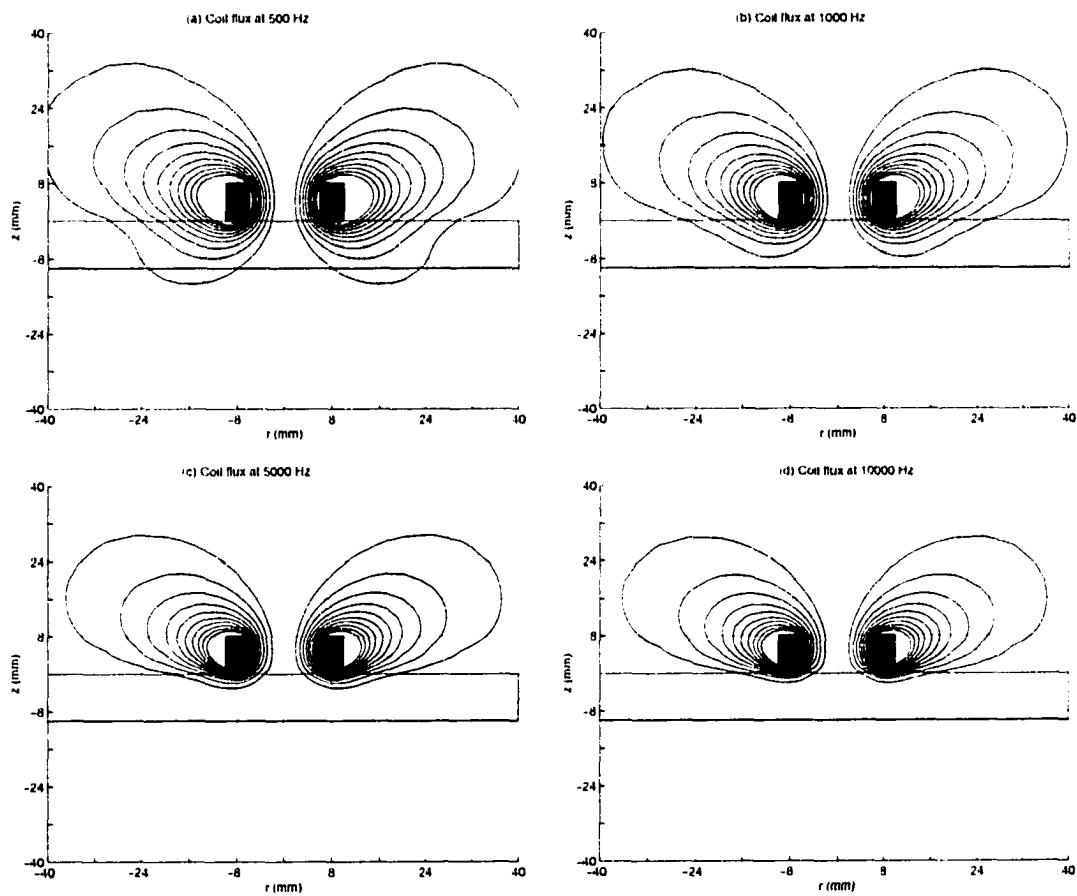


Figure 4.9 Flux plots of the coil at frequencies (a) 500Hz, (b) 1kHz, (c) 5KHz and (d) 10kHz.

capability than a probe with a large footprint. Figure 4.9 shows the flux plots of a coil on a 10mm thick aluminum sheet with changing frequencies. It is observed that the probe footprint decreases with increasing frequency.

One of the commonly used methods for reducing probe footprints is shielding where the probe is enclosed inside a material of high magnetic permeability ( $\mu$ ) or high conductivity ( $\sigma$ ) for magnetic and eddy current shielding, respectively. In eddy-current shielding a highly conducting material (copper) is used to enclose the probe. The skin effect causes the magnetic field to decay inside the shield thereby constraining the flux to a small area. A disadvantage of this shield is that the eddy currents generated in the conducting shield dissipate some of the energy and result in a net reduction in the field strength of the coil.

### ***Eddy Current Shielding***

The 2D finite element model was used to study the effectiveness of shielding and these results are presented here. Figure 4.10 shows the effect of frequency on eddy current shielding. A 2 mm thick copper shield is used to shield a coil of radius 6 mm in generating the flux plots in Figure 4.10. It is seen that the shielding effect is more pronounced at higher frequencies and hence the shielding is more effective. At lower frequencies (below 1kHz) the shielding effects are negligible and this method of shielding fails.

Figure 4.11 shows the influence of shield thickness on the shielding effect (eddy current). The effectiveness of shielding can be enhanced by increasing the conductivity and thickness of the shield. Increasing the thickness of the shield increases the size of the probe and it also adds bulk.

### ***Magnetic Shielding***

Magnetic shielding focuses the magnetic flux to a smaller area and also increases the net magnetic field strength. Figure 4.12 shows the effect of frequency on magnetic shielding. A 2 mm thick ferromagnetic material of relative permeability  $\mu_r = 15000$  and conductivity  $\sigma = 0$  S/m is used to shield a coil of radius 6 mm. The ferromagnetic material provides a path of low reluctance to the magnetic flux and as a result focuses the magnetic field.

The effectiveness of magnetic shielding can be increased by using a shielding material of higher

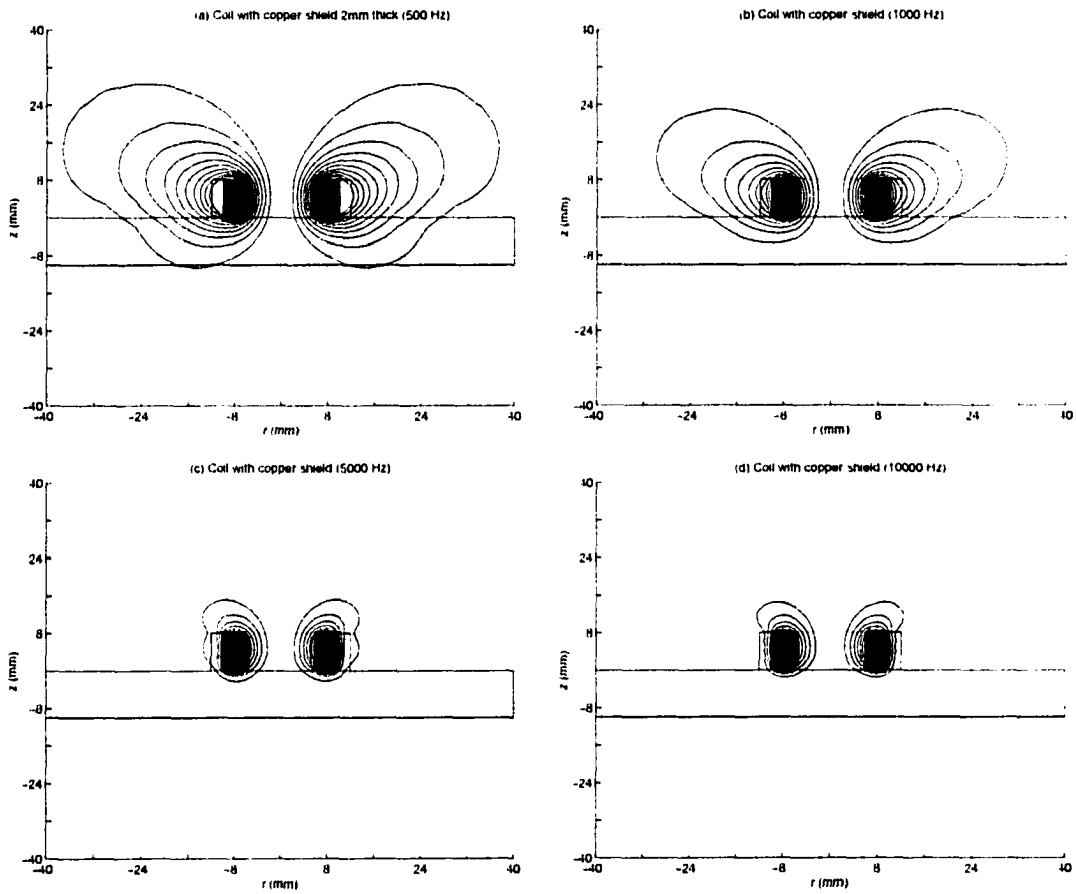


Figure 4.10 Field distribution around a coil with copper shield (2mm thick) at frequencies (a) 500Hz, (b) 1kHz, (c) 5kHz and (d) 10kHz.

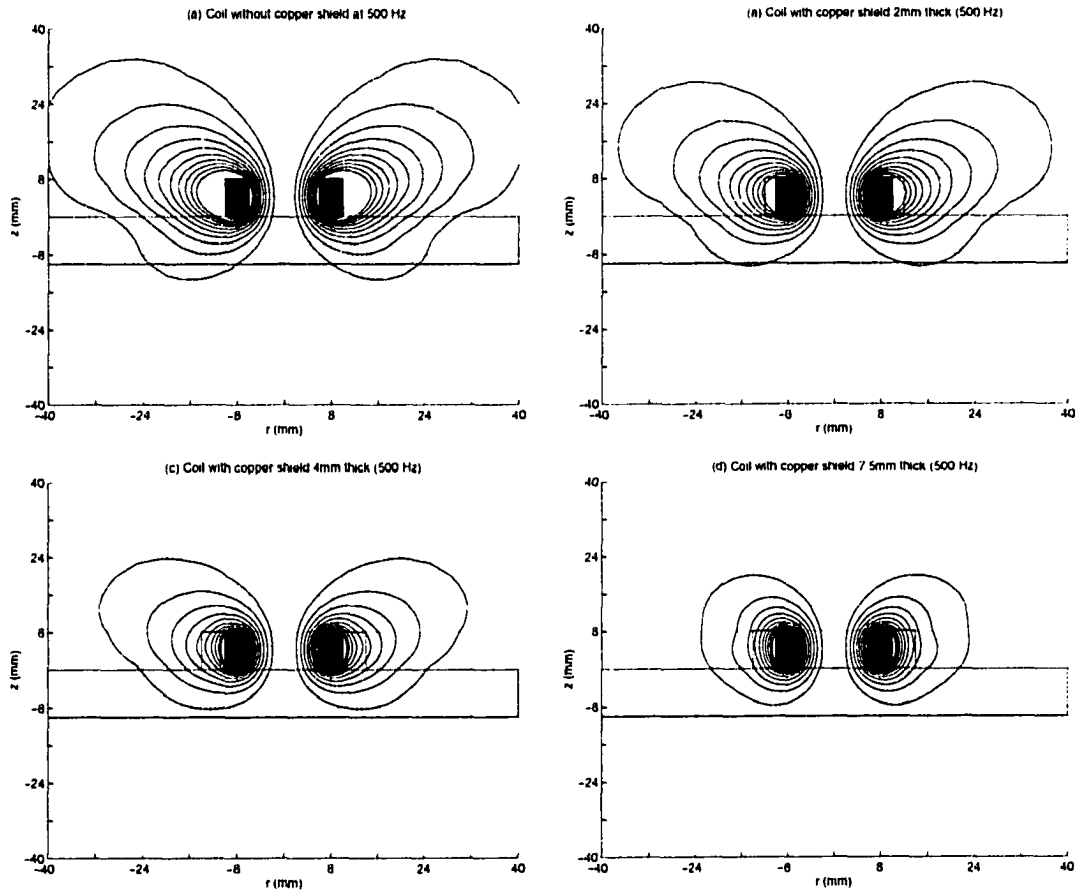


Figure 4.11 Coil with copper shield with thickness ( $f=500$  Hz) (a) 0mm, (b) 2mm, (c) 4mm and (d) 7.5 mm.

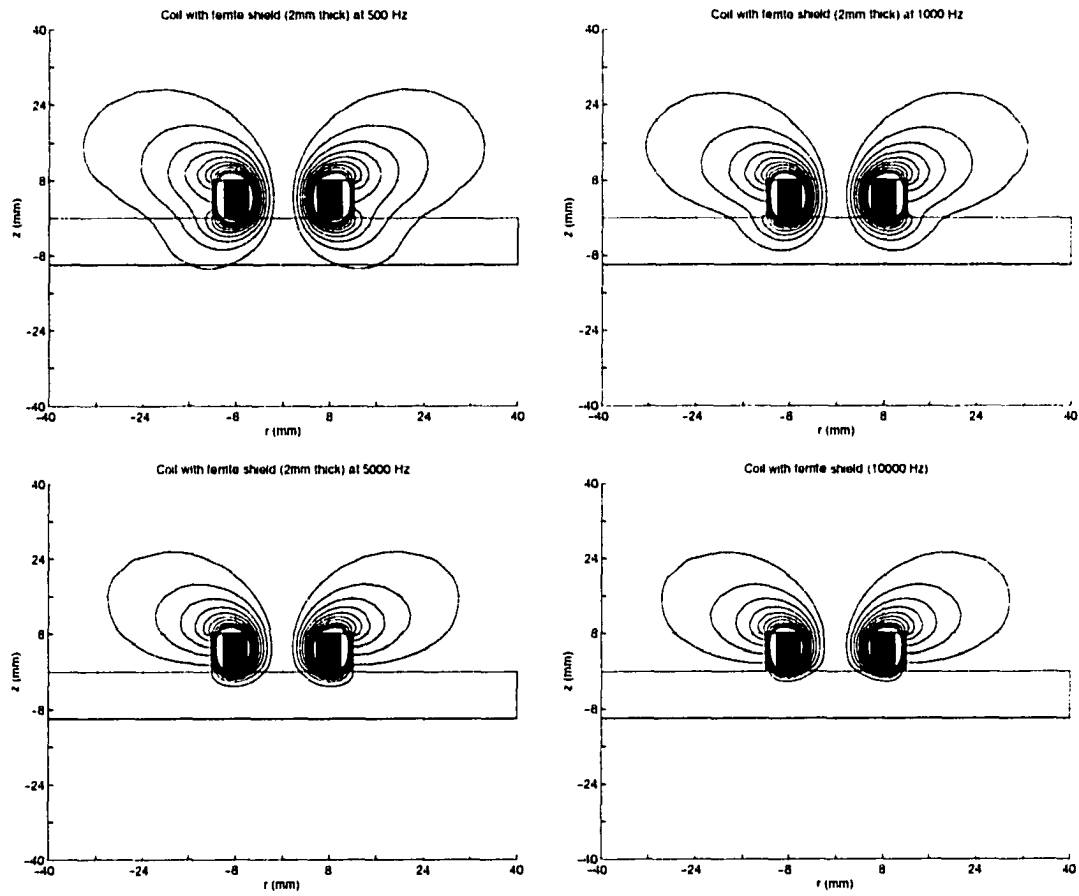


Figure 4.12 Effect of frequency on a shielded coil. Thickness of shield= 2 mm and frequency is (a) 500Hz, (b) 1kHz, (c) 5kHz and (d) 10kHz.

permeability and increasing the shield thickness. Different materials show different shielding properties. Materials such as steel, Mu metal and ferrites have been commonly used as shielding materials. Ferrite shields possessing lowest conductivity are most sensitive to flaws whereas metallic shields with high conductivity are less sensitive. The metal shields have eddy currents induced in them and thus the net field can be reduced in magnitude considerably which leads to a lower sensitivity. Ferrite shields on the other hand will increase the total field strength. Mu metal shields have intermediate properties, but it being a metal is preferred to ferrite shields.

The edge effect can be reduced with the use of appropriate shielding, which reduces the footprint size of the probe. The finite element model was used to study the effect of shielding on the edge effects. Both magnetic and eddy current shielding were modeled for evaluating this effectiveness in reducing edge effect. The geometry is similar to that described in Figure 4.1 with an external shield being added to the probe coil. The probe is then used to scan a defect in the second layer in the vicinity of an edge. These results are presented in Figures 4.13 to 4.16.

Figures 4.13 and 4.14 show the composite 'edge+defect' signals using a probe with a copper shield, at a frequency of 1kHz and 5kHz respectively. In Figure 4.13(a) the edge to defect distance  $d$  is 3 mm and the probe diameter is 10mm. The distance  $d$  is increased to 5 mm in Figure 4.13(b). The defect in the composite signal can be visually detected at the higher frequency (5kHz). The effectiveness of copper shielding is observed to be better at higher frequencies.

The copper shield was replaced with a ferrite shield and the new signals were computed. Figures 4.15 show the composite 'edge+defect' signal obtained using a probe with a ferrite shield at a frequency of 1kHz for an edge-to-defect distance  $d = 3$  and 5 mm. In Figure 4.15(a) the edge to defect distance  $d$  is 3 mm and the probe diameter is 10 mm. The distance  $d$  is increased to 5 mm in Figure 4.15(b). Figures 4.14 show the corresponding plots at 5kHz. In general shielding is observed to be more effective at higher frequencies.

Low-frequency eddy-current probes required for inspection of embedded flaws have large footprints and suffer from severe edge effects. It is difficult to use such probes to detect flaws close to the edges in the samples. Conventionally cylindrical ferrite shields have been used to enclose the regular unshielded probes to constrain the flux close to the probe. However, this shielding action is only in air. These shields are not very effective in reducing the field spread inside the conducting samples. The method of active shielding and its use to reduce probe footprint size is demonstrated as an alternate technique in the next section. This method is independent of the frequency of operation and can be effectively used with low frequency probes.

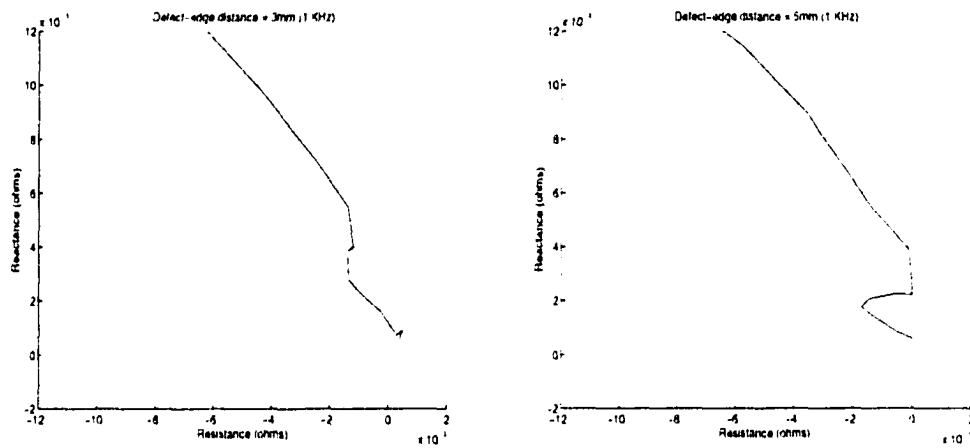


Figure 4.13 Edge effect (numerical) for a coil with a copper shield ( $f = 1\text{kHz}$ ).

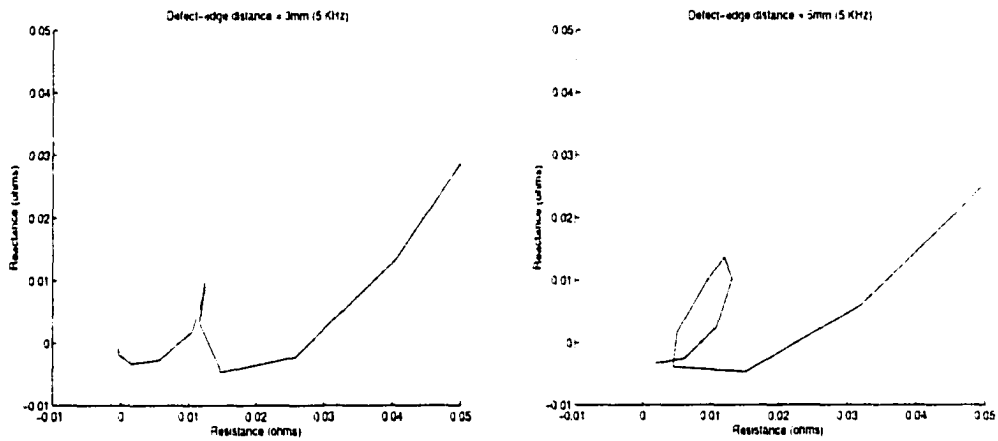


Figure 4.14 Edge effect (numerical) for a coil with a copper shield ( $f = 5\text{kHz}$ ).

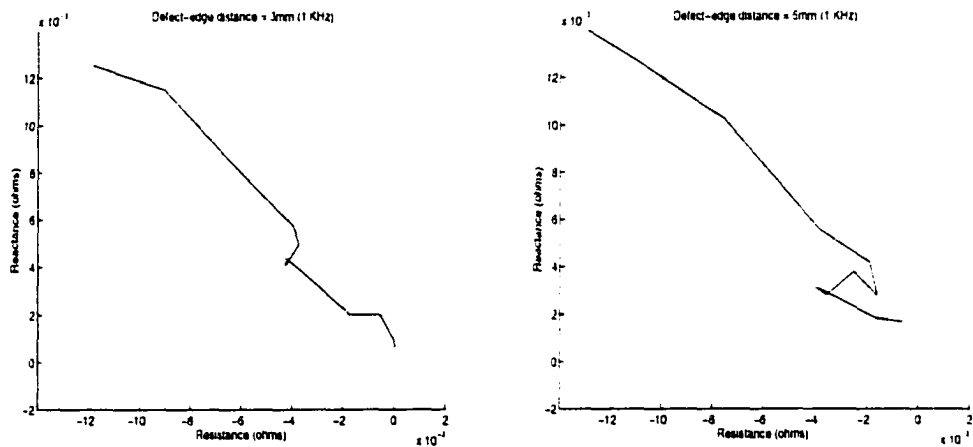


Figure 4.15 Edge effect (numerical) for a coil with a ferrite shield ( $f = 1\text{kHz}$ ).

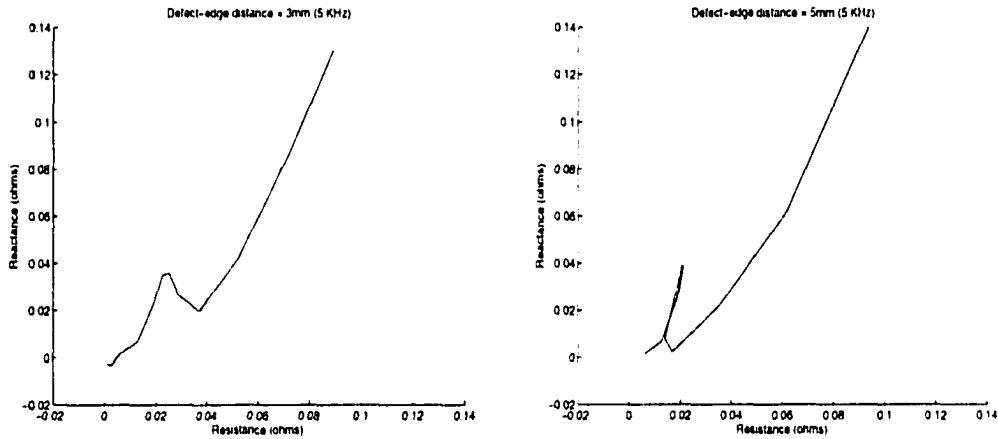


Figure 4.16 Edge effect (numerical) for a coil with a ferrite shield ( $f = 5\text{kHz}$ ).

### Flux Shaping Probe (A)

As seen in the last section, magnetic shielding of probe coils is effective in focusing the magnetic flux only in air. In the application under consideration it is required to focus the flux inside the metallic test specimen. The approach presented in this section is based on *active compensation*. Active compensation is a method that can be used to achieve shielding where the magnetic field is canceled in the desired area by superposition of another external field. This method has been used to make magnetically shielded rooms. This approach for magnetic flux shaping and focusing has been exploited for designing probes that reduce edge effects.

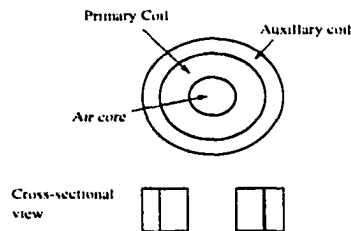


Figure 4.17 Geometry of the designed probe with reduced edge effect using a pair of concentric coils.

This approach uses an auxiliary coil carrying a current which is different in magnitude and direction from that of the primary coil. The field distributions inside the test object can be controlled by varying the relative magnitude and direction of the currents in the coils. An outer coil, concentric with the primary coil was used as an auxiliary coil for compensating the fields inside the sample. A schematic of the coil geometry is shown in Figure 4.17 along with the cross-sectional view. The auxiliary coil also carries a current and its field serves to alter the field of the primary coil. The net spatial field distribution in the test specimen can be controlled by varying the magnitude and direction of the current in the auxiliary coil with respect to the primary coil.

The total field distribution in the conducting layers was studied for a variety of design parameter values namely, (i) magnitude, (ii) direction of current in the coils, (iii) the coil cross-sectional areas and (iv) coil positions. The cross-sectional geometry of the auxiliary and primary coils are crucial for defining the net field distribution. The two concentric coil configuration has an axis of symmetry and hence the 2D finite element model can be used to obtain the magnetic flux pattern associated with the different design parameters. Four candidate probe geometries placed over an aluminum test sample shown in Figure 4 were modeled.

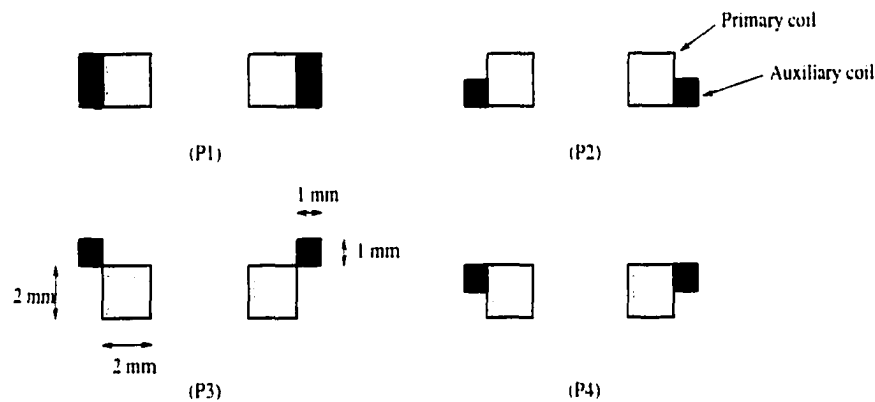


Figure 4.18 Candidate probes (P1,P2,P3,P4) showing the primary and auxiliary coils configurations.

Figure 4.19(a) shows a two coil probe with auxiliary and primary coils of different cross-sectional areas with a phase difference of  $180^\circ$ . In Figure 4.19(b), (c) and (d) the auxiliary coil with an out-of-phase current has half the area of the primary coil and the location of the auxiliary coil with respect to the primary coil is as shown in the figure. Figure 4.20 shows the effect of changing the phase difference between the primary and auxiliary coils. In Figure 4.20(a) the phase difference is

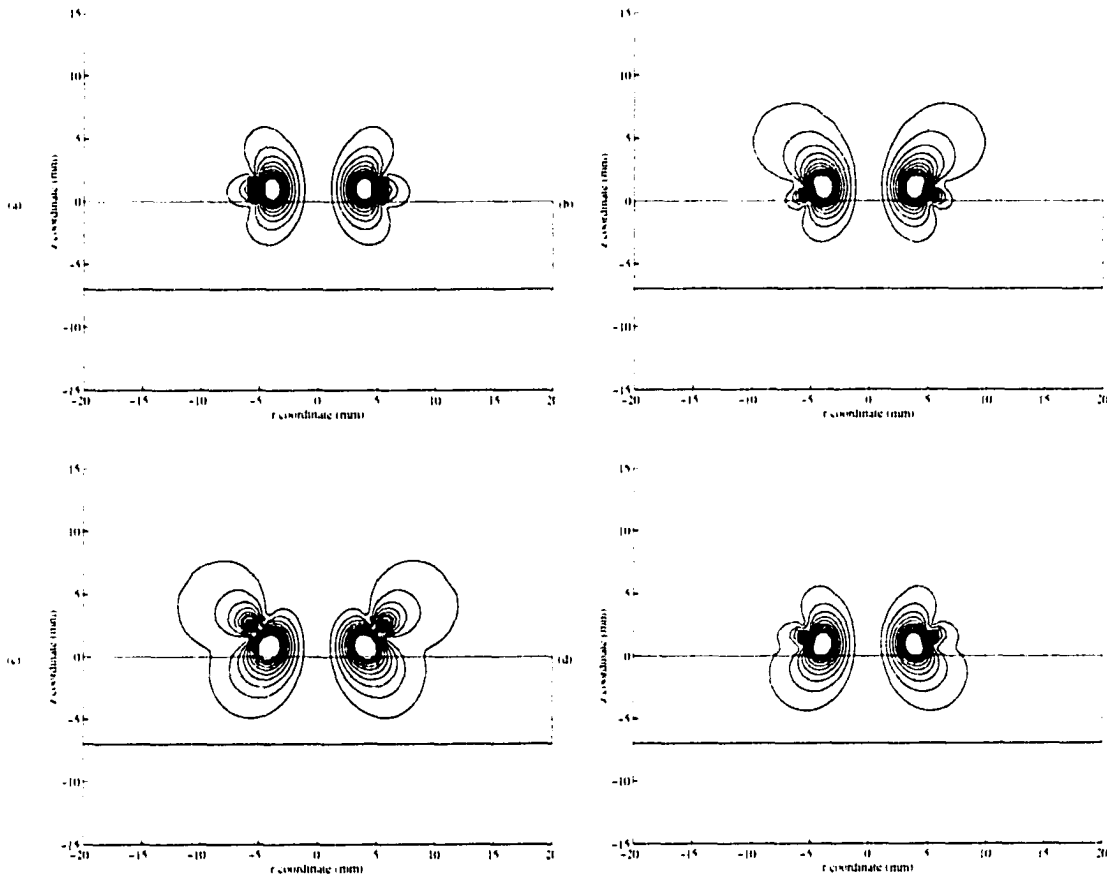


Figure 4.19 Flux focusing using the probes (P1,P2,P3 and P4)

Choosing the phase difference between the currents in the two coils to be  $180^\circ$  the finite element model predicted flux plots are presented in Figure 4.19. On examining the results in Figure 4.19 it is seen that the most compact flux distribution is obtained for candidate P1. Correspondingly the eddy current density inside the specimen is also localized. A probe based on this configuration of coils was used in further study.

Figures 4.20(a) and (b) show the magnetic field distribution of the probe with coil configuration P1 and a phase difference of (a)  $160^\circ$  and (b)  $170^\circ$  between the currents in the primary and auxiliary coils. As the difference between the phase of the primary and auxiliary currents is increased the total field strength reduces both in magnitude and in the area over which it spreads. The current density magnitude in both the primary and auxiliary coil is  $5\text{ A/mm}^2$ . Keeping the primary coil current density at  $5\text{ A/mm}^2$  and a relative phase difference fixed at  $180^\circ$ , the magnitude of the auxiliary coil current density was varied. Figures 4.21(a) and (b) show the corresponding results for auxiliary coil current density of (a)  $4\text{ A/mm}^2$  and (b)  $6\text{ A/mm}^2$ . These studies show that the

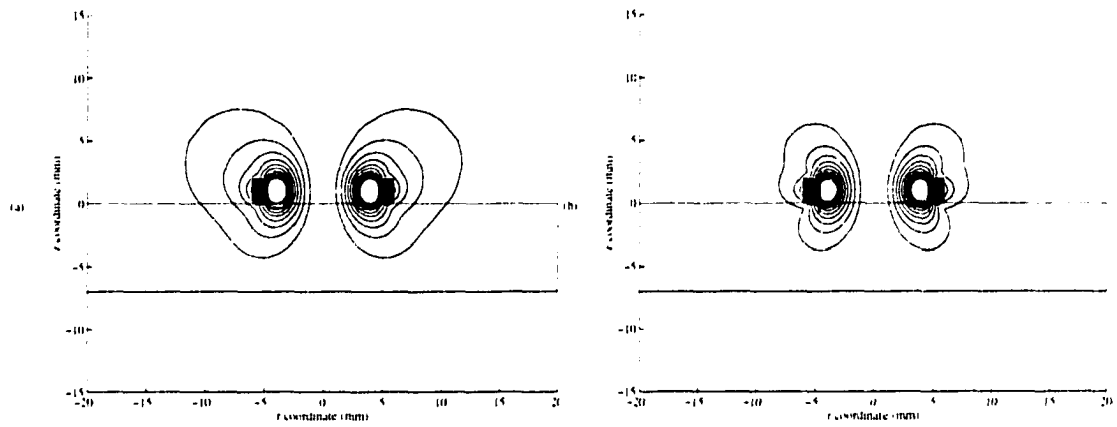


Figure 4.20 Flux focusing (candidate P1) with variable current phase in the auxiliary.

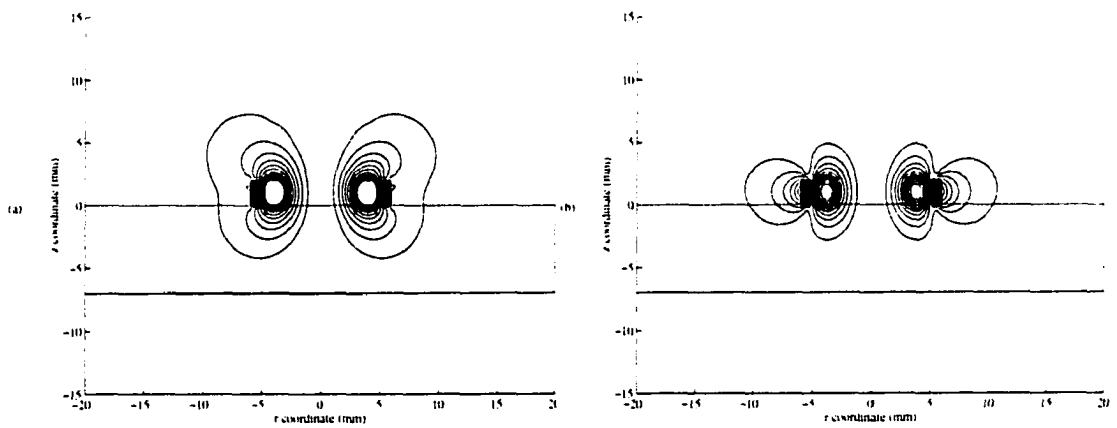


Figure 4.21 Flux focusing (candidate P1) with variable current magnitude in the auxiliary.

total flux distribution is very sensitive to the phase and magnitude differences of the primary and auxiliary coil currents. The optimal design for a probe with least footprint was obtained with a phase difference of  $180^\circ$  and equal magnitude of currents in the two coils.

The probe design obtained from this study was used to predict the signal from a flaw in close proximity to an edge. The probe geometry is shown in Figure 4.22. The probe consists of two concentric coils with the auxiliary coil on the outside of the primary coil. The primary and auxiliary coils have a radius of 4mm and 5.5mm respectively. The auxiliary coil carries a current in a direction that is opposite to that of the current in the primary coil.

Since a flaw signal requires scanning a defect with a probe, a full 3D finite element model is needed at each probe position.

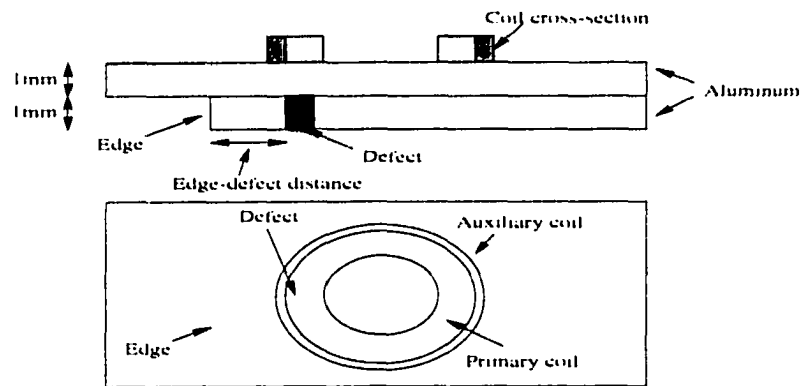


Figure 4.22 Geometry used to model the multilayer sample with defect in the second layer close to the edge showing the (a) top view and (b) the cross-sectional view.

The inspection geometry consists of the probe on a two layered aluminum sample (each 1mm thick) with an edge in the second layer and a defect (2mm  $\times$  2mm  $\times$  1mm) at a distance from an edge as shown in Figure 4.22. The change in the impedance of the primary/pickup coil is detected as a signal to indicate the presence of flaws in the sample being inspected. The impedance plane plots as obtained from the numerical model for a conventional eddy current probe and the probe candidate P1 are presented for various edge-to-defect distances  $d$  in the Figures 4.23 and 4.24.

Figures 4.23(a), (b), (c) (d) present the model predictions of the impedance plane plots for a conventional eddy current probe at 'edge-to-defect' distances  $d$  ranging from (a) 2 mm, (b) 3 mm, (c) 4 mm and (d) 5 mm. The impedance plane trajectories are obtained as follows. The probe signal for a scan over the sample is computed for each of the three cases: sample with defect alone (dotted and dashed loop), sample with edge alone (dotted line) and, sample with both edge and defect

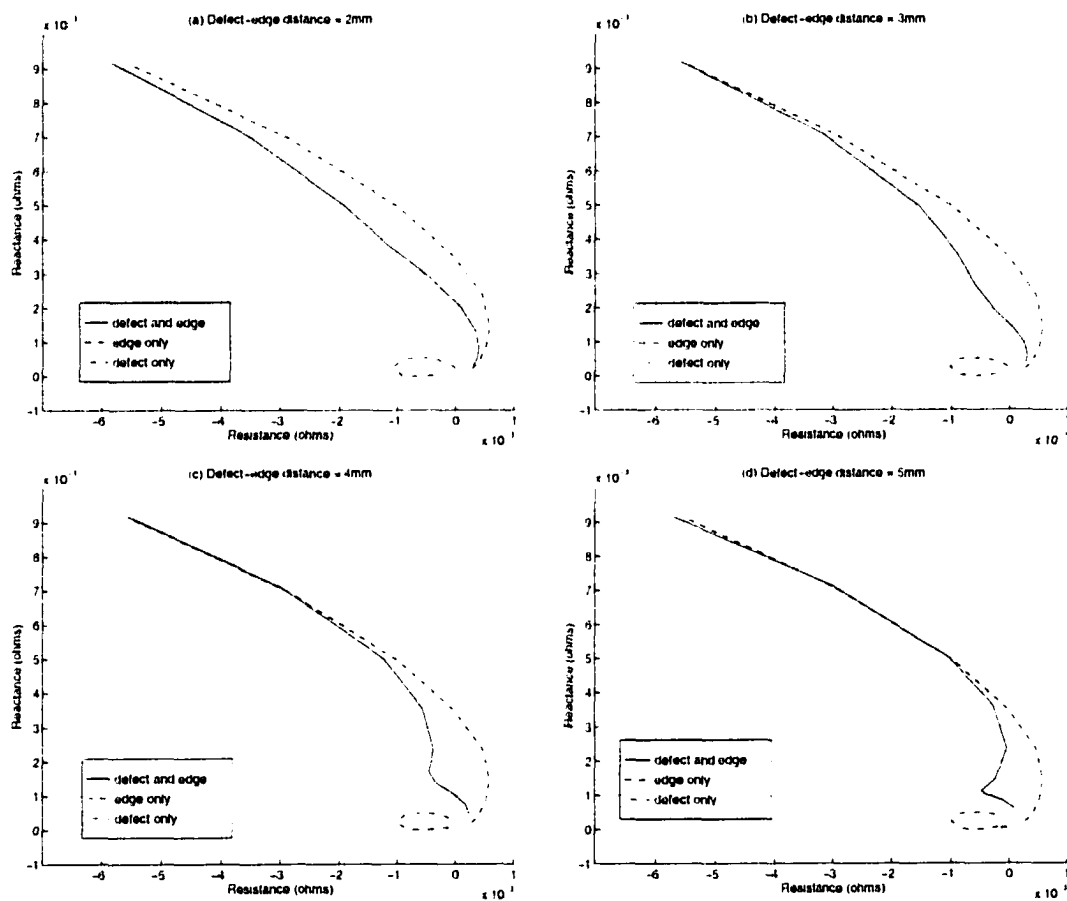


Figure 4.23 Impedance plane plots for the conventional EC probe for different edge to defect distance  $d$  at a frequency of 1KHz. (a)  $d=2\text{mm}$ , (b)  $d=3\text{mm}$ , (c)  $d=4\text{mm}$  and (d)  $d=5\text{mm}$ .

(continuous line). The coil impedance is obtained for the probe on the aluminum plates without a defect or edge in the sample and subtracted from each of the three scan signals obtained. This procedure simulates the nulling effect so that the trajectories begin at the origin. Figure 4.24(a), (b), (c) and (d) present the corresponding signals for the proposed probe  $P_1$  where the cross-sectional area of the auxiliary coil and the primary coil area is equal and they have currents of equal magnitude but opposite in phase.

A comparison of the results in Figures 4.23 and 4.24 indicate that the proposed probe design shows increased sensitivity compared to that of a conventional probe. The presence of a defect at a distance of 3 mm from the edge can be detected using the new probe whereas the impedance plane-plot for the conventional eddy-current probe in Figure 4.23 does not indicate the presence of the defect clearly. The 3D modeling results clearly show that it is possible to resolve a defect from an edge at an edge-defect distance of 5mm using a probe of 10mm diameter with an auxiliary coil of diameter 11mm.

The numerical model has been further used to study the effect of frequency on the performance of the probe. Figure 4.25 shows the impedance plane trajectories for an edge to defect distance of 3 mm at frequencies of (a) 1 KHz, (b) 3 KHz, (c) 5 KHz and (d) 10 KHz. The plots indicate that as the frequency decreases the defect becomes less visible in the composite edge-defect signal. The change in frequency also results in a shift of phase of the signal. A clockwise rotation of the signals with increase in frequency is observed. Using the numerical model to optimize the design a prototype probe was built and used to obtain experimental signals. These results are described next.

## Experimental Results

The probe design obtained using the numerical model was built and used for experimental validation of the proposed approach. A schematic of the probe is shown in Figure 4.26. In order to enhance the signal to noise ratio (SNR) of defect signals the probe is configured in a differential mode, using primary and reference coils.

The probe consists of three coils: the primary test coil ( $L_1$ ), the reference coil ( $L_2$ ) and the auxiliary coil which is divided into two, the lower ( $L_3$ ) and the upper ( $L_4$ ) coils. The coil connections are as shown in Figure 4.27. The primary test coil and the reference coil have the same number of turns ( $N=600$ ). The auxiliary coils have  $N/2$  turns each.

This arrangement is required to maintain the impedance of each of the three coils to be equal.

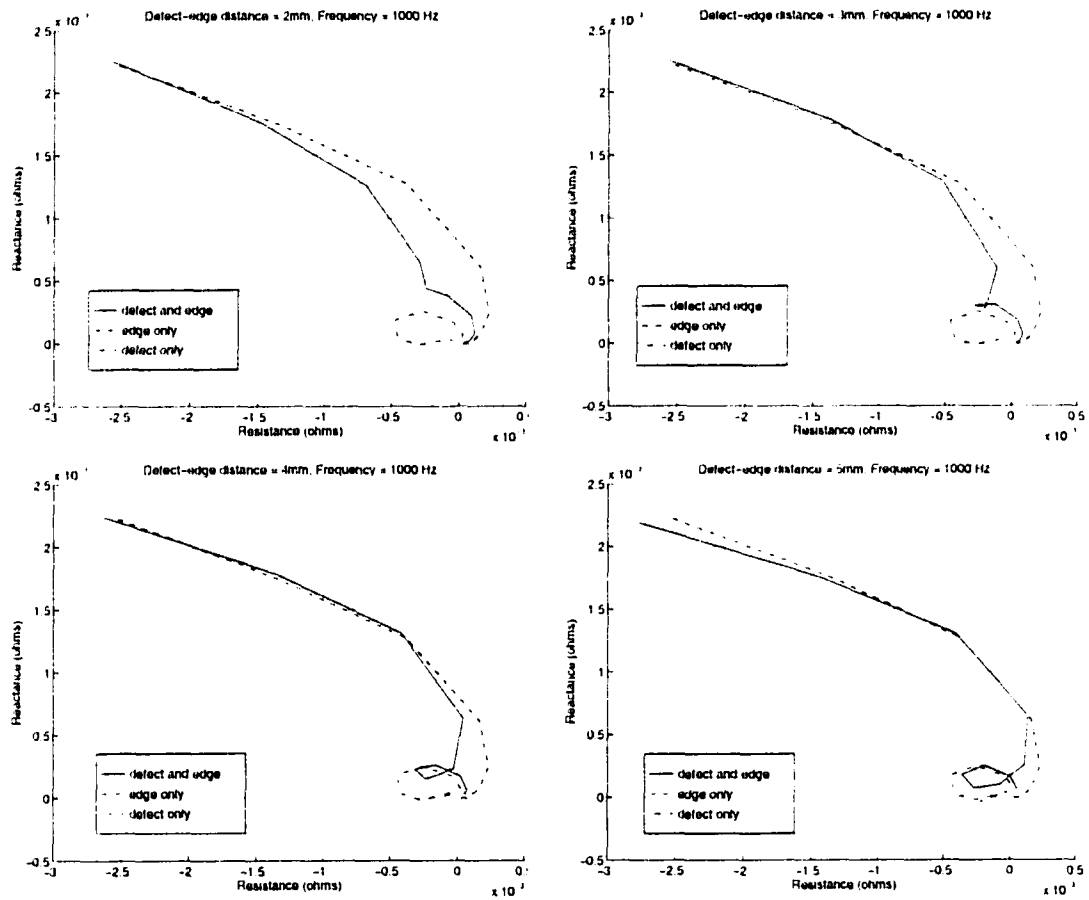


Figure 4.24 Impedance plane plots for the new probe  $P_1$  with the auxiliary coil with changing edge to defect distance  $d$  at a frequency of 1KHz. (a)  $d=2\text{mm}$ , (b)  $d=3\text{mm}$ , (c)  $d=4\text{mm}$  and (d)  $d=5\text{mm}$ .

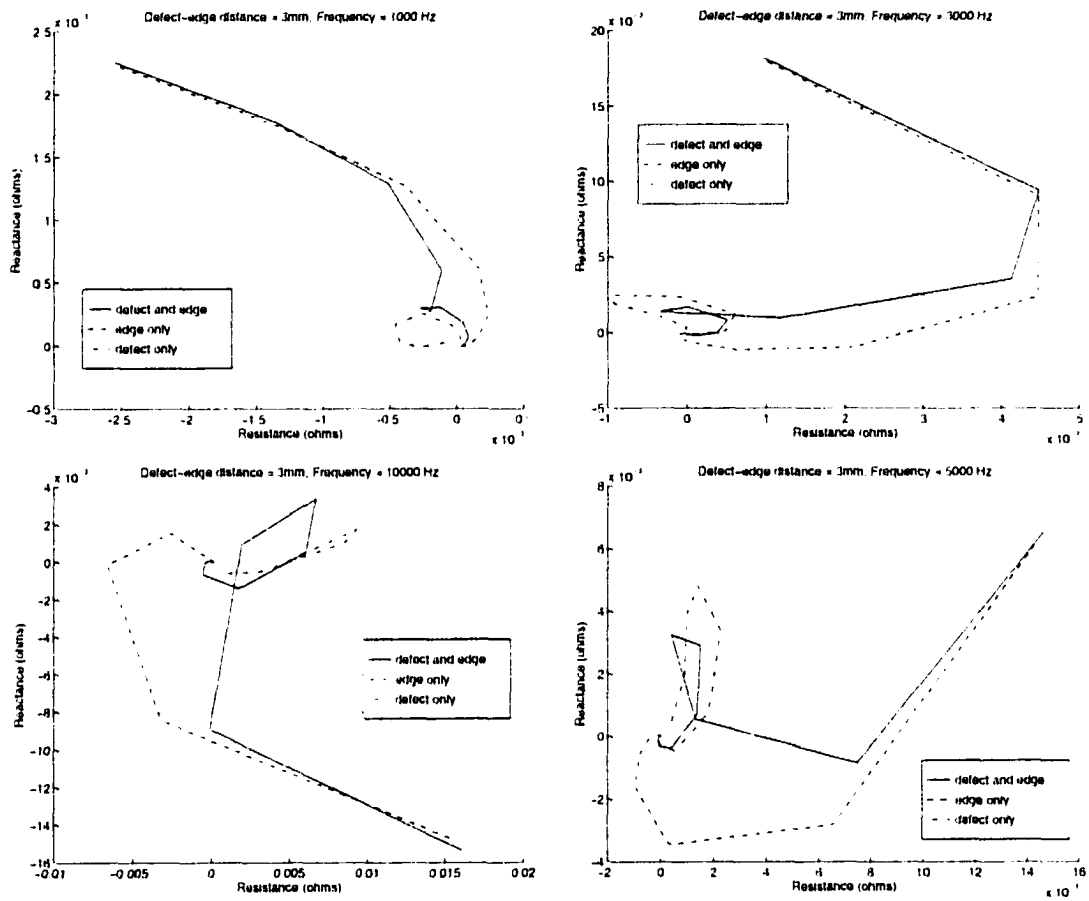


Figure 4.25 Impedance plots for the new probe (model) with a edge-defect distance of 3mm with changing frequency  $f$ . (a)  $f=1\text{KHz}$ . (b)  $f=3\text{KHz}$ . (c)  $f=5\text{Hz}$  and (d)  $f=10\text{KHz}$ .

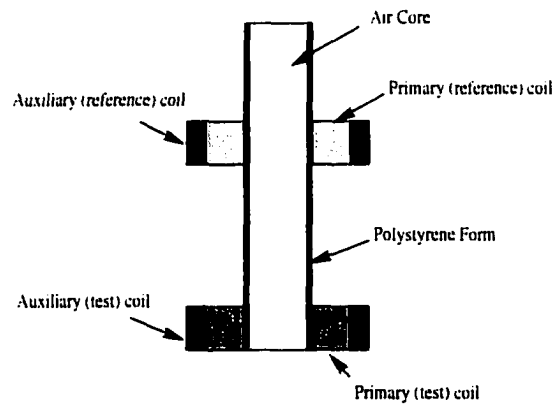
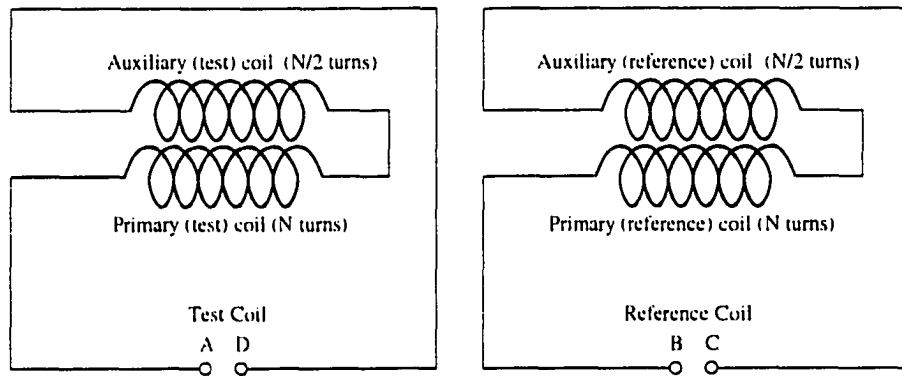
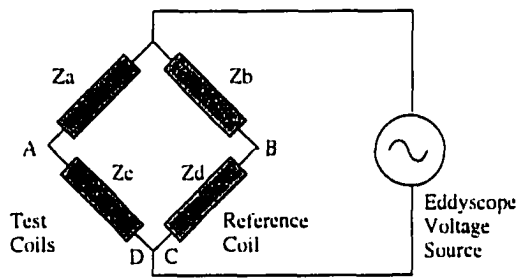


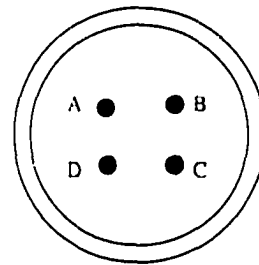
Figure 4.26 Schematic of the experimental probe (crosssectional view).



(a) Coil Connections



(b) Bridge Circuit



(c) Connector Pins

Figure 4.27 Probe coil connections and circuit.

In the differential mode of operation the impedance of the reference coil (between B and C) should be as close as possible to the impedance of the test coils (between A and D). Equal impedance of the primary and auxiliary coils ensures equal currents in both the coils, as required in the design. The half number of turns ( $N/2$ ) in the lower auxiliary coil is required so that the auxiliary coil has half the cross-section area of the primary coil. The winding direction in the auxiliary coil is chosen so that the flux of the lower auxiliary coil  $L2$  opposes the flux of the primary coil. This is essential for achieving the flux focusing effect.

In order to generate flaw signals a sample of 2 mm thick aluminum sheet was used with circular flaws of 2 mm diameter machined at distances of 5 mm and 7 mm from the edge (Figure 4.28). The defects in the numerical model was cubic in shape in contrast to the cylindrical defect shape used in the experimental sample, but the size of the flaws were comparable. These defects in the sample are surface breaking flaws that go all the way through the sample (2 mm thick).

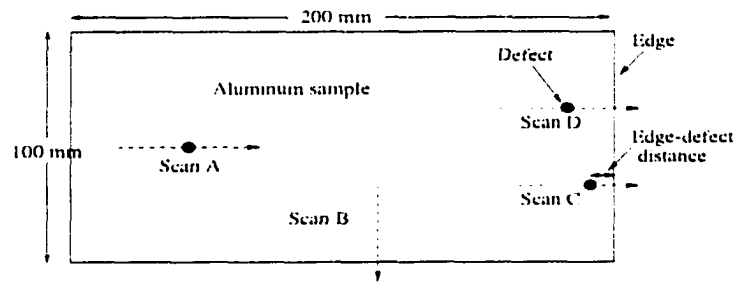


Figure 4.28 Test sample with flaws. Probe scan directions are shown by the arrows.

A personal computer based eddyscope designed at Iowa State University was used to measure the experimental signals. Direct control over the current in the coils and the data handling (capture, storage and transfer) capability were special features of the eddyscope that were used to conduct the experiment. Figure 4.28 shows the direction of the probe scan over the sample. Scans A and B produce the defect only and edge only signals respectively. Scans C and D generate signals from a defect at a distance of 5 mm and 7 mm from the edge respectively.

Figures 4.29 and 4.30 show the flaw signals as obtained from the probe built according to the specifications obtained from the numerical model. These results from the actual probe are compared with signals obtained using the the model. Figure 4.29 presents the experimental signals using a conventional eddy-current probe which can be compared with numerical predictions presented in Figures 4.23. Figures 4.24 and 4.30 are the numerical and the experimental results for the proposed

probe respectively at two different edge to defect distances and operating frequency of 10 KHz. The experimental results are normalized plots and hence a direct comparison of the magnitude cannot be made with the model predictions.

The experimental results are in qualitative agreement with the results obtained from the numerical model except for a phase rotation. These results validate the numerical model used in the design of the probe. The measured signals also confirm the feasibility of the flux shaping approach for minimizing edge effect and detecting flaws in the proximity of edges.

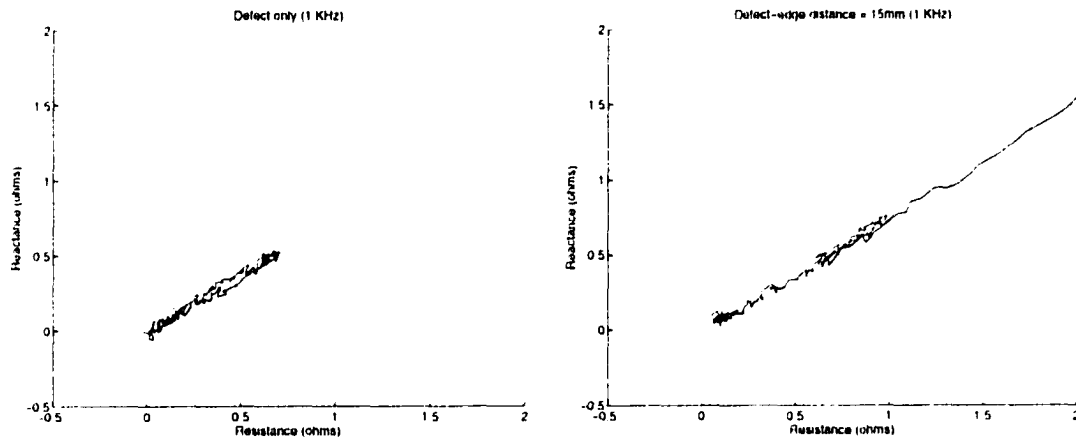


Figure 4.29 Impedance plane plots for the conventional probe (experimental):  
(a) defect signal (b) defect and edge composite signal.

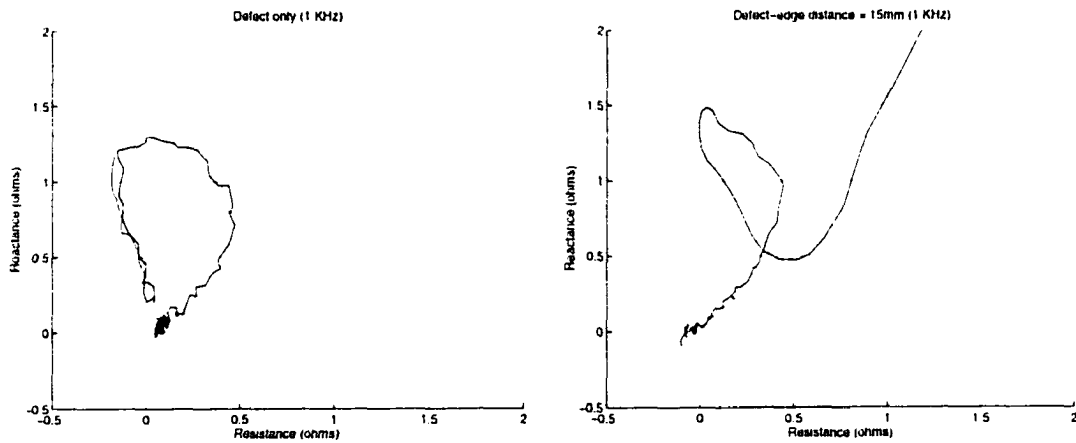


Figure 4.30 Impedance plane plots for the new probe (experimental)

## 5 REMOTE FIELD EDDY CURRENT

A major challenge in aircraft inspection is the detection of subsurface cracks around fastener holes also referred to as the problem of crack under fasteners (CUFs). CUF detection has proved to be difficult using the conventional eddy current (EC) methods that are limited to the inspection of surface and near surface anomalies. The remote field eddy current (RFEC) technique [13], initially introduced in the inspection of tubular metallic samples, is characterized by equal sensitivity to a flaw irrespective of its location in the tube wall. This method has been extended for inspecting defects in thick metal plates. This chapter investigates the feasibility of using RFEC technique for detecting CUFs. Simulation of the RFEC inspection using the finite element method requires large computing resources caused primarily due to the large distance between the driver and pickup coils. A three dimensional numerical model using a volume partition approach is described for reducing the computational resource requirement in the simulation of RFEC signals.

### Introduction

The detection of flaws that are located deep inside thick walled metallic plates is of interest to both aircraft and petrochemical industries. Aluminum aircraft fuselage skins can develop small fatigue cracks after an extended period of service due to the numerous pressurization cycles [25]. Usually, the outer skin is countersunk to provide for assembly with flush-head fasteners. The sharp edge in the skin, caused by the countersink, provides a high stress concentration for fatigue crack generation as shown in Figure 5.1. Numerous small cracks may be generated along a particular row of fasteners. The small cracks continue to grow with time and at some point they can cause failure of the skin and rapid decompression of the aircraft cabin can result. Hence there is a crucial need to detect them in their incipient stage.

Conventional eddy current methods have had limited success in the detection of CUFs [25]. The RFEC technique overcomes this difficulty and has shown considerable promise in detecting flaws in thick aluminum plate structures [15]. The RFEC method was initially used for flaw detection in the

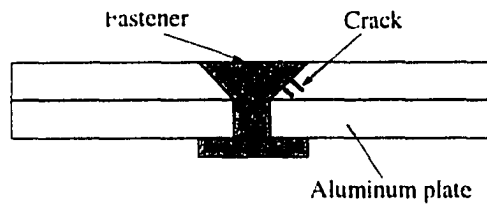


Figure 5.1 Fatigue cracks under fastener.

walls of tubular products.

The principles of RFEC inspection technique is discussed for the case of tubular geometry. Consider a pair of coils inside a tube of conducting material with their axis along the axis of the tube as shown in Figure 5.2. One of the coils (driver) is excited with a sinusoidal current and the other (pickup) used to sense the field. If the distance between the coils is varied by moving the pickup coil along the axis of the tube three distinct zones can be observed as indicated in Figure 5.2. The amplitude of the  $\vec{B}$  field decreases very rapidly in the region between the coil to a distance of approximately  $1D$  or one times the diameter of the coil. The field amplitude goes through a point of inflection between the distances of  $1D$  and  $2D$  followed by a region of slow decrease in the region beyond a distance of  $3D$  from the excitor coil.

The energy flow in the RFEC probe inspection method is indicated in Figure 5.2. In the near field region there is direct coupling of energy from the driver to the pickup [13] where as there is no direct coupling of energy in the remote field zone. The transition region lies approximately two diameters away from the driver coil. In terms of energy flow the energy sensed by the pickup coil has travelled through the tube wall twice radially [16] in the remote field region. The phase lag in the pickup coil is therefore proportional to the wall thickness.

This phenomenon is successfully used in the RFEC inspection of tubular products and is being extended to inspect planar products such as aluminum plates. In RFEC inspection the pickup coil is typically two to three diameters away from the excitor coil. This chapter describes the development of a 3D finite element model for simulating this phenomenon.

The experimental results [14] have validated the above approach. Figure 5.3 shows the RFEC signal obtained experimentally from the inspection of an aluminum plate with a defect of depth=50% of the plate thickness. To successfully model the flaw detection signal a three dimensional (3D) finite element model is required which can be used to optimize the design of the RFEC probe. The large distances involved between the driver and pickup coils translate into a large number of elements

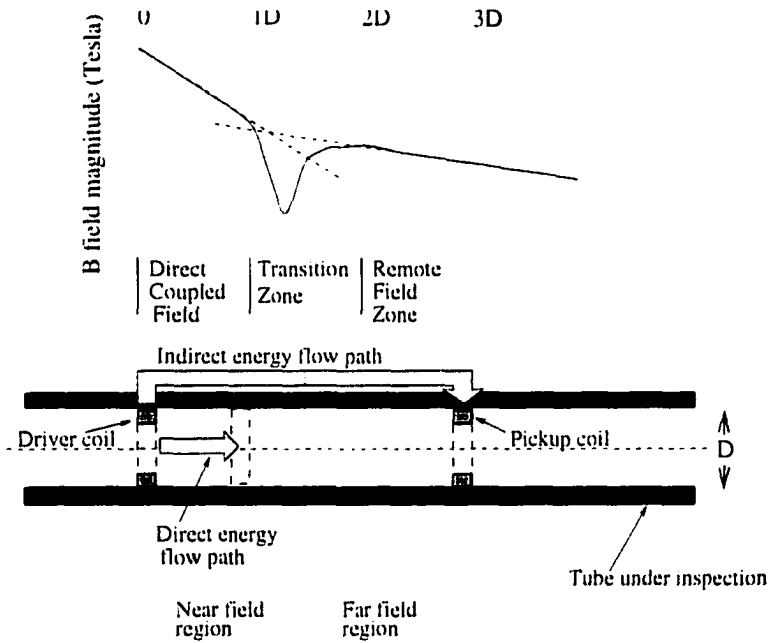


Figure 5.2 RFEC probe in a tube showing the profiles of the B field just inside the pipe wall. Direct field region, transition and the remote field zones are indicated in the graph.

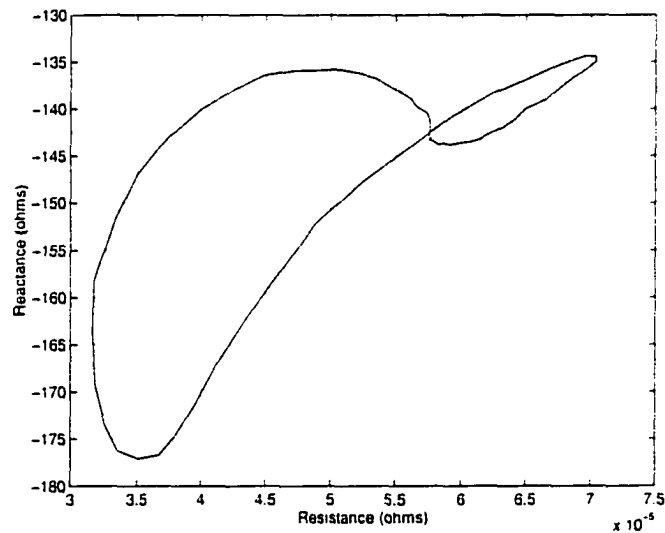


Figure 5.3 Experimental RFEC signal at 400Hz for a 50% defect in an aluminum plate.

needed for discretizing the volume. The finite element model consequently requires large amounts of computer resource in terms of both the computer memory and processing time.

This chapter presents a numerical method for reducing the computational resource requirement. The underlying idea of the approach is based on partitioning the overall volume into two sub-volumes and solving the problems sequentially in the sub-volumes. The results obtained in one volume is used as the forcing function for the second.

Figure 5.4 presents the schematic of the RFEC probe and test geometry. The probe consists of an excitation coil and a pickup coil, both wound inside a ferrite core with a metallic shield encircling the coil. This arrangement prevents the flux from the excitation from directly linking with the pickup coil, which is placed in the far field region of the excitation coil and picks up the RFEC signal.

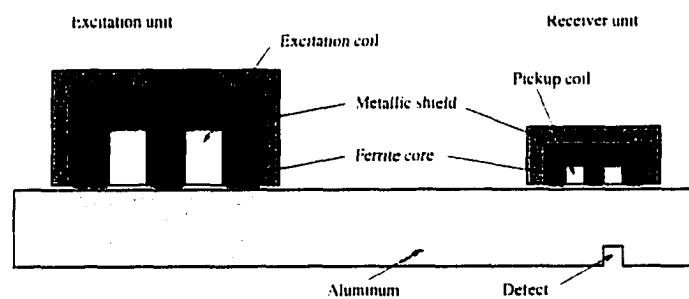


Figure 5.4 Schematic of the probe for thick aluminum plate inspection.

The numerical computation of the RFEC signal in the pickup coil requires the use of a 3D finite element model. It can be observed that the size of the pickup coil is very small relative to that of the excitation coil and it is located in the far field region of the excitation coil. With a plate thickness of 25mm and the excitation-pickup coil distance of 200mm, the FE mesh required for modeling the geometry will have a large number of elements. Moreover there are two coils involved each with its own axis of symmetry requiring a 3D FE model. If the driver and pickup coils are modeled using two different volumes, and the computer resource requirement can be reduced and useful numerical results obtained.

This approach for reducing the total number of elements can be used more effectively if the geometry being modeled is static. Simulations of eddy current inspection signals require a relative motion between the probe and the defect in the test sample resulting in a geometry that is dynamic. With some approximations as shown in the next section, the volume partition method can be used for generating the eddy current signals in the RFEC inspection method.

## Volume Partition Method

The volume to be modeled in the finite element modeling of an eddy current probe may be partitioned into sub-volumes. The volume partitioning method is particularly useful in modeling the RFEC inspection where there are two coils, placed several diameters away from each other.

The approach is based on the assumption that the change in the field strength in the far field area of the coil will not have any effect on the vector potential values due to the change in the defect location, at the plane of partition located suitably far away. With this approximation the volume partition method can be used in modeling the RFEC method as two independent smaller sub-problems.

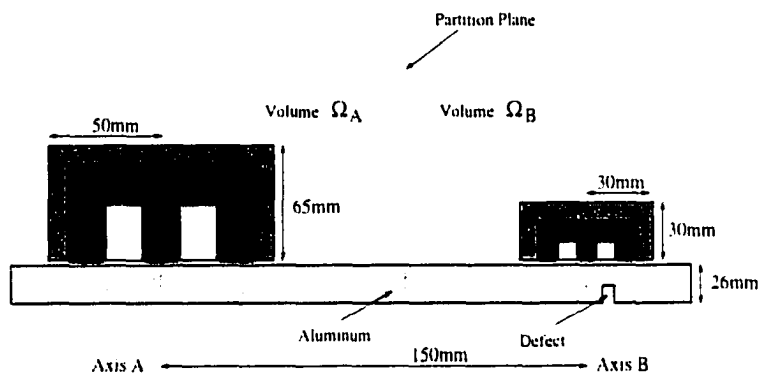


Figure 5.5 Partitioning of the volume to be modeled.

This approach divides a large volume into smaller volumes ( $\Omega_A$  and  $\Omega_B$ ) and the computer resource requirement, in terms of computer memory and processing time, can then be controlled to within the desirable limits. The volume  $\Omega_A$  contains the driver coil and the volume  $\Omega_B$  contains the pickup coil.

The volume partition approach for a three dimensional finite element model is demonstrated using a simple case of a circular current carrying ring. Figure 5.5 shows the partitioning of the volume of interest. Volume  $\Omega_A$  with the excitation coil is modeled first and the magnetic vector potential  $\vec{A}$  is computed on  $\Gamma$  the plane of partition.  $\Gamma$  is then used as one of the boundary planes to model the volume  $\Omega_B$  with the pickup coil and the previously computed vector potential  $\vec{A}$  values on  $\Gamma$  are used as the boundary conditions.

Figure 5.6 indicates the use of half symmetry with the plane  $y = 0$  being the plane of symmetry.

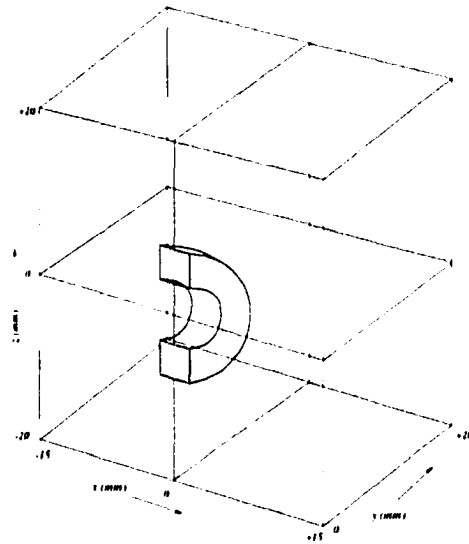


Figure 5.6 The volume with the current carrying coil modeled using a 3D finite element method.

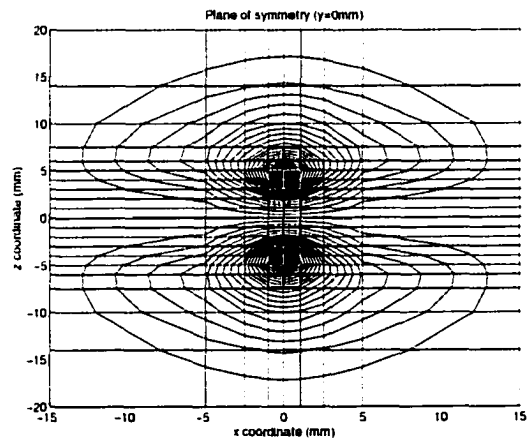


Figure 5.7 Coil flux in the plane of symmetry for the full volume.

The computed numerical solution of vector potential  $\vec{A}$  at the nodes of this mesh is plotted as contours to obtain the flux associated with the coil as shown in Figure 5.7.

From this solution we can obtain the vector potential  $\vec{A}$  values on plane  $z = 5\text{mm}$ . These values are used as the boundary values in the reduced model of the volume  $\Omega_B$  (Figure 5.8), with the plane  $z = 5\text{mm}$  being the partition plane.

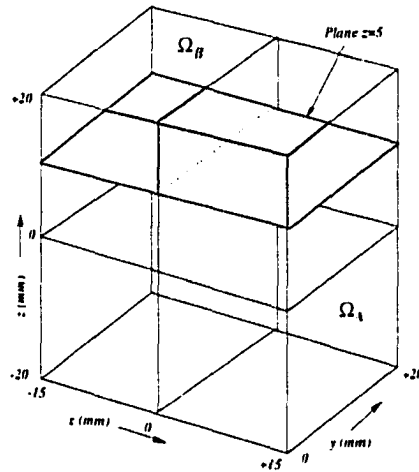


Figure 5.8 Partition plane location.

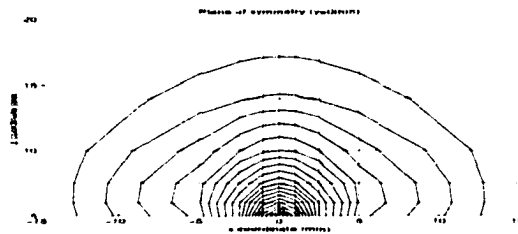


Figure 5.9 Flux plot in the plane of symmetry for the reduced volume ( $\Omega_B$ ).

The finite element solution of the coil field in volume  $\Omega_B$ , using the boundary conditions previously obtained, is shown in Figure 5.9. The result in Figure 5.9 demonstrates the successful implementation of partitioning the overall volume to the reduced volumes, which are modeled independently.

The total memory requirement and processing times for both the volumes  $\Omega_A$  and  $\Omega_B$  is less than the requirement for the entire volume  $\Omega$ . This advantage is greatly magnified in the simulation of the RFEC method as the pickup coil is placed remotely from the driver coil. The results of

implementing this method to obtain RFEC signals are discussed in the next section.

Figure 5.5 shows the RFEC geometry and location of the plane  $\Gamma$  used to partition the volume  $\Omega$  into  $\Omega_A$  and  $\Omega_B$ . The total volume if partitioned appropriately can lead to subvolumes in which additional symmetries emerge. In Figure 5.5 only the volume  $\Omega_B$  contains the defect and hence the defect free region  $\Omega_A$  with the driver coil can be modeled using a quarter symmetry. The pickup coil region  $\Omega_B$  with the defect will have to be modeled using at least half symmetry. The use of quarter symmetry in  $\Omega_A$  leads to substantial savings in terms of computing resource requirement.

From Figure 5.5 we see that volume  $\Omega_A$  has an axis of symmetry which can be further used to reduce the computation resource required. Table 5.1 shows the quantitative reduction in the number of elements in the finite element model and the memory requirement for the banded half stiffness matrix.

Table 5.1 Resource requirement for modeling

Parameter	Full volume ( $\Omega$ ) model	Partitioned volume ( $\Omega_A + \Omega_B$ ) model
Total elements	11872	3136+5600
Memory requirement	300 MB	75+130 MB
Computation time (single run)	12 hours	5 hours
Computation time (total)	180 hours	77 hours

Figure 5.10 shows the simulated signal from the pickup coil using a frequency of 400Hz. Eddy current signals are plotted on a complex plane with the resistance  $R$  (real) on the x-axis and reactance  $X_L$  (imaginary) on the y-axis. The simulation signals obtained are in good qualitative agreement with the experimental results [15] in Figure 5.10.

To successfully model the flaw detection signal in RFEC inspection of planar samples, a three dimensional (3D) finite element model is required which can be used to optimize the design of the RFEC probe. This is a computationally very intensive problem that requires large amounts of computer memory and processing time. A volume partitioning approach has been presented for handling such problems involving a large 3D FE mesh. The approach has been validated by comparison of the model predictions with experimental measurements.

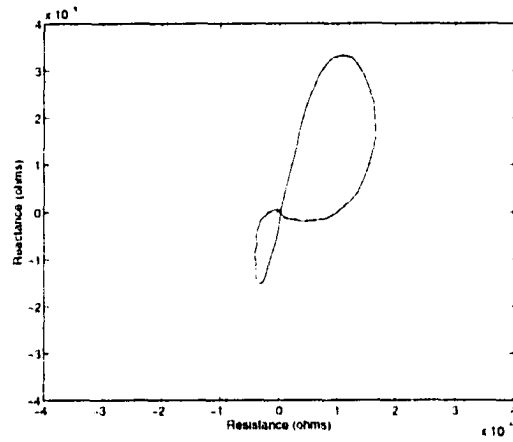


Figure 5.10 The experimental RFEC defect signal at 400 Hz.

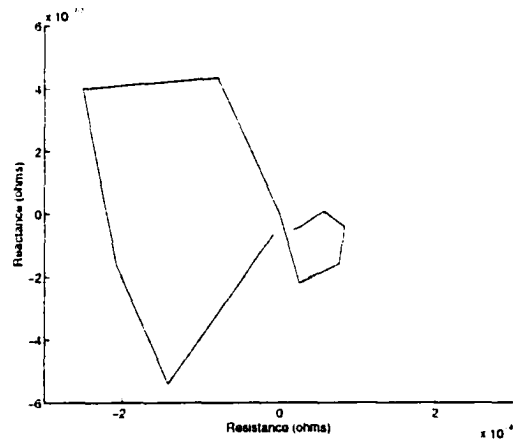


Figure 5.11 The simulation RFEC defect signal at 400 Hz (moving pickup coil).

The volume partition method divides a large volume mesh in a finite element model into sub-volumes. The sub-volumes are then modeled and solved for separately with communication of the boundary values between the two volumes. A smart partition of the volume and bring out additional symmetries in the sub-volumes and can further reduce the memory and processing time requirements. This method has been especially demonstrated to be useful in the planar inspection of the samples using the RFEC technique. The driver coil and the pickup coils are modeled in separate sub-volumes. The volume with the driver coil has no defects in it and there a quarter symmetry can be applied. This method is being used to model the inspection of cracks under fasteners (C'UFs) in multilayer aircraft frame samples.

## 6 MAGNETO-OPTIC IMAGING

Detection of corrosion in multilayer structures is a problem of significant importance in aircraft frame inspection. Low frequency eddy current (LFEC) inspection methods have been used for detection of corrosion that builds up between the layers of aluminum structures in the aircraft frame with limited success [25]. Use of low frequency excitation leads to the probes having large footprints and hence severe edge effect. The probes also have low resolution and are unable to detect small flaws or corrosion.

The magneto-optic/eddy current imaging (MOI) technique has shown considerable promise in detection of subsurface cracks and corrosion in aircraft skin inspection [24],[20]. The operating principle of the magneto-optic imaging is based on first inducing eddy currents in the conducting test sample and then image the magnetic field associated with these eddy currents using a magneto-optic sensor.

### Introduction

The increasing interest in the optical-based sensing systems is in part due to the fact that they can directly produce images for interpretation. They are also well suited for use with the fiber-optic systems and can operate in environments where electrically based sensors are difficult to use. The physics of magneto-optic effects and their application in the design of NDE systems is discussed in this section.

The interaction of light with material is affected by the magnetic and electric state of the material and give rise to the magneto- and electro-optic effects. These interactions may be characterized by the *constitutive relations*.

$$\vec{D} = \epsilon \vec{E} \quad (6.1)$$

$$\vec{B} = \mu \vec{H} \quad (6.2)$$

where  $\epsilon = \epsilon_0$  and  $\mu = \mu_0$  is the permittivity and the permeability of free space. If the  $\epsilon$  and/or  $\mu$

---

of a medium is dependent on the direction, then the medium is said to be *anisotropic* and they are represented by a tensor (matrix). For an anisotropic medium the constitutive relations are given as,

$$\vec{D} = \epsilon \cdot \vec{E} \quad (6.3)$$

$$\vec{B} = \mu \cdot \vec{H} \quad (6.4)$$

For a suitable choice of the coordinate axes these symmetric tensors may be expressed as a diagonal tensor (principal system) with only three independent constants (material assumed to be homogenous) and the permeability tensor may be expressed as,

$$\hat{\mu} = \begin{bmatrix} \mu_x & 0 & 0 \\ 0 & \mu_y & 0 \\ 0 & 0 & \mu_z \end{bmatrix}$$

In general when the medium is *biaxial*  $\mu_x \neq \mu_y \neq \mu_z$ . If for a medium  $\mu_x \neq \mu_y = \mu_z$  then it is said to be *uniaxial*.

Many materials which are normally isotropic become anisotropic when subject to an externally applied electric, magnetic fields or mechanical stress. Such induced anisotropy is of special interest in non-destructive evaluation (NDE). The magnetic field that induces the anisotropy can be measured by observing the magneto-optic effects.

As a special case of induced anisotropy the medium may become *gyrotropic*, in which case the tensor  $\hat{\mu}$  is hermitian. In an anisotropic material differently polarized waves propagate with different velocities (*birefringence*) and/or with different attenuation (*dichroism*). The phenomenon of birefringence and dichroism exhibited in transmission and reflection of light in anisotropic material are known as *Faraday* and *Kerr* magneto-optic effects respectively. The Faraday effect is one of the most well studied magneto-optic effects, and is the underlying idea in the magneto-optic imaging (MOI) NDE method.

In the presence of a large magnetic field the constitutive relations for an isotropic media are,

$$\vec{D} = \epsilon_0 \vec{E} \quad (6.5)$$

$$\vec{B} = \mu_0(\vec{H} + \vec{M}) = \hat{\mu} \cdot \vec{H} \quad (6.6)$$

where  $\hat{\mu}$  is the complex permeability tensor for the medium and  $\vec{M}$  is the magnetization in presence

of the external field  $\vec{H}$ . It can be shown that the complex permeability tensor  $\hat{\mu}$  is of the form,

$$\hat{\mu} = \begin{bmatrix} \mu_{11} & \mu_{12} & 0 \\ \mu_{21} & \mu_{22} & 0 \\ 0 & 0 & \mu_{33} \end{bmatrix} \quad (6.7)$$

where  $\mu_{12} = \mu_{21}$  (complex conjugate). For a uniaxial and lossless media this tensor will take the form,

$$\hat{\mu} = \begin{bmatrix} \mu & j\mu_g & 0 \\ -j\mu_g & \mu & 0 \\ 0 & 0 & \mu_z \end{bmatrix} \quad (6.8)$$

and a hermitian tensor of this form is known as gyrotropic. This tensor can also be expressed by a numerical approximation using complex variables [23] as,

$$\hat{\mu} = \mu_0 n^2 \begin{bmatrix} 1 + FQ^2 & jQ & 0 \\ -jQ & 1 + FQ^2 & 0 \\ 0 & 0 & 1 \end{bmatrix} \quad (6.9)$$

where the complex constants  $n$ ,  $Q$  and  $F$  of the material are the refractive index (of demagnetized isotropic material), primary and secondary magneto-optical constants respectively. The Faraday and Kerr effects can be explained by the primary constant  $Q$  ( $F=0$ ). The secondary magneto-optical effects such as the Voigt effect are explained in terms of the second constant  $F$ .

Consider an electromagnetic wave in  $+z$  direction in free space (charge density  $\rho = 0$ ) governed by Maxwell's equations.

$$\nabla \times \vec{E} = -j\omega \vec{B} \quad (\text{Faraday's law}) \quad (6.10)$$

$$\nabla \times \vec{H} = j\omega \vec{D} + \vec{J} \quad (\text{Ampere's law}) \quad (6.11)$$

$$\nabla \cdot \vec{D} = \rho \quad (\text{Gauss's law}) \quad (6.12)$$

$$\nabla \cdot \vec{B} = 0 \quad (\text{Gauss's law}) \quad (6.13)$$

where,  $\vec{E}$  is the electric field strength,  $\vec{B}$  is the magnetic flux density,  $\vec{H}$  is the magnetic field strength,  $\vec{D}$  is the electric displacement,  $\vec{J}$  is the electric current density, and  $\rho$  is the electric charge density.

The electric and magnetic fields in this case has only  $x$  and  $y$  components in order to satisfy Gauss' law. The  $\vec{E}$  and  $\vec{H}$  fields can be expressed in,

$$\vec{E} = (xE_x + yE_y)e^{-jkz} \quad (6.14)$$

$$\vec{H} = (xH_x + yH_y)e^{-jkz} \quad (6.15)$$

The  $\vec{E}$  and  $\vec{H}$  fields must also satisfy equations  $\nabla \times \vec{E} = -\frac{\partial \vec{H}}{\partial t}$  and  $\nabla \times \vec{H} = \vec{J} + \frac{\partial \vec{D}}{\partial t}$ . Equating each component we have,  $E_x = vB_y$  &  $E_y = -vB_x$ , and,  $H_x = -vD_y$  &  $H_y = vD_x$  where  $v = \omega/k$  with  $\omega$  being the angular frequency and  $k = \frac{1}{\sqrt{\epsilon\mu}}$ .

Applying these with equations (6.1) and (6.2) we get.

$$\frac{H_y}{H_x} = \frac{-jv^2\mu_g\epsilon_0}{1-v^2\mu\epsilon} = \pm j \quad (6.16)$$

$$v = \frac{\omega}{k} = \sqrt{\frac{1}{\epsilon_0(\mu \pm \mu_g)}} \quad (6.17)$$

There are thus two possible waves in the medium as shown by the equations above. The wave vectors for the left and right circularly polarized waves for such a medium are calculated using above equation to be.

$$k_L = \omega \sqrt{[\epsilon_0(\mu + \mu_g)]} \quad (6.18)$$

$$k_R = \omega \sqrt{[\epsilon_0(\mu - \mu_g)]} \quad (6.19)$$

Let  $+z$  be the direction of propagation of a linearly polarized light in this gyrotropic media. Suppose at  $z = 0$ .

$$\vec{H} = xH_0 = (x + jy)\frac{H_0}{2} + (x - jy)\frac{H_0}{2} \quad (6.20)$$

where the linearly polarized wave has been resolved into two orthogonal circular polarizations with  $H_0 = ||H_x|| = ||H_y||$ .

After the wave that has propagated a distance  $d$  units into the media, the magnetic field can be written as.

$$\vec{H} = (x + jy)\frac{H_0}{2}e^{-jk_L d} + (x - jy)\frac{H_0}{2}e^{-jk_R d} \quad (6.21)$$

where  $k_L$  and  $k_R$  are the wave vectors for the left and right circularly polarized waves. Rearranging this equation we get.

$$\vec{H} = \frac{H_0}{2}(e^{-jk_L d} + e^{-jk_R d})(x + yj \tan \theta) \quad (6.22)$$

where.

$$\theta = \frac{(k_L - k_R)d}{2} \quad (6.23)$$

which shows that the wave is still linearly polarized but the polarization axis has been rotated counterclockwise by an angle  $\theta$ . The rotation of a linearly polarized light in the presence of a magnetic field in the direction of propagation of light is called the *faraday rotation*.

This angle of rotation  $\theta$  (*specific rotation*) is proportional to  $\bar{\mu}$  ( $k = \sqrt{\omega[\epsilon_0(\mu \pm \mu_g)]}$ ), which is proportional to the magnetization  $M$ . It can hence be derived that,

$$\theta = K M d \quad (6.24)$$

where  $K$  is known as Kundt's constant.

If the off diagonal terms in equation (6.7) did have real parts the media would be lossy. A linearly polarized light on propagating through the media will then become elliptically polarized.

### Magneto-optic/Eddy current Imaging

In this NDE technique eddy currents are induced in the material to be inspected and a magneto-optic sensor images the resulting magnetic field. Material irregularities will cause disturbances in the magnetic field which translates to the visual indications in the image.

The magneto-optic sensor used is a thin ferrimagnetic bismuth doped iron garnet film (0.5 mm). These films exhibit the property of magnetic anisotropy and have an easy axis of magnetization normal to the surface. The material is transparent to light and is characterized by a large value of specific Faraday rotation (rotation per unit of thickness) in the range of 20,000 to 40,000 degrees/cm of film thickness. This feature is particularly useful in detecting low level magnetic fields which is desirable in NDE applications.

Uniform sheet currents (300 A) at a low frequency (1-50kHz) are produced in a copper sheet (8.5 cm wide) which is used to induce eddy currents in the surface being inspected. The magnetic fields associated with the sheet [24] currents (in both the foil and the test piece) lie parallel to the hard axis of magnetization of the sensor. These fields have little or no effect on the state of magnetization of the sensor.

The presence of defects in the surface makes the otherwise uniform eddy currents non-uniform. These non-uniform currents will produce a magnetic field normal to the surface of the sample. The iron-garnet film is placed such that these fields pass through its cross section (along the easy axis of magnetization). A beam of linearly polarized light is made incident on this garnet film and the reflected light is collected on a photo-film after passing through an analyzer. The non-uniform magnetic fields in the garnet film rotates the plane of polarization of the incident light. The analyzer blocks any light that has been rotated in polarization resulting in a dark image of defects on the photo-film.

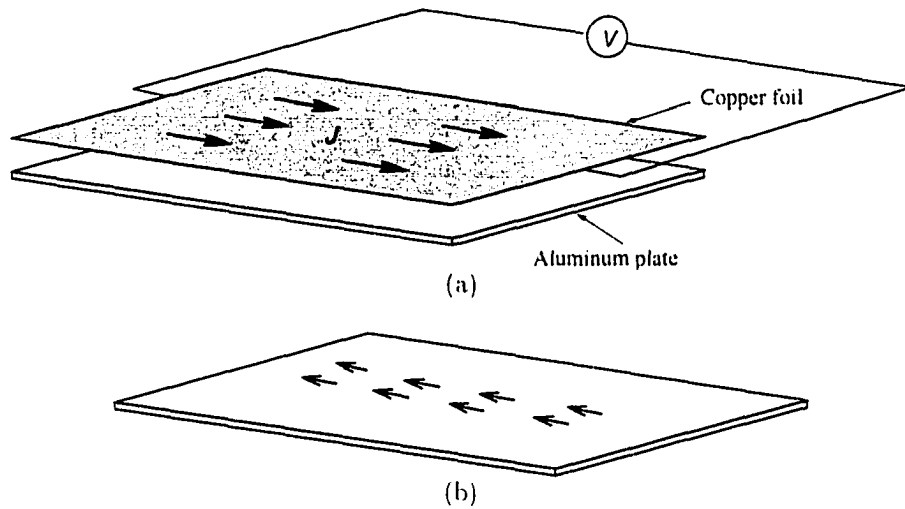


Figure 6.1 (a) Schematic of the magneto-optic/eddy-current imaging device.  
 (b) Induced eddy currents in a plate of conducting material.

The MOI instrumentation for NDE applications has been developed at PRI Instrumentation, Inc. of Torrance, California. Figure 6.1(a) shows the schematic of the MOI device. The copper foil carrying a time varying (sinusoidal) planar currents is used to induce eddy currents in the sample as shown in Figure 6.1(b). The presence of defects such as a hole in the sample disturbs the induced eddy currents as shown in Figure 6.2(a) and the magnetic fields associated with these currents in the sample are shown in Figure 6.2(b).

With the sample plate in the  $x$ - $y$  plane the  $z$  component of the magnetic field  $\vec{B}$  is mapped using a sensor plate above the copper foil. The sensor consists of a single crystal garnet wafer (gadolinium gallium garnet) which serves as a substrate for a several micron thick epitaxial magnetic film. The magnetic film serves to amplify the magnetic field  $\vec{B}$ . As a plane polarized light passes through the film, its plane of polarization is rotated in proportion to the strength of the magnetic field (Faraday's Effect). With appropriate optics, the sensor transforms a spatially varying magnetic field into an optical image as shown in Figure 6.3.

The design of the MOI instrument is currently being enhanced to detect subsurface corrosion in multilayer aircraft structures. To study the sensitivity and improve the device a finite element model has been developed to compute the field values associated with MOI inspection. This chapter presents the results of numerical simulation studies.

A test sample consisting of an aluminum plate 2mm thick with a through hole of diameter 6.35

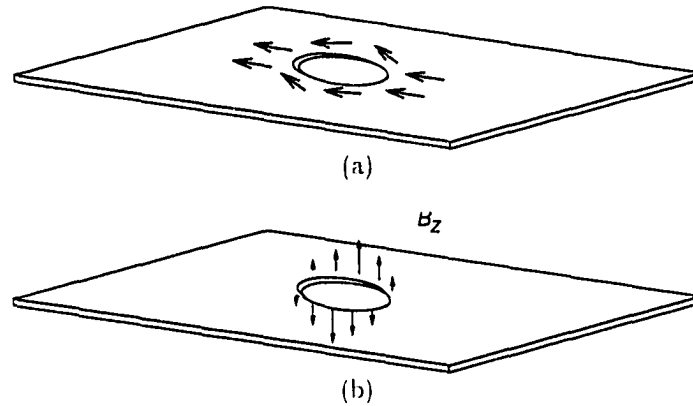


Figure 6.2 (a) The distribution of the eddy currents in the presence of a flaw such as a hole in the plate. (b) The magnetic field induced by the disturbed eddy currents.

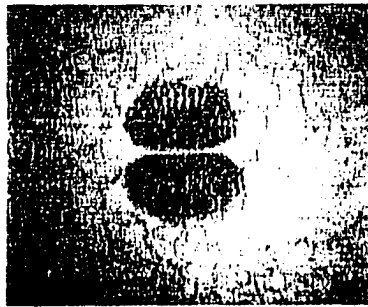


Figure 6.3 An experimental image obtained using the MOI inspection method.

mm along with a current source in the form of a current carrying foil (0.04 mm thick) at a distance of 0.35 mm from the sample is considered.

The above described geometry is modeled using the finite element (FE) method. The Maxwell's equation that describe the electromagnetic fields in terms of the magnetic vector potential ( $\vec{A}$ ) is given by,

$$\nabla \times \frac{1}{\mu} \nabla \times \vec{A} = -j\omega\sigma\vec{A} + \vec{J}_s \quad (6.25)$$

where  $\mu$  and  $\sigma$  are the permeability and conductivity of the medium respectively,  $\omega$  is the frequency of the exciting current in the copper foil and  $\vec{J}_s$  is the source current density.

The finite element method solves the above equation by minimizing the energy functional.

$$\mathcal{F} = \int_v \left[ \frac{1}{2\mu} |\nabla \times \vec{A}|^2 + \frac{1}{2} j\omega\sigma |\vec{A}|^2 - \frac{1}{2} \vec{J}_s \cdot \vec{A} \right] dv$$

The solution obtained in terms of  $\vec{A}$  values at each nodal point is used to compute the magnetic flux density  $\vec{B} = \nabla \times \vec{A}$ . In particular the normal component is given by  $B_z = \frac{\partial A_y}{\partial x} - \frac{\partial A_x}{\partial y}$ .

To reduce the computing resource requirement a quarter geometry is used as indicated in Figure 6.4. The current carrying foil and the aluminum sample with the hole both are assumed to be infinitely long in the direction of the current ( $y$ ). The normal  $z$  component of  $\vec{A}$  and the  $y$  component are forced to zero at the boundary planes normal to the direction of the current to satisfy the infinite length condition.

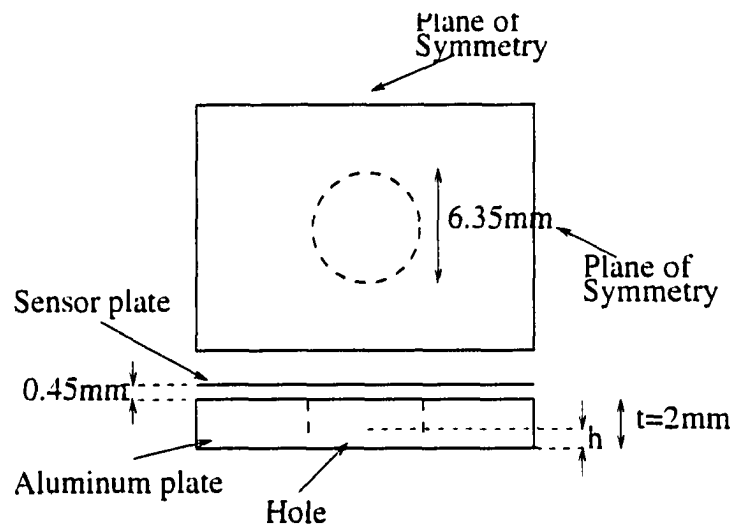
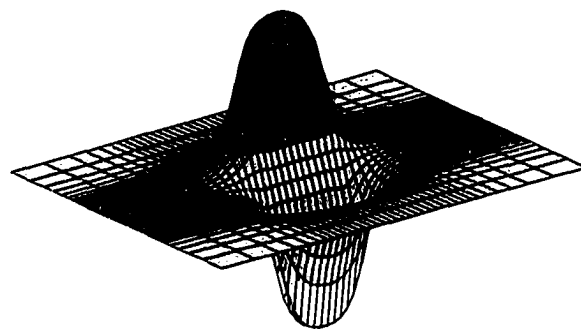
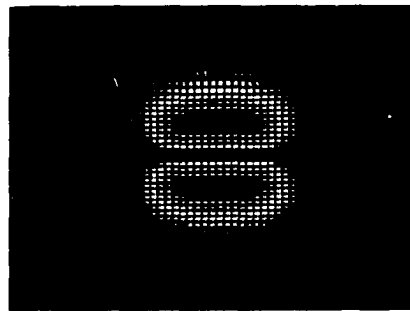


Figure 6.4 Geometry used for modeling a through hole in an aluminum plate.

Figure 6.5(a) shows the plot of  $B_z$  obtained numerically on the plane  $z = 0.5\text{mm}$ . The flux density is plotted as an image in Figure 6.5(b). The numerical model was validated using experimentally measured peak values of  $B_z$  at a frequency of 51.2KHz. The experimental field values are measured by gradually increasing the bias field around the sample which is an externally applied DC magnetic field to which the fields generated by the defect add. The net effect of increasing the bias field is to reduce the image size and when the peak field due to the hole and the DC field are equal the image vanishes completely. The reading of the DC field generator at this point is taken to be the peak defect field value. This model has further been used to model corrosion detection.



(a)



(b)

Figure 6.5 (a) The magnetic field ( $\vec{B}_z$ ) in the sensor computed using the finite element model for a through hole in the aluminum plate sample at 51.2kHz. (b) The projected image.

## Corrosion Detection

The MOI inspection method is being extended to detect corrosion in planar samples using the geometry in Figure 6.6. The test sample is an aluminum (7075) copper plate of thickness 1.5mm. A current inducing plate of thickness 0.04mm is placed above the aluminum sample plate at a distance of 0.35mm. The samples may consist of more than one plate, and corrosion may be present at plate interfaces. A corrosion pit in the form of a hemispherical dome of radius 19mm and height  $h$  is introduced in the plate as shown in the figure. Figure 6.7 shows the region of interest discretized using a finite element mesh.

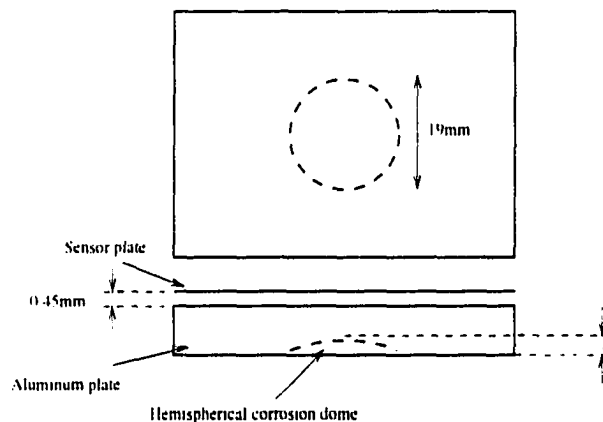


Figure 6.6 Geometry used for modeling corrosion detection.

Table 6.1 Numerical model parameters for MOI modeling.

Parameter	Value
Frequency	3 kHz
Source current density ( $J_s$ )	$10^8$ A/m
Copper foil conductivity ( $\sigma_f$ )	$5.8001 \times 10^7$ S/m
Aluminum conductivity ( $\sigma_{Al}$ )	$1.8867 \times 10^7$ S/m
Corrosion pit height ( $h$ )	0.3, 0.225, 0.15, 0.075mm

The parameter values used in the numerical model are summarized in Table 6.1. The normal component of the induced magnetic field ( $B_z$ ) is computed in the sensor substrate which is 0.5mm thick and directly above the current inducing foil.

Figure 6.8 shows the change in peak amplitude of the magnetic field  $\vec{B}_{z,max}$  with the change in the height  $h$  of the corrosion dome.

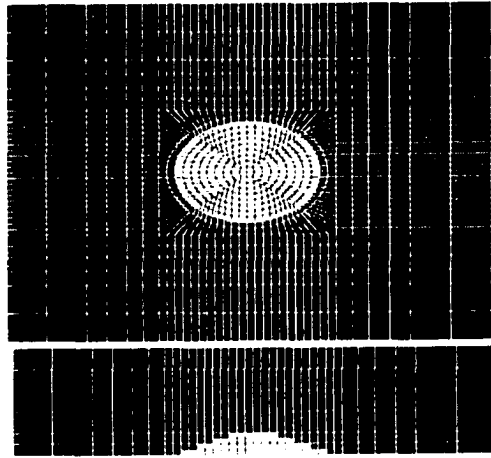


Figure 6.7 Discretization used in the finite element mesh as seen in the  $x$ - $y$  and  $x$ - $z$  plane.

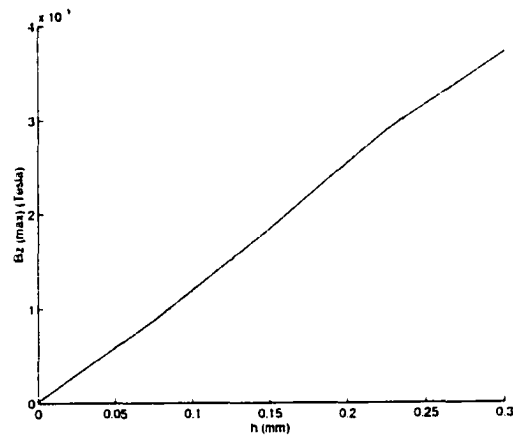


Figure 6.8 Change in the magnetic field  $|\vec{B}_z|_{max}$  (Tesla) with corrosion dome height  $h$  (mm).

### ***Foil Impedance Computation***

The copper foil used to induce currents in the sample can be treated as an eddy current probe and its effective impedance can be computed from the total energy and power. The finite element model was used to study the feasibility of using this measurement to characterize the defect. Assuming a current  $I$  ( $I_{rms} = I/\sqrt{2}$ ) through the coil, the total dissipated power ( $P$ ) and the energy stored ( $W$ ) in terms of the coil parameters are given as,

$$\begin{aligned} P &= \frac{1}{2} I^2 R \\ W &= \frac{1}{2} I^2 L \end{aligned}$$

From the above equations we compute impedance of the coil as

$$Z = R + j\omega L = \frac{P}{I^2} + j\omega \frac{2W}{I^2}$$

The total power dissipated and energy stored in the volume of interest is then computed as,

$$\begin{aligned} P &= \sum_{i=1}^n P_i = \sum_{i=1}^n \frac{\sigma_i}{2} \omega^2 |\vec{A}_i|^2 v_i \\ W &= \sum_{i=1}^n W_i = \sum_{i=1}^n \frac{1}{2\mu_i} |\nabla \times \vec{A}_i|^2 v_i \end{aligned} \quad (6.26)$$

where  $n$  is the total number of elements in the finite element mesh. Figure 6.8 shows the change in impedance of the current inducing foil with the change in the height  $h$  of the corrosion dome.

Figures 6.10(a), (b), (c) and (d) present the results obtained for corrosion domes of 5% (0.075mm), 10% (0.15mm), 15% (0.225mm) and 20% (0.3mm) metal loss respectively using a frequency of 3kHz. The peak value of the  $B_z$  correspondingly varies from 130 milligauss to 350 milligauss. In conclusion the MOI instrument can be modified to measure the foil impedance to provide additional information about the sample condition.

### ***Corrosion in a Two Layer Sample***

Industry is also interested in the effect of 2nd layer on signals due to corrosion. In order to study this effect the geometry shown in Figure 6.11 was modeled. Figure 6.11(a) and (b) shows the geometry used for modeling corrosion between two aluminum plates. Figure 6.11 presents the corresponding numerical results of change in  $\vec{B}_z|_{max}$  with increase in corrosion dome height  $h$ . The magnitude of values of  $|\vec{B}_z|_{max}$  are shown in the Table 6.2.

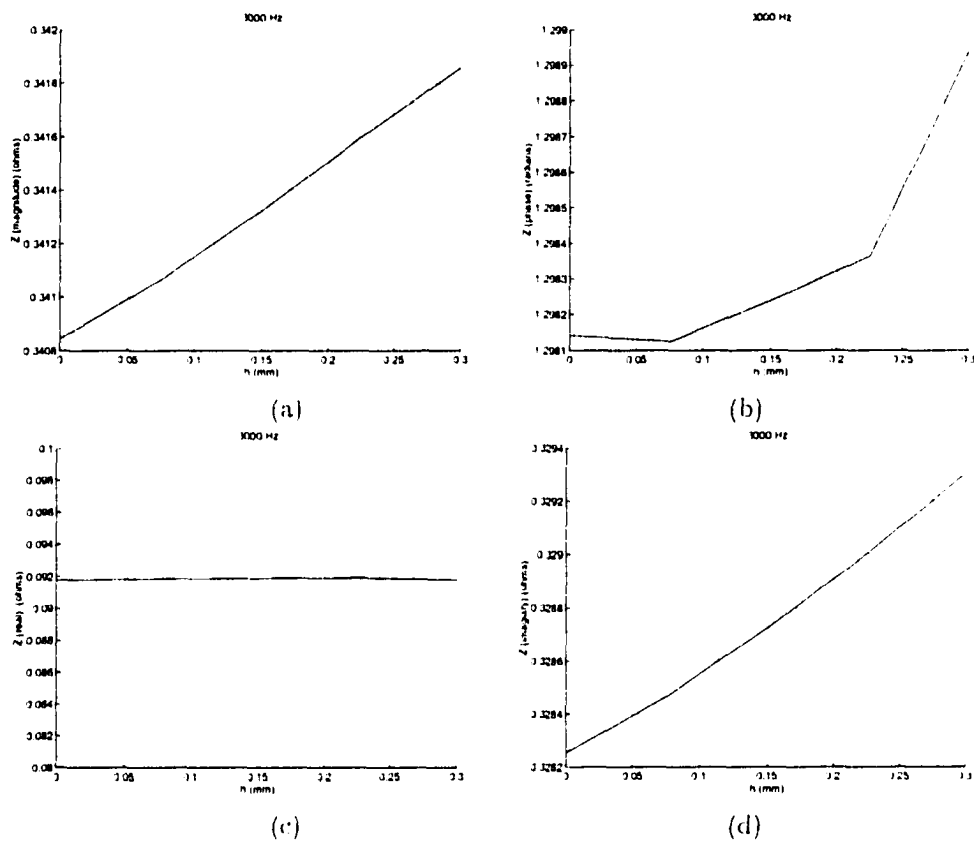


Figure 6.9 Impedance of the copper foil with changing corrosion dome height  $h$  with (a) the magnitude of  $Z$ . (b) the phase of  $Z$ . (c) the real part of  $Z$  (resistance) and (d) the imaginary part of  $Z$  (reactance) at a frequency of 3Khz.

Figure 6.12 shows the  $|\vec{B}_z|_{max}$  values as the corrosion dome height is increased. The effect of operating frequency on the defect parameters was modeled. Figure 6.13 shows the change in the  $|\vec{B}_z|_{max}$  in the sensor as the operating frequency is increased. The graph shows that the device cannot be very effective in detecting flaws below the frequency of 2.5Khz where the field values drop to very low levels. Experimentally it has been determined at PRI instruments Inc. that the MOI instrument gives good results when used at a frequency of around 3kHz.

These numerical studies should be successful in are providing information which can be used in calibrating the instrument and obtaining values of the currents and fields required for the optimal performance of the MOI device.

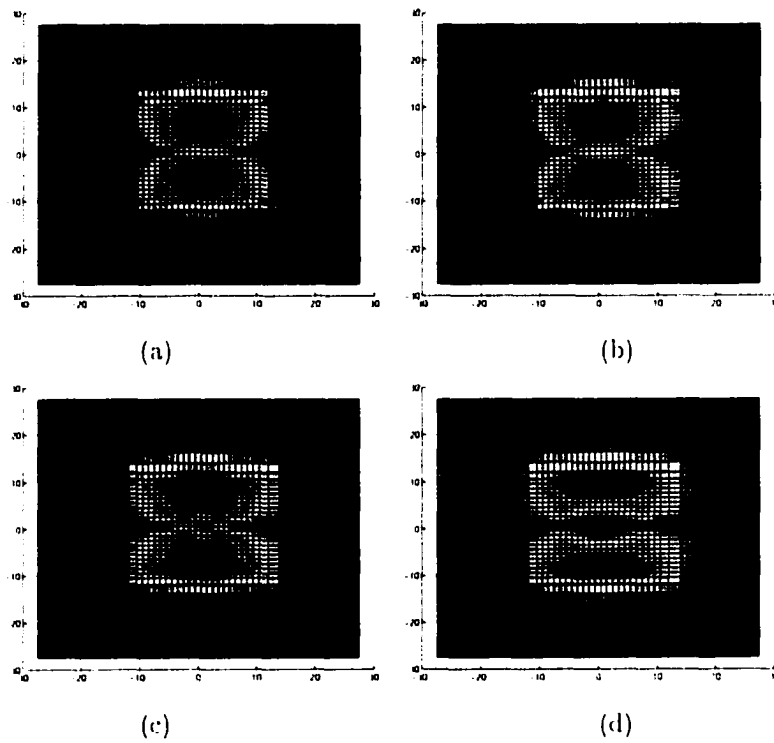


Figure 6.10 Computed MO images with varying corrosion dome height  $h$  (a)  $h = 0.075$  mm, (b)  $h = 0.15$  mm, (c)  $h = 0.225$  mm and (d)  $h = 0.3$  mm.

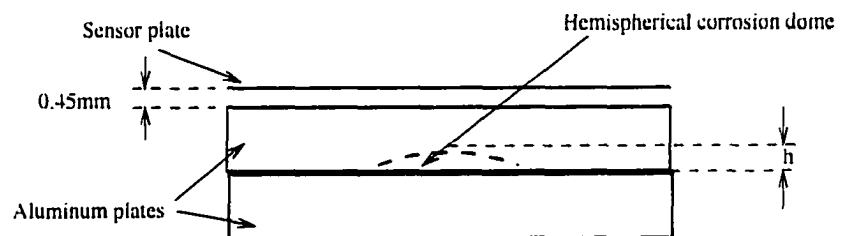


Figure 6.11 Geometry used for modeling corrosion detection between two aluminum plates.

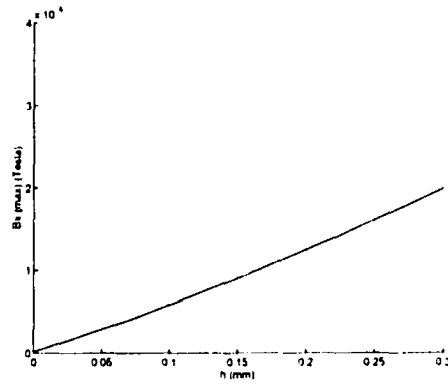


Figure 6.12 Change in  $|\vec{B}_z|_{max}$  for a two plate configuration with corrosion dome height  $h$ .

Table 6.2 Magnetic field with changing  $h$

Corrosion dome height (h)	$ \vec{B}_z _{max}$ (single Al plate)	$ \vec{B}_z _{max}$ (two Al plates)
0.000 mm	1.7441e-07 T	1.4360e-07 T
0.075 mm	8.8127e-06 T	4.2844e-06 T
0.150 mm	1.8482e-05 T	9.0425e-06 T
0.225 mm	2.8989e-05 T	1.4214e-05 T
0.300 mm	3.7273e-05 T	1.9924e-05 T

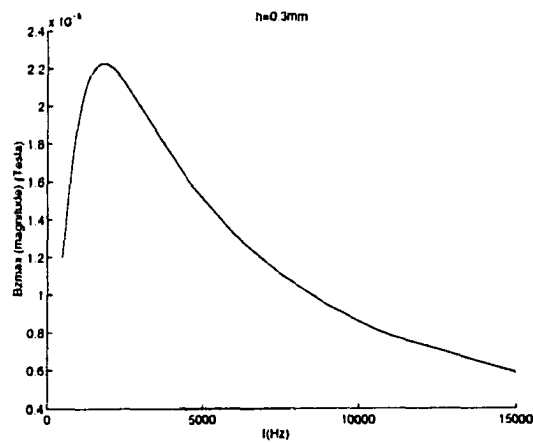


Figure 6.13 Change in the magnetic field  $|\vec{B}_z|_{max}$  (Tesla) with frequency (Hz) for a corrosion dome height  $h = 0.3\text{mm}$ .

## 7 CONCLUSION

A number of inspection problems of interest to the aviation industry have been addressed in this thesis. The focus of the work consists of both new probe design and analysis/optimization of existing technologies. The design and analysis of probes have been accomplished using finite element modeling of the eddy current phenomenon. A number of procedures for optimizing the three dimensional (3D) finite element code have also been presented with an implementation of the code on a cluster of workstations.

### Summary of Accomplishments

- A two-coil flux shaping probe has been designed and tested to reduce the effect of edges for detection of flaws in multilayer structures of aircraft frames. The designed probe uses active compensation and consists of two concentric coils with currents of different magnitude and phase to obtain the desired shape of the flux distribution. This method is seen to minimize edge effect irrespective of the operating frequency and can be useful for low-frequency inspection of embedded flaws. The conventional methods of shielding are not very effective in focusing the flux inside the test samples at low frequencies. The probe performance is extremely sensitive to the design parameters such as the relative current magnitude and phase in the coils, and the coil cross-sectional geometry. The concept of shaping the flux distribution is very useful in the design of special purpose probes and this thesis presents a feasibility study of using active compensation for designing probes with a desired field distribution.
  - The remote field eddy current (RFEC) phenomenon has been modeled for detecting embedded defects in thick metal plates. The model presents a novel procedure for handling very large volumes. The technique for reducing the computer resource required is based on partitioning the total volume of interest into two smaller subvolumes. The volume with the driver coil is used to compute the boundary conditions on the plane of partition for the volume with the pickup coil and the defect. The volume modeling the driver coil is further reduced by
-

using the additional symmetry created by the absence of defects in the volume. The validity of the volume partition approach has been demonstrated by comparison with experimental measurements.

- The magneto-optic eddy-current/imaging (MOI) has been numerically modeled and experimentally validated. The model has been successfully applied to a number of inspection geometries such as holes, cracks and corrosion. The simulation results are currently being used by industry for optimizing experimental parameters. The model can be easily extended to other aircraft geometries such as lap joints and cracks under fasteners (CUFs). This inspection method is being extended to detect corrosion in multilayer aluminum samples.
- A parallelization of the 3D finite element code has been successfully implemented. The decomposition and solution of the system of linear equations in the finite element modeling have been parallelized to run on a cluster of computing workstations. The programs use domain decomposition to obtain three subsystems of linear equations which have been tested and run on a 4 CPU system of DEC-Alpha workstations. The programming paradigm used is that of message passing implemented using the Message Passing Interface (MPI) communication standard. The parallelized finite element programs have been used to run on a cluster of workstations for solving the symmetric, banded, complex matrix equations. The use of distributed computing allows the modeling of large and dense meshes as computing resources from separate workstations get pooled.

## **Future Work**

The area of active compensation in eddy current probes is a development of this work that can find industrial applications. A two coil compensation method has been explored and this work may be extended to a more general multi-coil approach. The idea is very powerful and has significant potential in design of special purpose probes.

The model developed for the RFEC inspection method has been validated and can now be used for generating signals due to defects in thick plates. The model is currently being extended to model detection of cracks under fasteners (CUFs) in aircraft frames. The model as customized for magneto-optic/eddy current imaging (MOI) inspection is being used to determine the optimal design of the device to detect corrosion in two layer samples.

Initial work on code parallelization for cluster computing has been demonstrated. However a significant amount still remains to be done for optimizing the parallelized code, and conducting a more thorough analysis of the various issues such as using a variable number of processors and submatrices for domain decomposition.

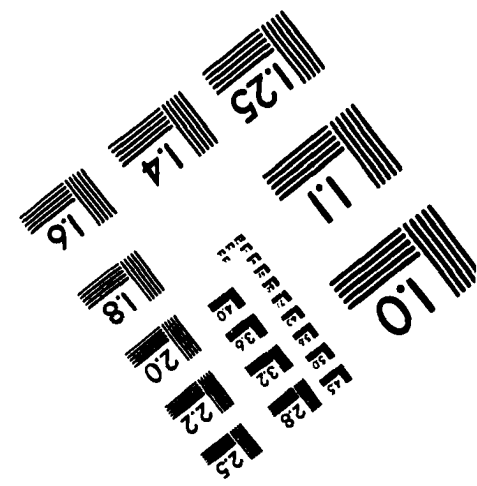
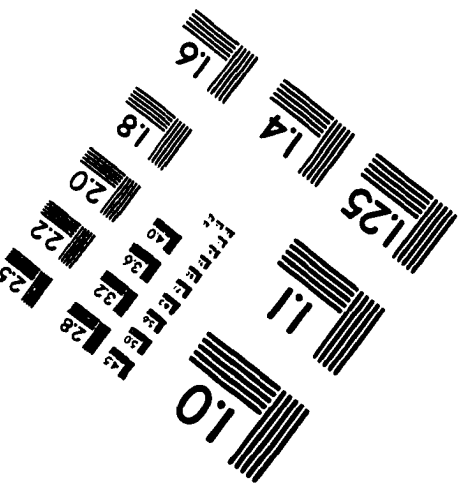
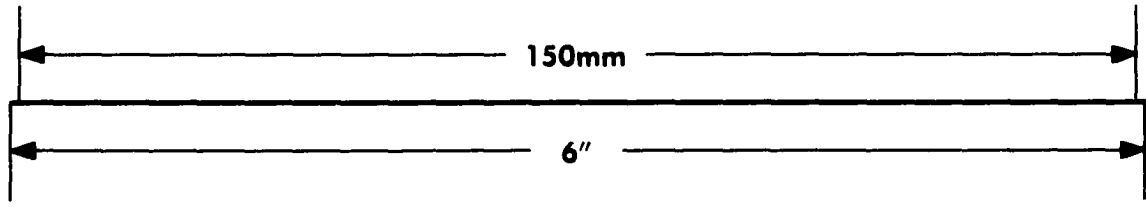
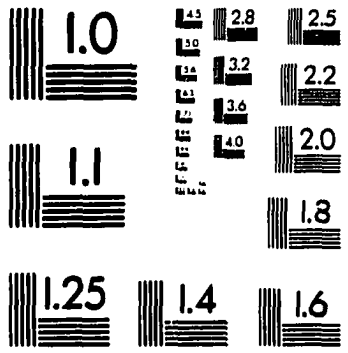
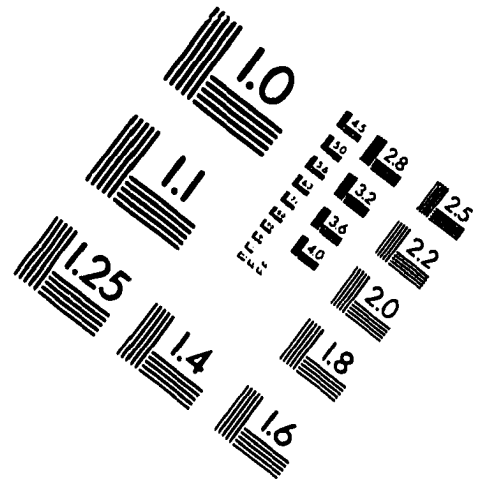
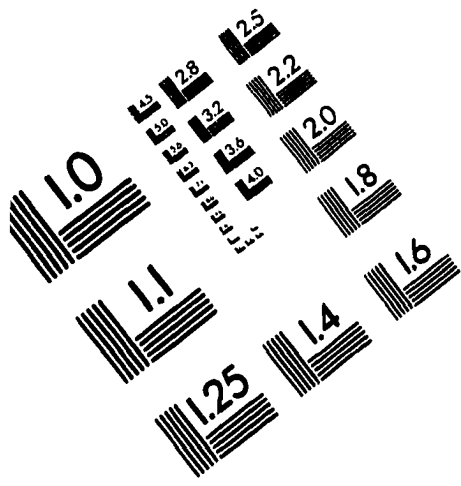
As a part of this research work a menu driven set of programs have been developed for preprocessing, mesh generation, finite element solution, post processing and graphical displays of the results. These programs have been customized for eddy current probe design and they can be enhanced by adding the graphical user interface.

## REFERENCES

- [1] A. J. Schwab, *Field Theory Concepts* Springer-Verlag, Berlin, Germany, 1988.
- [2] D. Jiles, *Introduction to Magnetism and Magnetic Materials* Chapman & Hall, London, United Kingdom, 1991.
- [3] R. Palanisamy, *Finite Element Eddy Current NDT Model* Ph.D. Thesis, Colorado State University, Fort Collins, Colorado, 1980.
- [4] N. Ida, *Three Dimensional Finite Element Modeling of Electromagnetic Nondestructive Testing Phenomena* Ph.D. Thesis, Colorado State University, Fort Collins, Colorado, 1983.
- [5] A. Krawczyk, J. Tegopoulos, *Numerical Modeling of Eddy Currents* Oxford University Press, Oxford, U.K., 1993.
- [6] C. V. Dodd, W. E. Deeds, J. W. Luquire, W. G. Spoeri, "Some Eddy-Current Problems and Their Integral Solutions", Contract No W-7405-eng-26, Oak Ridge National Laboratory, Oak Ridge, TN, April, 1969.
- [7] D. M. Bailey, "Shielded Eddy Current Probes", *Materials Evaluation*, pp. 776-786, June, 1983.
- [8] V. O. Kelha, J. M. Pukki, R. S. Peltonen, A. J. Penttinen, R. J. Ilmoniemi, J. J. Heino, "Design, Construction, and Performance of a Large-Volume Magnetic Shield" *IEEE Transactions on Magnetics*, pp. 260-270, vol. 18, no. 1, January, 1981.
- [9] F. W. Grover, *Inductance Calculations, Working Formulas and Tables* Dover Publications, Inc. New York, New York, 1946.
- [10] L. K. Urankar, "Vector Potential and Magnetic Field of Current-Carrying Finite Arc Segment in Analytical Form, Part I: Filament Approximation" *IEEE Transactions on Magnetics*, pp. 1283-1287, vol. 16, no. 5, September, 1980.
- [11] L. K. Urankar, "Vector Potential and Magnetic Field of Current-Carrying Finite Arc Segment in Analytical Form, Part III: Exact Computation for Rectangular Cross Section" *IEEE Transactions on Magnetics*, pp. 1860-1867, vol. 18, no. 6, November, 1982.
- [12] Z. Mottl, "The Quantitative Relations Between True and Standard Depth of Penetration for Air Cored Probe Coils in Eddy Current Testing" *NDT International*, pp. 11-18, vol. 23, no. 1, February, 1990.
- [13] T. R. Schmidt, "The Remote Field Eddy Current Inspection Technique", *Materials Evaluation*, vol. 42, pp. 225-230, February, 1984.
- [14] Y. Sun, S. Udpa, W. Lord and D. Cooley, "A Remote Field Eddy Current NDT Probe for Inspection of Metallic Plates", *Materials Evaluation*, vol. 54, no. 4, pp. 510-512, April, 1996.

- [15] Y. Sun, W. Lord, L. Udpa, S. Udpa, S. K. Lua and K. H. Ng, "Thick-Walled Aluminum Plate Inspection Using Remote Field Eddy Current Techniques", Proceedings of Review of Progress in Quantitative NDE-96, Brunswick, ME, July, 1996.
- [16] Y. S. Sun, "Finite-Element Study of Diffusion Energy Flow in Low-Frequency Eddy Current Fields" Materials Evaluation, pp 87-92, January, 1988.
- [17] T. R. Schmidt, "The Remote Field Low Frequency Eddy Current Inspection Technique", pp. 206-211 in *Electromagnetic Testing*, vol. 4 of Nondestructive Testing Handbook, 2nd ed., ASNT, Columbus, OH, 1987.
- [18] W. Lord, "A Finite Element Study of the Remote Field Eddy Current Phenomenon", Proceedings of Review of Progress in Quantitative NDE-87, Williamsburg, VA, June, 1987.
- [19] W. Lord, "Physics of the Remote Field Eddy Current Effect", paper presented at COMPUMAG-87, Graz, Austria, August, 1987.
- [20] S. Simms, "MOI: Magneto-Optic/Eddy Current Imaging," Materials Evaluation, pp.529-534, May, 1993.
- [21] M. J. Freiser, "A Survey of Magneto-optic Effects," IEEE Transactions on Magnetics, vol. 4, no. 2, June, 1968.
- [22] J. Smit (ed) *Magnetic Properties of Materials*, McGraw-Hill Inc. New York, NY, 1971.
- [23] J. Zak, E. R. Moog, C. Liu and S. D. Bader, "Fundamental magneto-optics," Journal of Applied Physics, vol. 68, no. 8, pp. 4203-4207, 15 October, 1990.
- [24] G. L. Fitzpatrick, D. K. Thome, R. L. Skaugset, E. Y. C. Shih and W. C. L. Shih, "Magneto-Optic/Eddy Current Imaging of Aging Aircraft: A new NDI Technique," Materials Evaluation, pp. 1402-1407, December, 1993.
- [25] D. Hagemaiier, "Eddy Current Detection of Short Cracks Under Installed Fasteners" ATA NDT Forum, Hartford, Connecticut, September, 1995.
- [26] D. Hagemaiier, "Eddy Current Detection of Subsurface Cracks", ATA NDT Forum, Minneapolis, Minnesota, August, 1989.
- [27] I. East, *Parallel Processing with Communicating Process Architecture*, UCL Press Limited, London, United Kingdom, 1995.

# IMAGE EVALUATION TEST TARGET (QA-3)



APPLIED IMAGE, Inc  
 1653 East Main Street  
 Rochester, NY 14609 USA  
 Phone: 716/482-0300  
 Fax: 716/288-5989

© 1993, Applied Image, Inc., All Rights Reserved